The Optical Spectrum of an LBV Candidate in the Cyg OB2 Association

V. G. Klochkova and E. L. Chentsov

Special Astrophysical Observatory, Russian Academy of Sciences, Nizhniĭ Arkhyz,
Karachaĭ-Cherkessian Republic, 369167 Russia
Received November 15, 2003; in final form, March 15, 2004

Abstract—We have obtained the first high-spectral-resolution ($R = 15\,000$ and $60\,000$) optical spectra for the extremely luminous star No. 12, identified with the IR source IRAS 20308+4104 in the Cyg OB2 association. We have identified about 200 spectral features at $4552-7939$ Å, including the interstellar NaI, KI lines and numerous DIBs, which are the strongest absorption lines in the spectrum, along with the HeI, CII, and SiII lines. A two-dimensional spectral classification indicates that the star's spectral type is B5±0.5 Ia$^+$. Our analysis of the radial-velocity pattern shows the presence of a radial-velocity gradient in the stellar atmosphere, due to the infall of matter onto the star. The strong Hα emission line displays broad Thompson wings and time-variable core absorption, providing evidence that the stellar wind is inhomogeneous, and a slightly blue-shifted P Cygni absorption profile. We conclude that the wind is time-variable. © *2004 MAIK "Nauka/Interperiodica".*

1. INTRODUCTION

Studies of mass loss and elemental-abundance variations in the surface layers are crucial for our understanding of the evolution of massive stars. It is important to establish the evolutionary stage and the star's luminosity with certainty. One widely used approach to stellar-evolution studies is to investigate stars in clusters and groups: the evolutionary stage, age, and luminosity can be determined fairly reliably for group members, whereas these characteristics are rather uncertain for field stars. It is especially important to study group members that are rare, such as LBV stars or Wolf−Rayet stars. From this point of view, the Cyg OB2 (or VI Cyg) association, with an age of several million years, is of special importance. The Cyg OB2 association contains a group of high-luminosity stars with correspondingly very high masses (about 100 $M_\odot$), and is so large that the association may be a young globular cluster [1].

According to Massey *et al.* [2], unevolved O and Of stars have been identified in the association, as well as an LBV candidate—the variable star No. 12 from the list of Schulte [3]. We will refer to this star as Cyg OB2−No. 12.

Cyg OB2−No. 12 is among the brightest OB stars in the IR, due to the presence of circumstellar matter lost by the star via its strong wind [4]. The star is identified with the IR source IRC+40430 = IRAS 20308+4104. For a distance modulus for the association of $m - M = 11.2^m$, the star's luminosity is $\log(L/L_\odot) = 6.26$ [5] and its bolometric absolute magnitude is $M_{bol} = -11^m$ [6]. Massey and Thompson [6] classified the star as B5 Ie, and Souza

and Lutz [7] as B8 Ia, whereas Humphreys and Davidson [8] considered it to be one of the Galaxy's brightest A supergiants. Massey *et al.* [2] later confirmed the LBV candidate status of Cyg OB2− No. 12 based on its membership in an association whose turnoff point is near that for the Milky Way's most massive stars.

The luminosity of Cyg OB2−No. 12 implied by its association membership indicates that the star is one of the four most luminous stars in our Galaxy (see, for instance, the diagram for S Dor stars presented by van Genderen [9] and Table 2 in the review of de Jager [5]). However, its visible light is strongly attenuated due to the large distance to the association and the presence of strong extinction: the observed magnitudes are $B = 14.41^m$, $V = 11.40^m$. It was recognized long ago that, apart from being distinguished by its high luminosity, Cyg OB2−No. 12 also displayed very high reddening [10, 11]. Based on their photometric study of a stellar sample in Cyg OB2, Torres-Dodgen *et al.* [12] estimated the association's distance modulus to be $m - M = 11.2^m \pm 0.2^m$ and its distance to be $d = 1.7 \pm 0.3$ kpc, and confirmed that the high interstellar reddening for the association members (with a mean value $E(B - V) = 1.82$) was satisfied by a normal law. The exception is Cyg OB2−No. 12, whose visual extinction exceeds 10^m (!). Obviously, spectroscopic studies of stars experiencing such a high degree of reddening are possible only thanks to the relatively small distance to the association and the high absolute luminosities of many of its members.

Lozinskaya *et al.* [13] also emphasized that the compact group of massive stars in the Cyg OB2 association probably possessed the Galaxy's strongest stellar winds, which are capable of significantly affecting the ambient interstellar gas over some two to three million years.

Cyg OB2−No. 12 is one of the few late B stars known to radiate thermal radio emission [4]. The variability of its radio flux is surprising [14]. White and Becker [15] estimated the mass-loss rate to be $4 \times 10^{-5} M_\odot$/yr, which is unusually high for a normal supergiant, but consistent with the extreme luminosity of Cyg OB2−No. 12. According to the criterion suggested by Humphreys and Davidson [8], a mass-loss rate that high indicates that Cyg OB2−No. 12 is an LBV star. Through his modeling of the IR spectral energy distribution, Leitherer *et al.* [16] estimated the star's effective temperature to be $T_{eff} = 13\,600$ K and the envelope's electron temperature to be $T_e = 5000$ K. The combination of a hot atmosphere and a cool, dense envelope found for Cyg OB2−No. 12 is not unique: such structures are known for S Dor stars [17].

The light from Cyg OB2−No. 12 is polarized [18]. The broadband polarimetry of Schulz and Lenzen [17] at $0.3-1.1$ μm displayed linear polarization exceeding 10%, providing evidence for a nonspherical distribution of the circumstellar material, and hence for a nonspherically symmetrical stellar wind.

The accumulated observations show that Cyg OB2−No. 12 is a crucial object for studies of late evolutionary stages for massive stars, creating the need for high-resolution optical spectroscopy that would make it possible to classify the spectrum, and thereby refine estimates of the star's fundamental parameters and the characteristics of its stellar wind.

2. OBSERVATIONS AND DATA REDUCTION

Our spectroscopic observations of Cyg OB2−No. 12 were acquired with the 6 m telescope of the Special Astrophysical Observatory (Russian Academy of Sciences) using echelle spectrographs. Our first set of observations, obtained on June 12, 2001 using the PFES spectrometer [19] with a 1040×1170-pixel CCD chip at the primary focus, yielded a spectrum in the interval $4542-7939$ Å with a resolution of $\lambda/\Delta\lambda \sim 15\,000$ (20 km/s). A second set of observations was obtained on April 12, 2003 at the Nasmyth focus using the NES spectrograph [20] equipped with an image slicer [21]. We obtained a spectrum in the range $5273-6764$ Å with a resolution of $\lambda/\Delta\lambda \sim 60\,000$ (5 km/s) using a 2048×2048-pixel CCD chip.

We used the PFES spectrometer to acquire spectra of bright, luminous B stars for use in spectral classification (see Section 3.1 for details). We eliminated cosmic-ray traces via a median averaging of two consecutive exposures. The wavelength calibration was performed using the spectrum of a ThAr hollow-cathode lamp. We recorded the spectrum of the hot, rapidly rotating star HR 4687, which has no narrow lines, each night for use in subtracting the telluric absorption spectrum.

The preliminary reduction of the CCD images of our echelle spectra (removal of cosmic rays, background subtraction, wavelength calibration, and extraction of the spectral orders) was performed using the MIDAS (98NOV) ECHELLE package. The final reduction (continuum normalization, measurements of radial velocities and equivalent widths for various spectral features) was done using the DECH20 program package [22].

3. DISCUSSION OF THE RESULTS

3.1. General Description of the Spectrum and Spectral Type of Cyg OB2−No. 12

The main features of Cyg OB2−No. 12 are evident even in low-resolution spectra [10]: it is an early-type, very luminous star with very strong Hα emission and extremely strong diffuse interstellar bands (DIBs). The Na D1,2 sodium-doublet lines display no obvious peculiarities. Wendker and Altenhoff [4] note that the Hα profile is probably variable.

Our high-resolution spectra enabled us for the first time to make detailed line identifications, classify the spectrum, and measure radial velocities. Table 1 presents identifications for the spectral features observed on June 12, 2001 and April 12, 2003, along with their equivalent widths W_λ, residual intensities r, and heliocentric radial velocities V_r. Figures 1 and 2 display fragments of the spectra of Cyg OB2−No. 12 and of the hypergiant HD 168625 (B6Ia$^+$, $M_v = -8.5^m$). The spectrum of HD 168625 was taken on June 19, 2001 with the PFES spectrometer. These spectra are very similar, demonstrating that the stars have similar temperatures and luminosities. In addition, DIBs are equally well represented in these spectra and have similar intensities. The strongest of them, the 5780 and 5797 Å bands, dominate in Fig. 1, but even the weak DIBs at 5766, 5773 Å, etc. have comparable intensities to the stellar NII, AlIII, and SiIII absorption. The DIBs at 6376 and 6379 Å in Fig. 2 are almost as deep as the SiII (2) absorption.

The vast majority of spectral features are shallow absorption lines with depths of $0.02-0.03$ of the continuum level, whose depths, equivalent widths, and

Table 1. Line identifications (multiplet number in brackets), equivalent widths W_λ, residual intensities r, and heliocentric radial velocities V_r for the spectra of Cyg OB2−No. 12 obtained on both dates (colons indicate uncertain values)

Element		λ_{lab}, Å	June 12, 2001			April 12, 2003		
			W_λ, Å	r	V_r, km/s	W_λ, Å	r	V_r, km/s
1		2	3	4	5	6	7	8
HeI	(48)	4921.93	0.43:	0.73	−18:			
FeII	(42)	4923.92	0.13:	0.9:				
DIB		4963.90	0.17:	0.86	−12:			
DIB		4984.81		0.92:				
NII	(19)	5001.4:	0.20:	0.90:	−5:			
NII	(6)	5002.70		0.93:				
NII	(19, 6)	5005.15	0.13:	0.91				
NII	(24)	5007.33	0.08:	0.95				
SII	(7)	5009.56		0.95:				
NII	(4)	5010.62	0.12:	0.94	−18			
HeI	(4)	5015.68	0.35	0.83	−14			
FeII	(42)	5018.44	0.12:	0.91:	−9:			
SII	(7)	5032.45	0.12:	0.93:	−17:			
NII	(4)	5045.10		0.96:				
HeI	(47)	5047.74	0.12:	0.93:				
FeIII	(5)	5073.90	0.08:	0.96:				
FeIII	(5)	5086.72	0.05:	0.96:				
FeIII	(5)	5127.35	0.09:	0.95:	−12:			
FeIII	(5)	5156.12	0.09:	0.92:	−10:			
FeII	(42)	5169.03	0.13:	0.93	−13			
FeIII	(113)	5235.66	0.10:	0.95:				
FeIII	(113)	5243.31		0.98:				
FeIII		5260.34		0.97				
FeII	(49, 48)	5316.65:	0.03:	0.98:				
SII	(38)	5320.73	0.04:	0.97:	−15:			
SII	(38)	5345.72	0.06:	0.97:	−18:			
DIB		5404.50		0.95:	−12:			
DIB		5418.90		0.96:		0.07:	0.92	−16:
SII	(6)	5428.67	0.07	0.96	−19:	0.05:	0.96:	−26:
SII	(6)	5432.82	0.10	0.94	−20:	0.13	0.91	−23
SII	(6)	5453.83	0.24	0.88	−16	0.21	0.86	−25
SII	(6)	5473.62	0.05	0.97	−18	0.09:	0.94:	
DIB		5487.67	0.22	0.95				
DIB		5494.10	0.07	0.92	−14	0.08	0.90	−13

Table 1. (Contd.)

1		2	3	4	5	6	7	8
NII	(29)	5495.67	0.06:	0.97:				
DIB		5508.35		0.95				
SII	(6)	5509.72		0.95:	−17:			
DIB		5512.64	0.04	0.96	−12:	0.04	0.93	−8:
CII	(10)	5535.35	0.06:	0.97:				
DIB		5541.62		0.97				
DIB		5544.96	0.05	0.94	−9	0.09:	0.92	−12:
SII	(6)	5564.98				0.04:	0.96:	−27:
DIB		5594.59		0.98	−12:			
SII	(11)	5606.15	0.06	0.96	−13	0.09	0.95:	−25:
DIB		5609.73	0.04	0.98	−10	0.04	0.96:	−10:
SII	(11)	5616.64		0.98:	−15:			
SII	(14, 11)	5640.1:	0.17	0.89	−10:	0.23	0.89	−24:
SII	(14)	5647.03	0.06	0.96	−18:	0.07	0.93	−26
SII	(11)	5659.99		0.99:		0.06:	0.95:	−27:
SII	(11)	5664.78		0.98				
NII	(3)	5666.63	0.13:	0.92	−17	0.11	0.92	−27:
NII	(3)	5676.02	0.12:	0.95	−19:	0.13	0.92	−20:
NII	(3)	5679.56	0.23:	0.89	−17	0.24	0.85	−23
NII	(3)	5686.21	0.13:	0.96	−22:			
AlIII	(2)	5696.60	0.10	0.93	−13	0.12	0.91	−23
DIB		5705.20	0.25	0.92	−20:	0.30	0.92	
NII	(3)	5710.77	0.13	0.93	−16	0.14	0.92	−16
DIB		5719.30	0.05	0.97	−1			
AlIII	(2)	5722.73	0.09	0.94	−20	0.06:	0.96	−15:
SiIII	(4)	5739.73	0.15	0.93	−10	0.12	0.92	−19:
NII	(9)	5747.30		0.96				
DIB		5766.16	0.05	0.95	−8	0.06	0.96	−13:
DIB		5769.04	0.03	0.98	−10:	0.03	0.97:	−8:
DIB		5772.60	0.05:	0.97	−14:	0.04	0.97:	−10:
DIB		5775.78		0.97:				
DIB		5780.37	1.03	0.60	−9	0.95	0.62	−8
DIB		5785.05		0.97:				
DIB		5793.22		0.97:	−6:			
DIB		5795.16		0.96:	−5:			
DIB		5796.96	0.38	0.69	−9	0.35	0.69	−9
DIB		5809.24	0.06:	0.97:		0.05	0.96:	−9:

Table 1. (Contd.)

1		2	3	4	5	6	7	8
DIB		5811.96		0.98	−15:			
DIB		5818.75		0.97:	−6:	0.05	0.96:	−13:
DIB		5828.46	0.06:	0.97				
FeIII	(114)	5833.93	0.05:	0.97	−15:	0.07	0.96:	−15:
DIB		5842.23		0.97				
DIB		5844.80		0.96	−12			
DIB		5849.80	0.16	0.88	−12	0.14	0.86	−12
HeI	(11)	5875.72	0.76	0.64	−2	0.82	0.66	−12
NaI	(1)	5889.95					0.40	−34
NaI	(1)	5889.95	0.92	0.11	−13	0.82	0.01	−9
NaI	(1)	5895.92					0.58	−34
NaI	(1)	5895.92	0.76	0.14	−12	0.72	0.02	−9
DIB		6005.03		0.96:	−7:			
DIB		6010.65	0.30:	0.95	−13			
DIB		6019.36	0.03:	0.97	−14	0.03:	0.98:	−13:
DIB		6027.48	0.06:	0.98	−10	0.07	0.95	−11
DIB		6037.61	0.09:	0.97	−19:	0.15	0.96	
OI	(22)	6046.4:	0.03:	0.99:				
DIB		6059.67	0.05:	0.98:	−11:			
DIB		6065.20		0.98:	−18:	0.04	0.97:	−9:
DIB		6068.20	0.02:	0.99				
NeI	(3)	6074.34	0.04:	0.98	−7:			
DIB		6084.75	0.03:	0.98				
PII	(5)	6087.82	0.02:	0.99:				
DIB		6089.78	0.06	0.94	−7	0.04	0.94	−11
NeI	(3)	6096.16	0.05	0.97:	−8:			
DIB		6108.05		0.98:	−10:			
DIB		6113.20	0.05	0.96	−14	0.06	0.96	−13
DIB		6116.80	0.03:	0.98	−10:			
DIB		6118.68:		0.99				
DIB		6139.94	0.03	0.97	−15	0.02	0.96	−10:
NeI	(1)	6143.06	0.05	0.97	−8:	0.10	0.95	−27
FeII	(74)	6147.74		0.99				
OI	(10)	6156.3:		0.99				
OI	(10)	6158.18		0.98	−5:			
DIB		6161.9:		0.98	−10:			
NeI	(5)	6163.59		0.98				
PII	(5)	6165.59		0.98:				

Table 1. (Contd.)

1		2	3	4	5	6	7	8
FeIII		6185.26		0.98:				
DIB		6194.73		0.98				
DIB		6195.96	0.12	0.86	−12	0.12	0.80	−12
DIB		6203.08		0.85	−14	0.30:	0.85	−12
DIB		6211.66	0.03:	0.97	−14:			
DIB		6212.90	0.02:	0.98	−9:			
DIB		6215.79		0.99				
DIB		6220.81		0.99	−15:			
DIB		6223.56		0.98		0.04	0.95	
DIB		6226.30		0.99				
DIB		6234.03		0.95	−14:	0.05	0.95	−12
DIB		6236.67		0.98				
FeII	(74)	6238.39		0.99:				
FeII	(74)	6247.55		0.99:				
DIB		6250.82		0.98	−12:			
NeI	(5)	6266.50	0.04:	0.97	−14:	0.05	0.97	
DIB		6269.75	0.27	0.86	−13	0.28	0.85	−11
DIB		6283.85		0.59	−14		0.61	−10:
SII	(26)	6312.66		0.98	−16:			
FeII		6317.99		0.98:				
DIB		6324.80	0.04:	0.97:				
DIB		6329.97	0.03	0.98	−11:			
NeI	(1)	6334.43	0.03	0.98:	−9:		0.97:	−20:
SiII	(2)	6347.10	0.39	0.81	−14	0.40	0.78	−28
DIB		6353.34	0.05	0.98	−15:	0.04	0.97	−15:
DIB		6362.30	0.05	0.98	−15:	0.06	0.97:	−12:
DIB		6367.25	0.04:	0.97	−13:	0.04	0.95	−8
SiII	(2)	6371.36	0.28	0.87	−14	0.33	0.84	−30
DIB		6375.95	0.11:	0.93	−10	0.13	0.86:	−14
DIB		6379.29	0.18	0.83	−12	0.20	0.78	−12
NeI	(3)	6382.99	0.04	0.97		0.06:	0.95	−32:
SII	(19)	6384.89		0.99				
DIB		6397.39	0.08	0.96				
DIB		6400.30		0.98:				
NeI	(1)	6402.25	0.13	0.93	−9			
DIB		6410.18	0.04:	0.98				
SII	(19)	6413.71	0.05:	0.98				

Table 1. (Contd.)

1		2	3	4	5	6	7	8
DIB		6425.70	0.03:	0.97	−13			
FeII	(40)	6432.68	0.03:	0.98:				
DIB		6439.50	0.06	0.95	−12	0.05	0.94	−9
DIB		6445.20	0.05	0.94	−10	0.07	0.92	−11
DIB		6449.14	0.04	0.96:	−11:	0.05	0.96	−10:
FeII	(74)	6456.38		0.95:	−15:			
NII	(8)	6482.05		0.95:	−13:			
NeI	(3)	6506.53		0.97	−10:		0.93:	−26:
Hα		6562.81	4.0:	1.6	−8		1.76	−15
CII	(2)	6578.05	0.38:	0.82	−6	0.39	0.80:	−23:
CII	(2)	6582.88	0.29:	0.86	−9			
DIB		6597.31		0.96	−10:			
NeI	(6)	6598.95		0.98				
NII	(31)	6610.57		0.99:				
DIB		6613.56	0.42	0.70	−9	0.39	0.68	−12
DIB		6632.85		0.99:				
OII	(4)	6640.90		0.99:				
DIB		6646.03		0.99:				
DIB		6660.64	0.06	0.93	−11	0.07	0.92	−10
DIB		6665.15		0.98				
DIB		6672.15	0.05	0.96	−13			
HeI	(46)	6678.15	0.75	0.68	−2			
DIB		6689.30	0.03:	0.99	−13:			
DIB		6694.48	0.02:	0.99	−17:			
DIB		6699.26	0.07	0.95	−11			
DIB		6701.98	0.02	0.98	−15			
DIB		6709.39	0.02:	0.98	−6:			
DIB		6729.28	0.02:	0.98	−11:			
DIB		6737.13	0.02:	0.99	−13:			
DIB		6740.99	0.03:	0.98				
DIB		6767.74	0.01:	0.99	−17:			
DIB		6770.05	0.03:	0.98	−9			
DIB		6788.66	0.02:	0.99	−7:			
DIB		6792.52	0.03	0.98	−12			
DIB		6795.24	0.03	0.98	−6:			
DIB		6801.37	0.02:	0.98	−9			

Table 1. (Contd.)

1		2	3	4	5	6	7	8
DIB		6810.5:		0.98:				
DIB		6827.30	0.02:	0.98	−14			
DIB		6843.60	0.06	0.96	−19			
DIB		6852.67	0.02	0.98				
DIB		6860.02	0.05	0.97	−17			
DIB		6862.53	0.03:	0.99				
HeI	(10)	7065.32	0.36:	0.82	+2:			
DIB		7357.60		0.91	−14:			
NI	(3)	7468.31	0.05	0.98	−15:			
DIB		7494.89		0.98:	−9:			
FeII		7495.63		1.01				
FeII		7513.17		1.03	−12			
DIB		7559.35		0.97	−12			
DIB		7562.3:	0.25:	0.94	−13:			
DIB		7581.30	0.08:	0.97	−12:			
KI	(1)	7664.91	0.70:	0.4:	−9:			
DIB		7721.85	0.07	0.96	−10			
OI	(1)	7771.94	1.23[1]	0.76	+3:			
OI	(1)	7774.2:		0.75				
DIB		7832.81	0.05	0.97	−10			

[1] Triplets combined equivalent width.

radial velocities are uncertain (marked with colons in Table 1).

The signal-to-noise ratio in the blue was not high, and we used nonstandard criteria for our quantitative spectral classifications. The sets of classification criteria and the wavelength intervals used for 2001 and 2003 overlap only partially. The classification techniques are described in more detail in [23]. Here we note only that the HeI, CII, NII, AlIII, SiII, SII, and FeII lines were used.

The $W(\mathrm{Sp})$ calibration relations were based on the supergiant standard stars ϵ Ori (O9.5Ia), HD 13854 (B1.2Iab), HD 14134 (B2.2Ia), HD 206165 = 9 Cep (B2.5Ib), HD 198478 = 55 Cyg (B3.4Ia), HD 164353 = 67 Oph (B3.6Ib, $M_v = -5.6^m$), HD 58350 $= \eta$ CMa (B3.9Ia), HD 13267 = 5 Per (B5Ia), HD 15497 (B6Ia, $M_v = -7.0^m$), HD 183143 (B7.7Ib, $M_v = -8^m$), HD 34085 $= \beta$ Ori (B8.2Ia, $M_v = -7.3^m$), and HD 21291 (B9.3Ib, $M_v = -6.9^m$).

A comparison of the absorption depths and equivalent widths in our two spectra shows that, although the depths were slightly smaller in 2001 than in 2003 (due to the lower resolution), the equivalent widths did not differ systematically. It is thus natural that the spectral types derived for Cyg OB2−No. 12 for the 2001 and 2003 data were the same within the errors: B5.0±0.5 and B4.8±0.5, respectively. The luminosity class for both Cyg OB2−No. 12 and HD 168625 is Ia$^+$. Evidence for the star's high luminosity is also provided by the high intensity of the OI 7773 Å IR triplet, whose equivalent width is $W = 1.14$ Å, corresponding to an absolute magnitude of $M_v < -8^m$.

3.2. The Hα Line Profile

Based on two spectra with 3 Å resolution taken three days apart, Souza and Lutz [7] concluded that the radial velocity derived from the Hα emission line was variable. An absorption line at 6532 Å
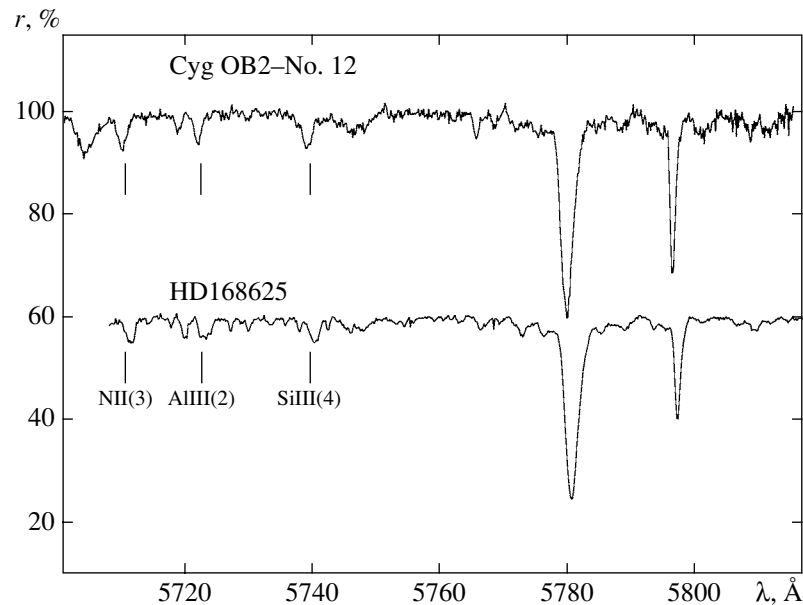
Fig. 1. Fragment of the spectrum of Cyg OB2−No. 12 taken on June 12, 2001 (top) compared to the corresponding fragment of the spectrum of the B5Iae$^+$ star HD 168625 (bottom). The stellar lines are marked, with their identifications given. The rest of the absorption features are DIBs; the deepest are at 5780 and 5797 Å (Table 1).
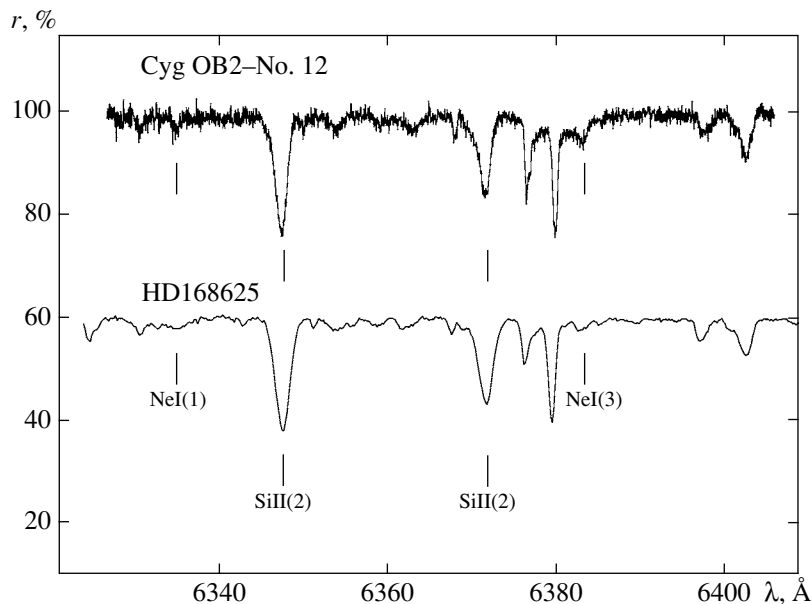
Fig. 2. Same as Fig. 1 for the region of the SiII doublet (Table 1).

was detected in one of the spectra, whose position corresponds to an expansion velocity of about −(1400−1500) km/s. The spectrum with 7 Å resolution presented in [18] shows a similar absorption feature (6526 Å).

Our high-resolution spectra enabled us to study the structure of the Hα emission profile (Fig. 3) in detail. The profile has broad wings extending to at least ±1000 km/s is slightly asymmetric, with weak absorption visible in the left wing, suggestive of a P Cygni profile; and displays absorption features with variable shape in the core. These absorption features correspond to transitions in the Hα line rather than to the telluric spectrum, whose contribution was carefully removed from the spectrum.

We are inclined to interpret the emission wings of
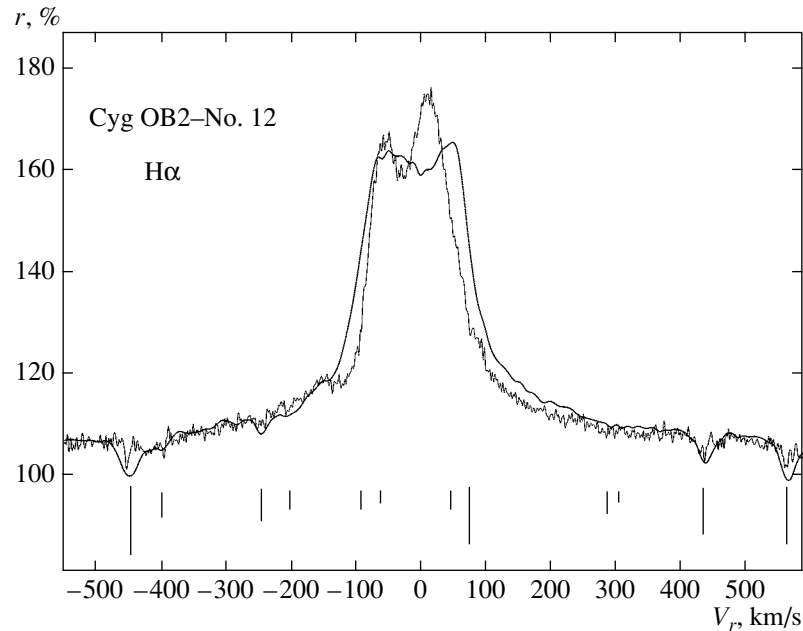
Fig. 3. Hα line profiles ($r(V_r)$ relations) in the spectra of Cyg OB2−No. 12 obtained on June 12, 2001 (solid) and April 12, 2003 (thin). The vertical dashes show the positions of telluric H$_2$O lines, with the dash lengths being proportional to the line depths.

the Hα profile as being due to Thompson scattering on the envelope's free electrons [24−26]. Stark emission wings are formed in denser media, such as the de-excitation region behind the shock front in the atmosphere of W Vir [27]. Following Wolf *et al.* [28], let us estimate the efficiency of Thompson scattering for a hot envelope in which the hydrogen is completely ionized. In accordance with [15], let us assume a mass-loss rate of $4 \times 10^{-5} M_\odot$/yr and a radius for the envelope equal to twice the stellar radius ($R_\star = 338 R_\odot$ [14]). It is more difficult to estimate the escape velocity based on the two absorption features observed in the Hα wing [7, 18]. The value of 1400 km/s used in [15] seems too high. Note that the shell forming the narrow absorption feature must be spatially separated from the shell forming the P Cygni profile. It is not clear why the presence of this shell is not manifest in the spectrum taken three days later [7]. The distance covered at such a speed over three days is about 3.7×10^{13} cm, which is a factor of four higher than the envelope's radius estimated in an adiabatic cooling wind model, based on observations of free−free emission transitions at 6 cm [15]. This would imply that the optical spectral features are formed further from the star than the radio emission. This discrepancy can be removed if we reject the assumption of spherical symmetry for the envelope. In fact, if the wind extends differently in different directions, its temperature in a spherical approximation will be lower than the real tempera-

ture, as is observed (5000 ± 1500 K [15]). For the above high escape velocity and large radius, the optical depth to Thompson scattering in the spherically symmetric approximation [28] is insignificant, about 0.01. If the escape velocity is lower by an order of magnitude, as is suggested in [14] (see also our estimate of the highest wind velocity below), and the wind is not spherically symmetric, the Thompson-scattering optical depth increases by more than an order of magnitude.

We conclude that the absorption features we have detected at the peak and in the blue wing of the Hα line are variable, even after we have taken into account the different spectral resolutions of our observations.

3.3. Interstellar Features

The strength of the interstellar (and circumstellar) extinction of the light from Cyg OB2−No. 12 has made the star a popular target for studies of interstellar spectral features. In particular, the strong absorption towards Cyg OB2−No. 12 is of considerable interest from the point of view of investigating the discrete distribution of the absorbing material (cf., for example, Scappini *et al.* [29] and references therein). Souza and Lutz [30] first detected IR bands of the C$_2$ molecule, and molecular features in the spectrum of Cyg OB2−No. 12 were subsequently analyzed in a number of studies. In their high-spectral-resolution study, Gredel and Münch [31] detected a

four-component structure in the IR $(1, 0)$ band of the C_2 molecule's Phillips system, which displayed a range of velocities from -10.6 to $+13.2$ km/s, whereas Chaffee and White [32] observed two components in the KI line with velocities from -12.9 to -4.3 km/s. Gredel *et al.* [33] used echelle spectra to analyze the physical conditions for the formation of the C_2 and CN molecules in detail, and also detected an interstellar rubidium (RbI) line.

We also note that the star's spectrum is densely populated by interstellar features, as can clearly be seen in Figs. 1 and 2. It follows from Figs. 1 and 2 and Table 1 that the intensities of the main DIBs and of the NaI lines are higher than those of the strongest photospheric absorption lines (HeI, CII, SiII) in the spectrum of Cyg OB2–No. 12. We discuss the structure of the D1 and D2 NaI(1) lines below, in connection with the systemic velocity of Cyg OB2–No. 12.

3.4. Radial Velocities

Table 2 presents radial velocities for individual lines and averages for groups combining lines with similar residual intensities. Possible systematic errors for the velocities in Tables 1 and 2 estimated from the telluric and interstellar lines are within 2 and 1 km/s for the June 12, 2001 and April 12, 2003 spectra, respectively. It is also necessary to take into account the differing spectral resolutions when comparing $V_r(\mathrm{NaI})$ for the 2001 and 2003 spectra. Figure 4 shows that, in the April 2003 spectrum, the main component with $r \approx 0.01$ and $V_r = -9$ km/s is clearly separated from a component with $V_r = -34$ km/s that is half as strong. The June 2001 PFES spectrum does not show these components as being separated, but the asymmetry of the profile is appreciable, with the blue wing being less steep.

The random measurement errors for individual lines can be judged from the scatter of the circles in the upper panels of Fig. 5, with the following caveats. The velocities were measured from absorption cores, i.e., from the lowest parts of the profiles, with exclusion of the very deepest portions having much lower intensity gradients. Of the two lines whose profiles are displayed in the bottom panels of Fig. 5, the core in the June 2001 spectrum is sharper for the HeI absorption line, so that its position can be measured more accurately, whereas the SiII absorption line is sharper in the April 2003 spectrum. The SiII (2) lines (open circles in Fig. 5) are obviously blueshifted relative to other absorption lines with the same depths, but the other lines may also possess small mutual shifts, increasing the scatter of the data points in the $V_r(r)$ diagrams. In addition, many of the lines are asymmetric (as is also clearly visible

Table 2. Heliocentric radial velocities, V_r, for individual lines and groups of lines in the spectrum of Cyg OB2–No. 12 (colons indicate uncertain values)

Lines	V_r, km/s	
	June 12, 2001	April 12, 2003
Emission features		
Hα	-10	-15
FeII	-12:	
Stellar absorption features		
NII, OII, SII, etc.	-16	-25
SiII (2)	-14	-29
CII (2)	-11	-24:
HeI 5876	-1	-12
Hα	-140:, 0:	-125:, -28
Interstellar absorptions		
NaI (1)	-11	-34, -9, 20
KI (1)	-10:	
DIB	-10	-11

in Fig. 5), and a small shift in r has a considerable influence on the resulting value of V_r.

3.4.1. The systemic velocity of Cyg OB2–No. 12. Unfortunately, we have no data on the radial velocities of any stars of the association besides Cyg OB2–No. 12 itself and the spectroscopic binary Cyg OB2–No. 5, whose gamma velocity is very uncertain [34]. However, a rough estimate of the systemic velocity, V_{sys}, for Cyg OB2–No 12 is possible based on the differential rotation of the Galaxy. In our case, this estimate is facilitated by the fact that the dependence of the velocity on distance is weak in the direction toward Cyg OB2–No. 12 (along the Cygnus arm), and almost disappears in the region of the Cyg OB2 association [35]. This circumstance makes it possible to use a wider range of acceptable distances for stars, HII regions, and cool gaseous clouds whose radial velocities are to be used to estimate V_{sys}. The relation between the heliocentric radial velocity, V_r, and Galactic longitude, l, for stars between 1 and 2 kpc selected from the catalogs [36–38] gives the mean value $V_r = -12 \pm 3$ km/s for the longitude of Cyg OB2 ($l = 80°$). The peak of the interstellar Hα emission profile at $l = 80°$ is also at $V_r = -12$ km/s [13, 39], and the highest intensity of the CO radio emission is at $V_r = -9$ km/s [40]. A similar V_r value for the Cyg OB2 association (about
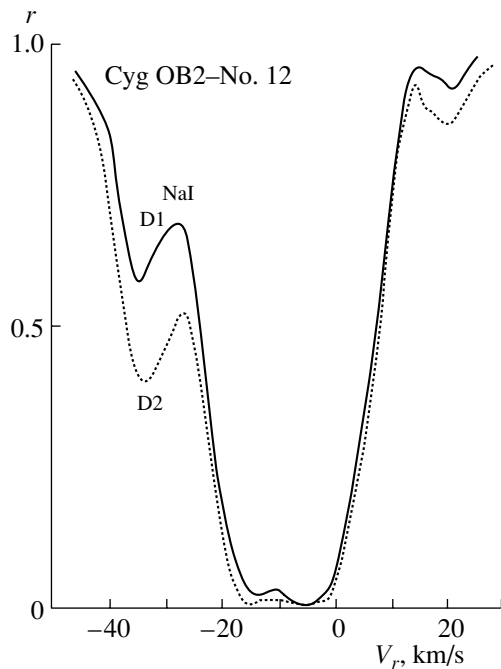
Fig. 4. Profiles of the D1 (solid) and D2 (dotted) NaI lines in the spectrum of Cyg OB2–No. 12 (April 12, 2003).
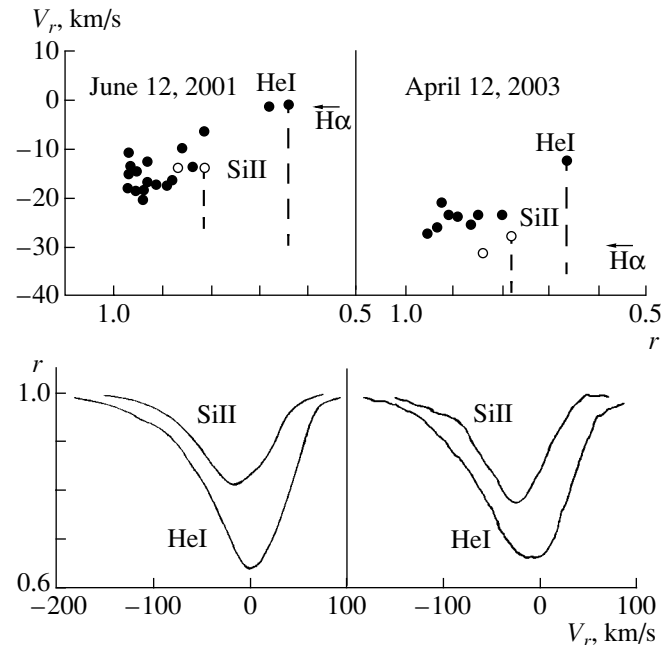

Fig. 5. Radial velocities in the atmosphere of Cyg OB2–No. 12. Top: the heliocentric radial velocities versus the residual intensities. Circles correspond to absorption cores, the horizontal dash to the FeII 7513 Å emission, and arrows to dips in the peak of the Hα profiles. The vertical dashed lines show the direction and amount of wing shifts for the SiII 6347 Å and HeI 5876 Å lines, and the horizontal dashed line corresponds to the systemic velocity, $V_{sys} = -11$ km/s. Bottom: the corresponding profiles of the SiII 6347 Å and HeI 5876 Å lines.

-10 km/s) results from the detailed analysis of the motions of stars and interstellar matter in the Cygnus arm carried out by Sitnik *et al.* [41].

Let us supplement the above V_r estimates with those obtained specifically for Cyg OB2–No. 12. According to McCall *et al.* [42], the CO emission has two intensity peaks, with $V_r = -7$ and -2 km/s, and the interstellar absorption profiles of KI, CO, C_2, etc. have up to five components with V_r values from -13 to 12 km/s. The profiles of the interstellar NaI doublet in our high-resolution spectrum (Fig. 4) have two main components: the strongest is saturated and has $V_r = -9$ km/s, while the shallower one is blueshifted and has $V_r = -34$ km/s. A similar division into components with the same intensity ratio and velocities (-11 and -35 km/s) is observed in the D2 NaI line for the spatially nearby hypergiant P Cygni [43]. The blueshifted component is probably circumstellar, and is associated with the stellar wind. Judging from its velocity, the main absorption feature is formed immediately in front of the star, in the gas complex that Sitnik *et al.* [41] call BB. There are dips at the bottom of this absorption feature, whose velocities (-13 and -6 km/s) coincide with those for the components of the KI line according to Chaffee and White [32] and McCall *et al.* [42]. Finally, we should include our velocity estimates for stationary envelope emission lines (the first rows of Table 2). The weak FeII 7513 Å emission line, which is unfortu-

nately the only one, gives $V_r \approx -12$ km/s; the upper, symmetric part of the Hα profile, which experiences minimal distortion from the absorption components, gives $V_r = -10 \ldots -15$ km/s.

As expected, all these estimates are close to each other. We adopt $V_{sys} = -11 \pm 2$ km/s as the center-of-mass velocity for Cyg OB2–No. 12.

3.4.2. Temporal and line-to-line variations of V_r. Figure 5 and the data in Table 1 show that the radial velocities measured from the absorption-line cores vary in time and change with the line intensity. In both our spectra, the weakest lines ($r \to 1$) yield V_r values lower than V_{sys} (by 5 and 14 km/s, respectively, in 2001 and in 2003), testifying to variable rates of expansion of the layers where they are formed. Stronger lines show positive shifts relative to weaker ones, with the exception of the SiII lines, marked in Fig. 5 as open circles. The slope of the filled-circle chain in the left panel of Fig. 5, corresponding to June 12, 2001, is quite evident, whereas it is poorly represented in the upper right panel of Fig. 5 due to the limited spectral range and some deficiencies of the

April 12, 2003 data. The core of the deepest available absorption line, HeI 5876 Å, shows the highest V_r, which exceeded V_{sys} by 10 km/s on June 12, 2001; according to McCall *et al.* [44], this shift reached values as large as 22 km/s.

3.4.3. Manifestations of the wind. The stellar wind from Cyg OB2−No. 12 is manifest most clearly in the Hα profile. Figure 3 shows that the profile shape varies with time, but its principal features are preserved: strong emission, with a dip at the short-wavelength slope, a sheared peak, and extended Thompson wings. The blueshifted absorption is barely visible in the June 2001 spectrum and is more pronounced in the April 2003 spectrum, but can be traced at least to $V_r = -160$ km/s in both cases; i.e., to the same limit that is reached by the blue wings of the absorption lines presented in Fig. 5. The wind's velocity limit is about 150 km/s.

The intensity inversions in the upper part of the Hα profile are especially interesting. They indicate that the wind from Cyg OB2−No. 12 is not uniform: in addition to the high-velocity material noted above, it contains a fair amount of material that is nearly stationary relative to the star, or is even falling onto the stellar surface. The coexistence of lines with direct and inverse P Cygni profiles in the same spectrum, and even combinations of such features in the profile of the **same** line, has been noted for some LBVs at their maximum brightness [45, 46]. This behavior leads us to reject the spherically symmetric wind model. It is possible that the slow part of the wind also contributes to the absorption profiles; spectroscopic monitoring is needed to check this hypothesis. So far, this possibility is supported by the coincident velocities for the central dips of the Hα line and the well-formed cores of strong absorption lines (HeI 5876 Å in 2001 and SiII 6347 Å in 2003), as well as by the fact that the shift of all the absorption lines in the 2003 spectrum towards short wavelengths relative to their positions in 2001 was accompanied by a similar shift of the central dip in Hα.

At any rate, both the hydrogen lines and the strongest absorption lines in the visual spectrum Cyg OB2−No. 12 (for the available part of the spectrum, these are the HeI and SiII lines) are partially formed in the wind.

4. CONCLUSIONS

Our detailed spectroscopy of the extremely luminous star Cyg OB2−No. 12 in the stellar association Cyg OB2 at 4552−7939 Å has enabled us to identify about 200 spectral features, including numerous interstellar features (NaI, KI, and DIBs). Using spectral-classification criteria developed for long

wavelengths, we have determined the star's spectral type (B5±0.5) and luminosity class (Ia$^+$). The intensity of the IR oxygen triplet, OI λ 7773 Å, leads to an absolute magnitude for the star $M_v < -8^m$.

Our analysis of the radial-velocity pattern indicates the presence of a radial-velocity gradient in the atmosphere due to the infall of matter onto the star.

We have detected fine structure of the profile of the strong Hα emission: broad emission wings (to ± 1000 km/s), absorption at the peak that varies with time, and weak P Cygni absorption features corresponding to expansion velocities up to 150 km/s. The intensity inversion at the Hα peak provides evidence that the stellar wind is not uniform: in addition to that part of the wind that moves away from the star, there is also material that is at rest relative to the star, or is even falling onto the stellar surface.

The radial velocities measured from the absorption-line cores vary with time and with the line intensity. The weakest lines ($r \to 1$) in our two spectra give V_r values lower than V_{sys} (by 5 and 14 km/s, respectively, in 2001 and 2003), testifying to a variable rate of expansion of the layers in which they are formed. Our discovery of evidence that the wind is variable shows the necessity of spectroscopic monitoring of this star.

ACKNOWLEDGMENTS

REFERENCES

1. F. Comeron, A. Pasquali, A. Rodighiero, *et al.*, Astron. Astrophys. **389**, 874 (2002).
2. P. Massey, K. DeGioia-Eastwood, and E. Waterhouse, Astron. J. **121**, 1050 (2001).
3. D. H. Schulte, Astrophys. J. **128**, 41 (1958).
4. H. J. Wendker and W. J. Altenhoff, Astron. Astrophys. **92**, L5 (1980).
5. C. de Jager, Astron. Astrophys. Rev. **8**, 145 (1998).
6. P. Massey and A. B. Thompson, Astron. J. **101**, 1408 (1991).
7. S. P. Souza and B. L. Lutz, Astrophys. J. **235**, L87 (1980).

8. R. M. Humphreys and K. Davidson, Publ. Astron. Soc. Pac. **106**, 1025 (1994).

9. A. M. van Genderen, Astron. Astrophys. **366**, 508 (2001).

10. W. W. Morgan, H. L. Johnson, and N. G. Roman, Publ. Astron. Soc. Pac. **66**, 85 (1954).

11. S. Sharpless, Publ. Astron. Soc. Pac. **69**, 239 (1957).

12. A. V. Torres-Dodgen, M. Carroll, and M. Tapia, Mon. Not. R. Astron. Soc. **249**, 1 (1991).

13. T. A. Lozinskaya, V. V. Pravdikova, and A. V. Finogenov, Pis'ma Astron. Zh. **28**, 260 (2002) [Astron. Lett. **28**, 223 (2002)].

14. J. H. Bieging, D. C. Abbott, and E. B. Churchwell, Astrophys. J. **340**, 518 (1989).

15. R. L. White and R. H. Becker, Astrophys. J. **272**, L19 (1983).

16. C. Leitherer, B. Wolf, O. Stahl, and C. Bertout, Astron. Astrophys. **140**, 199 (1984).

17. A. Schulz and R. Lenzen, Astron. Astrophys. **121**, 158 (1983).

18. K. H. Nordsieck, Publ. Astron. Soc. Pac. **86**, 324 (1974).

19. V. E. Panchuk, I. D. Najdenov, V. G. Klochkova, *et al.*, Bull. Spec. Astrophys. Obs. **44**, 127 (1998).

20. V. E. Panchuk, N. E. Piskunov, V. G. Klochkova, *et al.*, Preprint No. 169, SAO RAN (Special Astrophys. Obs., 2002).

21. V. E. Panchuk, M. V. Yushkin, and I. D. Naĭdenov, Preprint No. 179, SAO RAN (Special Astrophys. Obs., 2003).

22. G. A. Galazutdinov, Preprint No. 92, SAO (Special Astrophys. Obs., 1992).

23. V. G. Klochkova, E. L. Chentsov, N. S. Tavolzhskaya, and G. A. Proskurova, Preprint No. 183 (Special Astrophys. Obs., 2003).

24. J. M. Marlborough, Astrophys. J. **156**, 135 (1969).

25. J. I. Castor, L. F. Smith, and D. van Blerkom, Astrophys. J. **159**, 1119 (1970).

26. A. P. Bernat and D. L. Lambert, Publ. Astron. Soc. Pac. **90**, 520 (1978).

27. A. Lèbre and D. Gillet, Astron. Astrophys. **255**, 221 (1992).

28. B. Wolf, O. Stahl, M. J. H. de Groot, and C. Sterken, Astron. Astrophys. **99**, 351 (1981).

29. F. Scappini, S. Casu, C. Cecchi-Pestellini, and M. Olberg, Mon. Not. R. Astron. Soc. **337**, 495 (2002).

30. S. P. Souza and B. L. Lutz, Astrophys. J. **216**, L49 (1977).

31. R. Gredel and G. Munch, Astron. Astrophys. **285**, 640 (1994).

32. F. H. Chaffee, Jr. and R. E. White, Astrophys. J., Suppl. Ser. **50**, 169 (1982).

33. R. Gredel, J. H. Black, and M. Yan, Astron. Astrophys. **375**, 553 (2001).

34. B. Bohannan and P. S. Conti, Astrophys. J. **204**, 797 (1976).

35. J. Brand and L. Blitz, Astron. Astrophys. **275**, 67 (1993).

36. R. M. Humphreys, Astrophys. J. Suppl. **38**, 309 (1978).

37. D. Hoffleit and C. Jaschek, *The Bright Stars Catalogue* (Yale Univ. Observ., 1982).

38. D. Hoffleit, M. Saladyga, and P. Wlasuk, *Supplement to the Bright Stars Catalogue* (Yale Univ. Observ., 1983).

39. R. J. Reynolds, Astrophys. J. **268**, 698 (1983).

40. T. M. Dame, D. Hartmann, and P. Thaddeus, Astrophys. J. **547**, 792 (2001).

41. T. G. Sitnik, A. M. Mel'nik, and V. V. Pravdikova, Astron. Zh. **78**, 40 (2001) [Astron. Rep. **45**, 34 (2001)].

42. B. J. McCall, K. H. Hinkle, T. R. Geballe, *et al.*, Astrophys. J. **567**, 391 (2002).

43. L. M. Hobbs, Astrophys. J. **157**, 135 (1969).

44. B. J. McCall, D. G. York, and T. Oka, Astrophys. J. **531**, 329 (2000).

45. B. Wolf and O. Stahl, Astron. Astrophys. **235**, 340 (1990).

46. O. Stahl, T. Gaeng, C. Sterken, *et al.*, Astron. Astrophys. **400**, 279 (2003).

Translated by N. Samus'

Parameters of V404 Cyg—A Black-Hole Binary

A. M. Cherepashchuk[1,2], N. V. Borisov[3],
M. K. Abubekerov[1], D. K. Klochkov[1], and É. A. Antokhina[2]

[1]*Moscow State University, Vorob'evy gory, Moscow, 119899 Russia*
[2]*Sternberg Astronomical Institute, Universitetskiĭ pr. 13, Moscow, 119899 Russia*
[3]*Special Astrophysical Observatory, Nizhniĭ Arkhyz, Russia*
Received March 15, 2004; in final form, May 27, 2004

Abstract—We present the results of spectroscopic observations of the X-ray binary V404 Cyg obtained on the 6-m telescope of the Special Astrophysical Observatory in 2001−2002. We have used a statistical approach to interpret the radial-velocity curve of V404 Cyg. We derived the dependence of the mass of the X-ray emitting component m_x on the mass of the optical component m_v via an analysis of the radial-velocity curve based on profiles of the CaI 6439.075 Å absorption line synthesized in a Roche model. Using the orbital inclination estimated from the ellipticity of the optical component, $i = 54°−64°$, and the component-mass ratio $q = m_x/m_v = 16.7$ found from the rotational broadening of the spectral lines, we obtain $m_x = 10.65 \pm 1.95 \ M_\odot$ for the mass of the black hole. © *2004 MAIK "Nauka/Interperiodica"*.

1. INTRODUCTION

The X-ray nova GS 2023+338 was first discovered by the Ginga space probe during an outburst on May 22, 1989 [1]. This discovery was subsequently confirmed by Sunyaev *et al.* [2]. During the outburst, the magnitude of GS 2023+338 changed from $V \sim 18.3^m$ to $V = 11.6^m$. Soon afterward, an optical counterpart to the X-ray source was identified: V404 Cyg, which had been classified as a nova after an outburst in 1938 [3, 4].

The X-ray nova V404 Cyg contains a K0IV optical subgiant that fills its Roche lobe and a black hole that accretes matter from an accretion disk. The mass function of the optical star in V404 Cyg is $f_v = 6.08 \pm 0.06 \ M_\odot$ [5]; this is much higher than the limiting mass for neutron stars, providing evidence that the compact component in the system is a black hole. The absence of X-ray pulsations from the compact object prevents the direct determination of the mass of the optical component. Estimates of the mass of the optical star based on its spectral type vary from $0.5 \ M_\odot$ to $1.0 \ M_\odot$ [6].

Current estimates of the parameters of the X-ray source are not very accurate. Based on the I light curve, the range of possible orbital inclinations was determined to be $46°−73°$ and the component-mass ratio to be $q = m_x/m_v = 8−12$ [7]. The measured semi-amplitude of the radial velocity variations, $K_v = 211 \pm 4$ km/s, yields for the mass function of the optical star $f_v = 6.3 \pm 0.3 \ M_\odot$. Assuming that the mass of the subgiant is close to $1.0 \ M_\odot$, Wagner

et al. [7] concluded that the mass of the compact object is $8−12 \ M_\odot$.

A more accurate semi-amplitude for the radial velocity of the optical star was found in [5]: $K_v = 208.5 \pm 0.7$ km/s; this corresponds to the mass function $f_v = 6.08 \pm 0.06 \ M_\odot$ quoted above. The component-mass ratio $q = 16.7 \pm 1.3$ was estimated from the rotational broadening of lines of metals at $6400−6600$ Å. Assuming that the highest possible orbital inclination is $80°$ (as follows from the absence of X-ray eclipses [8]) and that the mass of the optical star is $0.2−1.3 \ M_\odot$, we obtain for the mass of the compact object $7−24 \ M_\odot$.

Analysis of the K light curve of V404 Cyg yields the orbital inclination $i = 52°−60°$ [6]. Using the component-mass ratio $q = 16.7$ [5] and the mass of the optical component $0.5−1.0 \ M_\odot$, we find for the mass of the compact object $10−15 \ M_\odot$.

Analysis of the H light curve of V404 Cyg yields $i = 59°−73°$ [9]. For this range of inclinations, the mass of the black hole does not exceed $12.5 \ M_\odot$. For the component-mass ratio $q = 16.7$, the mass of the black hole is close to $9.5 \ M_\odot$.

The R light curve combined with the spectroscopic component-mass ratio $q = 16.7$ [5] gives $i = 56° \pm 2°$ [10]; variability of the light curve on a time scale of six hours was reported in this same paper. Six-hour variability of the Hα profile is also observed, but the brightness and Hα variations of the system are not correlated [11, 12]. Hynes *et al.* [13] describe the growth and decline of the equivalent width and

Table 1. Spectroscopic observations of V404 Cyg

Date	UT	Exposure, s	Number of spectra	Spectral interval, Å	Resolution, Å
July 12, 2001	18:07−20:30	2700	3	5700−8200	5.5
July 14, 2001	18:52−20:26	2700	2	5700−8200	5.5
July 15, 2001	20:20−21:53	2700	2	5700−8200	5.5
July 16, 2001	21:09−22:40	2700	2	5700−8200	5.5
June 14, 2002	17:35−20:14	1800	5	5500−6800	3.0
July 9, 2002	18:25−19:35	1800	2	5500−6800	3.0
July 10, 2002	18:43−20:20	1800	3	5500−6800	3.0
July 11, 2002	16:52−20:02	1800	6	5500−6800	3.0
July 12, 2002	18:56−19:57	1800	2	5500−6800	3.0

variations of the Hα emission profile on time scales down to $\sim$1−2 h. Pavlenko *et al.* [10] include fluctuations of the photoionizing flux from the compact object due to local flares in the accretion disk or the disk corona among possible origins for the variation of the Hα emission equivalent width [13], however, the mechanism underlying the fast variations of the Hα equivalent width is not known with certainty. The asymmetry of the Hα emission wings likewise remains poorly understood (for more details see [13]).

Our aim was to more accurately determine the radial-velocity curve of the X-ray nova V404 Cyg and

Table 2. Observed barycentric radial velocities of V404 Cyg (adopted zero Julian epoch is $JD_0 = 2448813.873$ [5])

Phase	Radial velocity, km/s
0.229	187.10
0.295	195.90
0.365	161.20
0.387	139.80
0.535	−58.39
0.606	−111.09
0.696	−198.10
0.770	−212.50
0.930	−68.42

the parameters of the close binary system, as well as study the short-time-scale variability of the Hα emission profile.

2. OBSERVATIONAL DATA

Two sets of spectroscopic observations of V404 Cyg were obtained using the 6-m telescope of the Special Astrophysical Observatory between July 12 and 16, 2001 and between June 11 and July 12, 2002. The observations were carried out at the primary focus using a UAGS high-power, long-slit spectrograph and a PM1024 CCD with 1024×1024 pixels and a pixel size of 24×24 μm. In 2001, we used a diffraction grating with a dispersion of 651 lines/mm, yielding an inverse linear dispersion of 3.1 Å/pixel in the spectral interval studied, 5700−8200 Å. The resolution of the resulting spectrograms was 5.5 Å.

In 2002, we used a R1305/17 diffraction grating with a dispersion of 1305 lines/mm, providing an inverse linear dispersion of 1.5 Å/pixel and a resolution of 3.0 Å at 5500−6800 Å. A log of the observations is given in Table 1.

All the spectra were calibrated against a HeNe light source. The spectra were reduced using the MIDAS package, including standard flat fielding, background subtraction, bias correction, and elimination of "hot" pixels. The single white dwarf BD+284211 was used as a spectrophotometric standard for all the spectrograms. The K0IV star HR8857 [5] was used as a radial-velocity standard.

The radial velocities of V404 Cyg were derived from the shift of blends at 6400−6520 Å relative to the
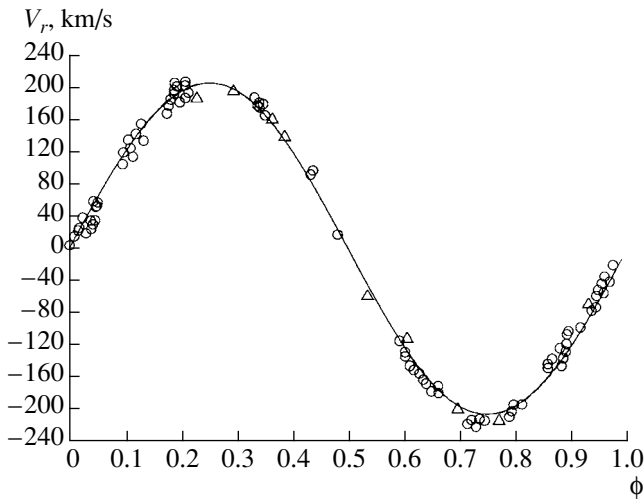
Fig. 1. Folded observed radial-velocity curve of the optical component of V404 Cyg. The open circles show the observed radial velocities derived by Casares and Charles [5] from absorption lines of metals, while the open triangles show the radial velocities found in the present study. The solid curve is the theoretical radial velocity curve for the Roche model based on the synthesized CaI 6439.075 Å absorption line profile assuming $m_x = 10.46\ M_\odot$, $m_v = 0.7\ M_\odot$, and $i = 59°$ (the remaining parameters are listed in Table 3); no correction for the response function has been made. The dashed curve shows the theoretical radial-velocity curve for a point-mass model with $m_x = 10.46\ M_\odot$, $m_v = 0.7\ M_\odot$, and $i = 59°$. This latter curve nearly coincides with the curve for the Roche model.

Fig. 2. Radial velocities averaged over phase intervals (filled circles). For comparison, theoretical radial-velocity curves for the Roche model (solid) and point-mass model (dashed) for the case $m_x = 10.46\ M_\odot$, $m_v = 0.7\ M_\odot$, and $i = 59°$ are shown.

blends in the same wavelength interval of the radial-velocity standard HR 8857. Table 2 gives the observed radial velocities of the optical component of V404 Cyg corrected for the Earth's motion and the systemic velocity.

We constructed the folded radial-velocity curve using our spectroscopic data along with the radial velocities from [5], which were derived from the shift for the wavelength interval 6212−6605 Å relative to this same interval in the spectrum of the radial-velocity standard, HR 8857. The folded curve enabled us to determine the orbital period of the V404 Cyg binary more precisely. We adopted $JD_0 = 2448813.873$ for the zero Julian epoch [5]. The new orbital period, $P_{orb} = 6\overset{d}{.}4715 \pm 0.0001$, agrees with the old value, $P_{orb} = 6\overset{d}{.}4714 \pm 0.0001$ [5], within the errors.

The folded observed radial-velocity curve based on our spectroscopic data and the data of [5] is shown in Fig. 1. The radial velocities were averaged over phase intervals to reduce the influence of random errors (Fig. 2). Since the observed radial velocities are not distributed in phase very uniformly, the rms deviation of the mean radial velocity at phase 0.508

is 37.80 km/s (or 18.1% of the radial-velocity semi-amplitude). This large rms deviation is due to the large gradient of the regular radial-velocity variations near phase 0.5. Since the rms deviation of the observed radial velocity σ_{V_r} at phase 0.508 is much larger than in other phase intervals (where it is $\sim$2−3% of the radial-velocity semiamplitude; Fig. 2), and thus gives rise to an appreciable "perturbation" of the residuals [see (1) below], we excluded the mean observed radial velocity at phase 0.508 when fitting the mean radial-velocity curve.

3. FITTING OF THE MEAN RADIAL-VELOCITY CURVE

The optical component of V404 Cyg fills its inner Roche lobe. The tidal action of the relativistic companion makes the shape of the optical star non-spherical. The side of the optical component facing the relativistic object is heated by the incident X-ray emission. Therefore, we fit the mean radial velocities using a Roche model that is able to take into account this interaction between the components to some extent. The parameters of the Roche model for the X-ray binary V404 Cyg are given in Table 3.

The presence of observable X-ray emission from the V404 Cyg binary provides evidence that the K0IV optical star fills its Roche lobe. Since this star fills its Roche lobe over a time determined by its nuclear evolution time scale, which is $\sim 10^{10}$ yr, the orbit of the close binary has enough time to circularize, and the rotation of the optical component becomes

Table 3. Numerical input parameters for the synthesis of the radial-velocity curves of the optical component of V404 Cyg in the Roche model

P, day	6.4715	Period
e	0.0	Eccentricity
i, deg	54, 59, 64	Orbital inclination
μ	1.0	Roche lobe filling factor for optical component
f	1.0	Ratio of the rotational velocity of the optical star to the synchronous rotational velocity
T_{eff}, K	5500	Effective temperature of the optical component
β	0.08	Gravitational darkening coefficient
k_x	0.03	Ratio of the X-ray luminosity of the relativistic component and bolometric luminosity of the optical component, L_x/L_v
A	1.0	Coefficient of reprocessing of incident X-ray radiation
u	0.5	Limb-darkening coefficient

synchronous with the orbital motion. Therefore, our calculations assume that the orbit of V404 Cyg is circular and the ratio of the spin and orbital rotational velocities is $f = 1.0$.

We consider the masses of both components and the orbital inclination of V404 Cyg to be unknown parameters. We found the solution via a step-by-step search through the parameter values considered. We obtained a set of masses for the compact object m_x for masses of the optical component m_v of 0.5 $M_\odot$, 0.7 $M_\odot$, and 0.9 $M_\odot$ and orbital inclinations i of $54°$, $59°$, and $64°$. This yields the dependence of the mass of the compact object on the mass of the optical component and orbital inclination. The orbital inclinations were selected based on earlier fitting of the R, K, and H light curves of the close binary, which gave the estimates $56° \pm 2°$ [10], $56° \pm 4°$ [6], and $59° - 73°$ [9], respectively. The statistical adequacy of the model was tested at the $\alpha = 5\%$ significant level.

Since the radial velocity of the optical component was determined from absorption lines of metals at $6200-6500$ Å both in the present study and in [5], our theoretical radial velocities are based on synthesized profiles of the CaI 6439.075 Å absorption line. Since absorption lines of metals in the spectrum of the optical component of V404 Cyg have small widths (~ 1 Å), the theoretical radial-velocity curves were computed from the CaI 6439.075 Å profile convolved with a Gaussian instrumental profile with a full width at the half maximum of FWHM $= 0.5$ Å. This FWHM was adopted because most of the radial velocities included in the folded curve (Fig. 2) were

derived from spectra obtained with an instrumental FWHM $= 0.5$ Å [5]. For comparison purposes, we also fit the observed mean radial-velocity curve of V404 Cyg using synthesized CaI 6439.075 Å profiles without convolving with a response function. Figure 3 shows the synthesized CaI 6439.075 Å absorption profiles at orbital phases of 0.00 and 0.25 for both cases.

The residual differences between the mean observed and theoretical radial-velocity curves were computed as

$$\Delta(m_x) = \frac{\sum_{j=1}^{M}(n_j - 1)}{M} \frac{\sum_{j=1}^{M} n_j (V_j^{teor} - \bar{V}_j^{obs})^2}{\sum_{j=1}^{M} n_j(n_j - 1)\sigma_j^2}, \quad (1)$$

where $\bar{V}_j^{obs}$ is the observed radial velocity averaged over a phase interval centered at $\bar{\phi}_j$, V_j^{teor} is the theoretical radial velocity at the same phase, σ_j is the rms deviation of $\bar{V}_j^{obs}$ from the observed radial velocity in the phase interval with its center at $\bar{\phi}_j$, M is the number of phase intervals, and n_j is the number of individual averaged observations in phase interval j.

The value of $\Delta(m_x)$ is distributed according to a Fisher law $F_{M,\sum_{j=1}^{M}(n_j-1),\alpha}$ [14]. We can find the set of acceptable values for m_x for a given significance level α and a specified value of m_v. This set contains
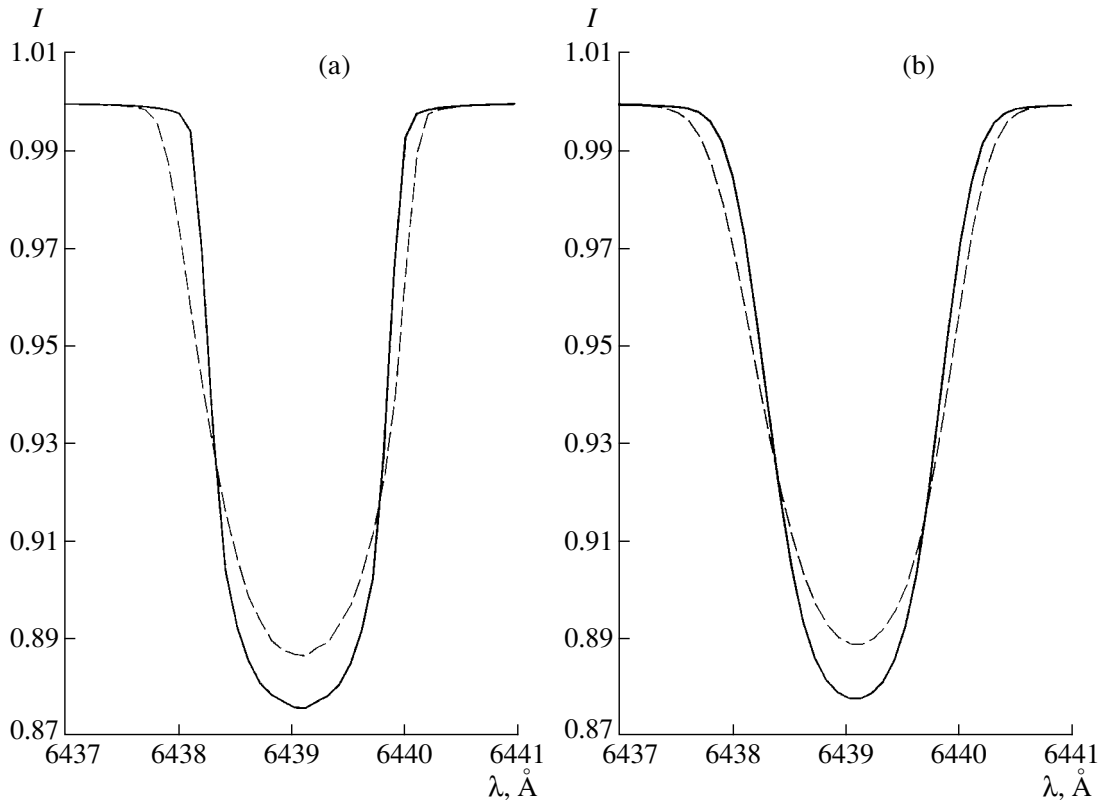
Fig. 3. (a) Synthetic profiles of the CaI 6439.075 Å absorption line calculated in the Roche model for $m_x = 10.46\ M_\odot$, $m_v = 0.7\ M_\odot$, and $i = 59°$ (for the remaining parameters see Table 3) at orbital phases 0.00 (solid) and 0.25 (dashed). (b) The same profiles convolved with a Gaussian response function with FWHM $= 0.5$ Å. The profiles at orbital phase 0.25 are corrected for the Doppler shift.

values of m_x obeying the condition

$$\Delta(m_x) \le F_{M, \sum\limits_{j=1}^{M}(n_j-1),\alpha}.$$

The algorithm used to compute the theoretical absorption-line profiles and theoretical radial-velocity curves is described in [15, 16], and we do not present it here. Note, however, that computing the local shape of the CaI 6439.075 Å absorption profile using this algorithm requires the solution of the radiative-transfer equation for each area element. This differs from the algorithm for synthesizing radial-velocity curves from the Hγ absorption profile applied in [17], which included computation of the local shape of the profile from an area element via the interpolation of tabulated values of this profile given by Kurucz [18].

The residuals found by fitting the mean observed radial-velocity curve are shown in Fig. 4; this figure shows that it is important to take into account the instrumental profile. The theoretical radial-velocity curves computed without including the effect of the response function on the synthesized CaI 6439.075 Å

absorption profile are not in agreement with the observed data: the close-binary models are rejected at the $\alpha = 5\%$ significance level (Fig. 4b).

Table 4 presents the relation between the component masses for various orbital inclinations derived in the Roche model based on the synthesized CaI 6439.075 Å profiles convolved with the response function. The same relation without this convolution is presented in Table 5. The results are shown in graphical form in Fig. 5. Since the residual differences between the theoretical and observed radial-velocity curves are unacceptably large at the $\alpha = 5\%$ significance level when the response function is not taken into account, the confidence intervals for the mass of the compact object are omitted in Table 5 and Fig. 5b.

4. DEPENDENCE OF THE SHAPE OF THE RADIAL-VELOCITY CURVE OF V404 Cyg ON ORBITAL INCLINATION

We carried out special calculations of the theoretical radial-velocity curves in the Roche model to study the dependence of the shape of the radial-velocity curve on the orbital inclination of V404 Cyg. The
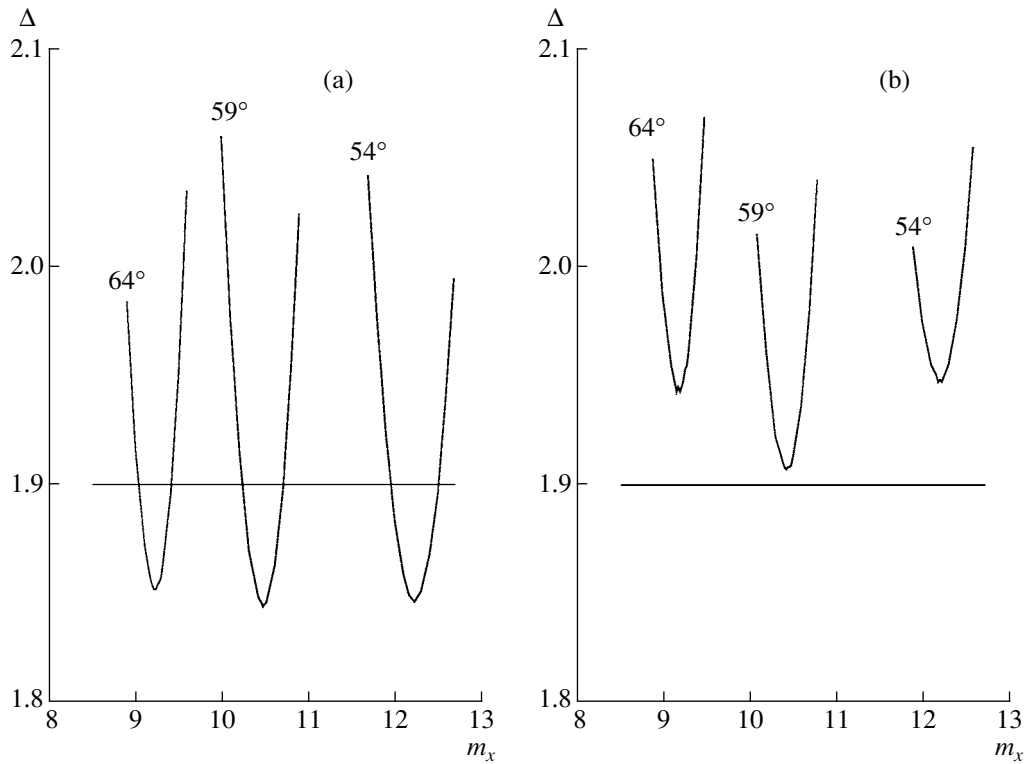
Fig. 4. (a) Residuals for the fitting of the radial-velocity curve derived in the Roche model for $m_v = 0.7\ M_\odot$ and orbital inclinations $i = 54°$, $59°$, and $64°$ (for the remaining parameters see Table 3). The curve is based on the synthesized CaI 6439.075 Å profile and includes the effect of a response function with FWHM $= 0.5$ Å. (b) Same as (a) but without the effect of the response function.

mass of the optical star was taken to be $m_v = 0.7\ M_\odot$, and the mass of the black hole to be $m_x = 10\ M_\odot$. Calculations were carried out for inclinations $i = 40°$, $54°$, $64°$, and $80°$, with the remaining parameters of the Roche model unchanged (see Table 3). Since the radial-velocity semiamplitude K_v increases with the orbital inclination, the computed theoretical radial velocity curves were normalized to the maximum radial velocity in the phase interval 0.0–0.5. The difference in the shapes of the radial-velocity curves is maximum at phase $\phi = 0.36$. The difference of the radial-velocity curves for $i = 40°$ and $i = 80°$ was ~0.3% of the semiamplitude K_v when the response function was taken into account when computing the synthesized CaI 6439.075 Å profiles and ~0.5% when the response function was not taken into account. For comparison, the difference in the shape of the radial-velocity curves for close binaries with parameters similar to that of Cyg X-1 ($q = m_x/m_v \simeq 0.5$) was ~3% of K_v when the orbital inclination was varied from $i = 40°$ to $i = 80°$ [19].

In the case of the X-ray nova V404 Cyg, increasing the orbital inclination from $i = 54°$ to $i = 64°$ resulted in variations of the shape of the radial-velocity curve of the semiamplitude K_v by ~0.10% or

~0.13% when the CaI 6439.075 Å profile was or was not convolved with the response function. Because the shape of the radial-velocity curve varies little with such variations of the orbital inclination, the residual minima for the different inclinations do not differ as much as in the case of Cyg X-1 [19, Fig. 5] (Fig. 4).

The rms error σ_{Vr} of the observed mean radial-velocity curve of V404 Cyg is ~(2–3)% of its semiamplitude K_v, preventing estimation of the orbital inclination as was done for Cyg X-1 [19]. However, the Roche model can be used to estimate the orbital inclination from the radial-velocity curve, since the minimum residuals are different for different inclinations (Fig. 4). This is especially clearly visible in Fig. 4b. For successful estimation of the orbital inclination of V404 Cyg from the radial-velocity curve, σ_{V_r} must be ~0.10% of K_v or, in absolute units, ~0.2 km/s. Therefore, further high-quality spectroscopic observations of V404 Cyg are promising for this purpose.

5. COMPONENT MASSES IN V404 Cyg

The component-mass ratio $q = m_x/m_v$ found from the rotational broadening of metal lines in the spectrum of the optical component of V404 Cyg is 16.7 [5]. By drawing the corresponding line in the

Table 4. Dependence of the m_x on m_v in the Roche model. The effect of the response function on the synthesized CaI 6439.075 Å profile is taken into account

$m_v, M_\odot$	$m_x, M_\odot$		
	$i = 54°$	$i = 59°$	$i = 64°$
0.5	$11.87^{+0.24}_{-0.22}$	$10.13^{+0.21}_{-0.23}$	$8.87^{+0.22}_{-0.19}$
0.7	$12.22^{+0.30}_{-0.27}$	$10.46^{+0.25}_{-0.23}$	$9.21^{+0.21}_{-0.18}$
0.9	$12.56^{+0.28}_{-0.27}$	$10.78^{+0.26}_{-0.25}$	$9.53^{+0.20}_{-0.19}$

Table 5. Dependence of m_x on m_v in the Roche model. The effect of the response function on the synthesized CaI 6439.075 Å profile has not been included

$m_v, M_\odot$	$m_x, M_\odot$		
	$i = 54°$	$i = 59°$	$i = 64°$
0.5	11.83	10.10	8.86
0.7	12.20	10.42	9.18
0.9	12.54	10.77	9.48

plot showing the relation between the component masses (Fig. 5), we find that, for $i = 54°-64°$, the masses of the black hole and optical star are $m_x = 8.7-12.6\ M_\odot$ and $m_v = 0.52-0.76\ M_\odot$. Thus, the mean mass of the black hole in V404 Cyg is $10.65 \pm 1.95\ M_\odot$.

6. VARIABILITY OF THE Hα EMISSION PROFILE

Casares *et al.* [11] were the first to point out the S-wave variability of the Hα emission profile; they estimated the period of this variability to be 5.7 h. Later, the more accurate period of 5.656 h was found from a larger number of spectrophotometric observations obtained in 1990−1991 [12].

The most detailed study of the short-time optical variability and behavior of the Hα line in V404 Cyg was carried out by Hynes *et al.* [13], who found a qualitative correlation between the behavior of the continuum and the Hα equivalent width. An increase of the continuum is observed with increase in the Hα equivalent width. Both the continuum from the accretion disk and the Hα flux vary by more than a factor of two over one to two hours.

During the nights of June 14 and July 11, 2002, we obtained five and six spectra at 5500−6800 Å (Table 1), enabling us to study the behavior of the Hα line on time scales ~30 min. The Hα emission profiles are shown in Fig. 6, and the profiles averaged over a night are shown in Fig. 7. We determined the mean profile by taking the arithmetic mean of all Hα profiles obtained during a night. Figures 6 and 7 show that the emission profile not only experiences significant variations during the course of a night, but also varies strongly from night to night.

We investigated the short-term variability of the Hα emission profile. We estimated the deviation of a given Hα profile from the profile averaged over the night using the Fisher statistical criterion, averaging the relative intensities of the Hα emission lines over wavelength intervals of ~5 Å. The residuals were computed as

$$\Delta(I^{obs}(t)) = \frac{\sum\limits_{j=1}^{M}(n_j - 1)}{M} \tag{2}$$
$$\times \frac{\sum\limits_{j=1}^{M} n_j(I_j^{mean} - \bar{I}_j^{obs}(t))^2}{\sum\limits_{j=1}^{M} n_j(n_j - 1)\sigma_j^2},$$

where $\bar{I}_j^{obs}$ is the observed mean relative intensity of the Hα line in the wavelength interval centered at $\bar{\lambda}_j$ at time t, I_j^{mean} is the mean relative intensity of the averaged Hα line profile in the wavelength interval centered at $\bar{\lambda}_j$ at time t, σ_j is the rms deviation of $\bar{I}_j^{obs}(t)$ in a given wavelength interval centered at $\bar{\lambda}_j$, M is the average number of wavelength intervals, and n_j the number of averaged relative intensities in the wavelength interval j.

We found the times t when the Hα profile deviated significantly from the nightly averaged profile for a specified significance level α. The deviation of a profile from the mean profile was considered to be significant if

$$\Delta(I^{obs}(t)) \geq F_{M, \sum\limits_{j=1}^{M} (n_j-1), \alpha}.$$

We considered the $\alpha = 5\%$ significance level for our analysis. The results are presented in Fig. 8, which shows that significant deviations from the mean level occurred on a time scale of about two hours on the night of June 14, 2002, and on a time scale of ~0.5−1 h on the night of July 11, 2002. The behavior of the line is striking. A phase of intense growth of the emission line component can suddenly change into a decrease, and vice versa. The change of phases may occur in ~0.5 h (Figs. 6b and 8b).
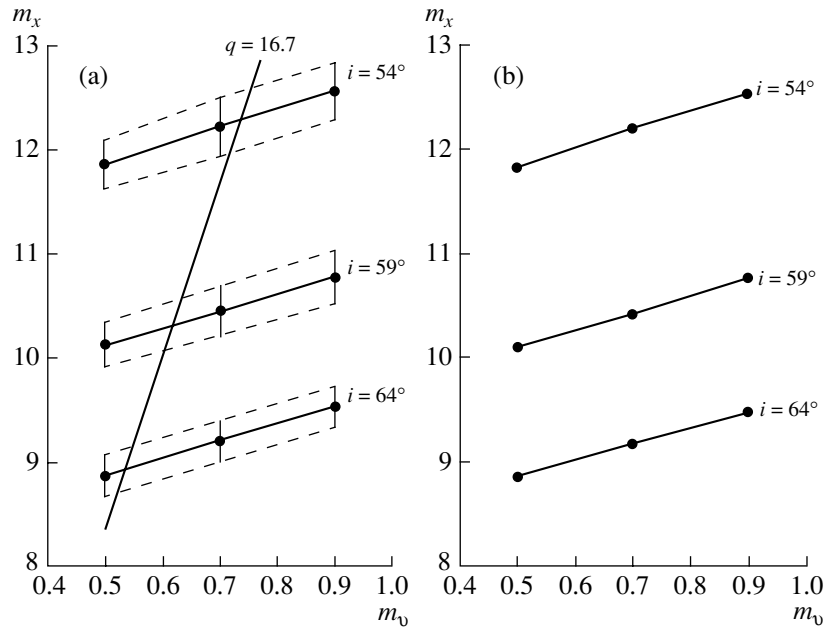
Fig. 5. (a) Relation between the masses of the compact object and optical star in V404 Cyg derived via analysis of the mean radial-velocity curve in the Roche model based on the CaI 6439.075 Å profile and convolved with a Gaussian response function with FWHM = 0.5 Å. The straight line corresponds to the component-mass ratio $q = m_x/m_v = 16.7$ [5]. (b) Same as (a) without including the effect of the response function.
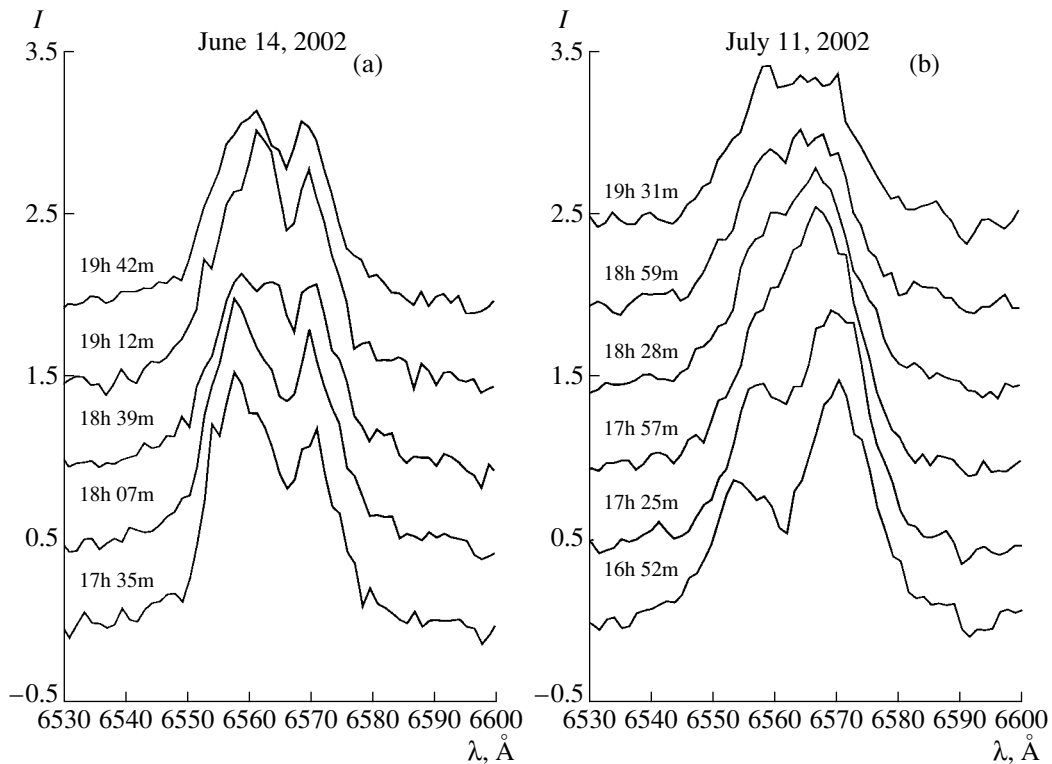
Fig. 6. Hα emission profiles obtained on (a) June 14, 2002 at orbital phase $\phi = 0.365$ and (b) July 11, 2002 at orbital phase $\phi = 0.535$. For ease of viewing, the profiles have been shifted vertically relative to one another.
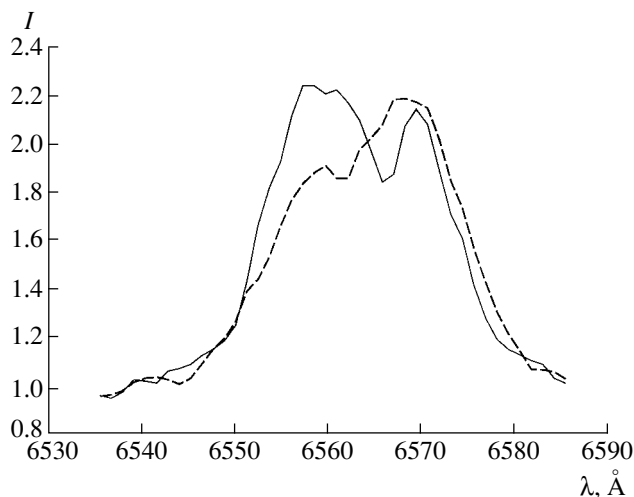
Fig. 7. Mean Hα emission profiles obtained during the nights of June 14, 2002 at orbital phase $\phi = 0.365$ (solid) and July 11, 2002 at orbital phase $\phi = 0.535$ (dashed).

Fig. 8. Deviations of the Hα emission profile from the nightly averaged profile on (a) June 14, 2002 at orbital phase $\phi = 0.365$ and (b) July 11, 2002 at orbital phase $\phi = 0.535$. The straight lines show critical levels of the residuals for the Fisher criterion for the $\alpha = 5\%$ significance level.

The origin of the Hα variability has not been established. Proposed sources of the S-wave variability include the motion of a hot spot in the accretion disk [12], chromospheric activity of the optical component, and reconnection of magnetic field lines in the accretion disk [13]. No unique mechanism for the S-wave short-time-scale variability of the Hα emission in V404 Cyg is known. Correct interpretation of the data requires a long series of observations with high time resolution, and studies in this direction should be continued.

7. CONCLUSION

The main result of our study is our derivation of the relation between the masses of the two components in the X-ray nova V404 Cyg in a Roche model for orbital inclinations $i = 54°-64°$. Combined with the spectroscopically determined component-mass ratio $q = 16.7$ [5], these dependences yield $m_x = 10.65 \pm 1.95\ M_\odot$ for the mass of the black hole and $m_v = 0.64 \pm 0.12\ M_\odot$ for the mass of the optical star.

It is not currently possible to constrain the orbital inclination of V404 Cyg using the observed mean radial-velocity curve. The accuracy required for this is $\sim 0.10\%$ of the radial-velocity semiamplitude K_v, while the accuracy of the observed mean radial-velocity curve is $\sim (2-3)\%$ of K_v. Thus, the averaged effects of the orbital variability of the absorption-line profiles contributing to the radial-velocity curves of low-mass X-ray binary systems ($q \gg 1$) influence the shape of the line relatively weakly. Therefore, the orbital inclinations of low-mass X-ray binary systems must be determined directly from the orbital variability of absorption-line profiles [20, 21]. This requires

high-quality spectra of V404 Cyg with resolution $R \simeq 50\,000$ on the largest $8-10$ m new-generation telescopes.

We also determined the typical time scales for variability of the Hα emission profile. Significant variations of the profile shape and equivalent width occur on time scales of $\sim 0.5-2$ h. The origin of variability of the photoionizing flux has not been established [13], and studies of this problem require further spectroscopic observations of V404 Cyg.

REFERENCES

1. F. Makino *et al.*, IAU Circ., No. 4782 (1989).
2. R. Sunyaev *et al.*, IAU Circ., No. 4800 (1989).
3. B. G. Marsden, IAU Circ., No. 4783 (1989).
4. R. M. Wagner, T. J. Kreidl, S. B. Howell, *et al.*, IAU Circ., No. 4797 (1989).
5. J. Casares and P. A. Charles, Mon. Not. R. Astron. Soc. **271**, L5 (1994).
6. T. Shahbaz, F. A. Ringwald, J. C. Bunn, *et al.*, Mon. Not. R. Astron. Soc. **271**, L10 (1994).

7. M. R. Wagner, T. J. Kreidl, S. B. Howell, and S. G. Starrfield, Astrophys. J. **401**, L97 (1992).

8. Y. Tanaka, in *Proceedings of the 23rd ESLAB Symposium on Two Topics in X-Ray Astronomy*, Ed. by H. J. Battrick (ESA Publ. Div., SP-296, 1989), p. 1.

9. D. Sanwal, E. L. Robinson, E. Zhang, *et al.*, Astrophys. J. **460**, 437 (1996).

10. E. P. Pavlenko, A. C. Martin, J. Casares, *et al.*, Mon. Not. R. Astron. Soc. **281**, 1094 (1996).

11. J. Casares, P. A. Charles, T. Naylor, and E. P. Pavlenko, Mon. Not. R. Astron. Soc. **265**, 834 (1993).

12. J. Casares and P. A. Charles, Mon. Not. R. Astron. Soc. **255**, 7 (1992).

13. R. I. Hynes, C. Zurita, C. A. Haswell, *et al.*, Mon. Not. R. Astron. Soc. **330**, 1009 (2002).

14. D. Hudson, *Statistics. Lectures on Elementary Statistics and Probability* (Geneva, 1964; Mir, Moscow, 1970).

15. É. A. Antokhina, A. M. Cherepashchuk, and V. V. Shimanskiĭ, Izv. Ross. Akad. Nauk, Ser. Fiz. **67**, 293 (2003).

16. É. A. Antokhina, A. M. Cherepashchuk, and V. V. Shimanskiĭ, Astron. Zh. **81** (2004, in press).

17. É. A. Antokhina and A. M. Cherepashchuk, Astron. Zh. **71**, 420 (1994) [Astron. Rep. **38**, 367 (1994)].

18. R. L. Kurucz, Astrophys. J., Suppl. Ser. **40**, 1 (1979).

19. M. K. Abubekerov, E. A. Antokhina, and A. M. Cherepashchuk, Astron. Zh. **81**, 606 (2004).

20. É. A. Antokhina and A. M. Cherepashchuk, Pis'ma Astron. Zh. **23**, 889 (1997) [Astron. Lett. **23**, 773 (1997)].

21. T. Shahbaz, Mon. Not. R. Astron. Soc. **298**, 153 (1998).

Translated by L. Yungel'son

The Death Lines of Radio Pulsars for Dipolar and Asymmetric Magnetic Fields

E. M. Kantor and A. I. Tsygan

Ioffe Physicotechnical Institute, Russian Academy of Sciences,
Politekhnicheskaya ul. 26, St. Petersburg, 194021 Russia
Received March 23, 2004; in final form, July 15, 2004

Abstract—The effect of curvature of open magnetic-field tubes on the death lines of radio pulsars is studied. The solution is obtained in the framework of a Goldreich−Julian model for both dipolar and asymmetric magnetic fields. The tube-axis curvature can shift the death line appreciably toward either longer or shorter periods. If the field is dipolar and gamma rays are generated by the inverse Compton effect, the formation of secondary plasma is more efficient near the death line. In the case of an asymmetric magnetic field, the generation of radio emission beyond the tube of open field lines is possible. © *2004 MAIK "Nauka/Interperiodica".*

1. INTRODUCTION

The death line of a radio pulsar is the curve in the magnetic-field—period plane separating the regions where radio emission can and cannot be generated. The mechanism for the radio emission is as follows [1, 2]. Electrons are accelerated by the electric field along open magnetic field lines emanating from the polar regions of the pulsar (we shall consider the case of an acute angle between the angular-velocity and magnetic-moment vectors). Next, these electrons produce gamma rays, which, in turn, generate secondary plasma (i.e., electron−positron pairs) due to the presence of a transverse component of the magnetic field. When the primary high-energy particles pass through the secondary plasma, they generate oscillations that result in radio emission. It is commonly believed that a pulsar will no longer emit at radio frequencies if a sufficient amount of secondary plasma cannot be formed.

In the present work, we shall calculate the death lines for an asymmetric magnetic field and compare these results with the case of a dipolar field. The death lines for a dipolar field have already been obtained by other authors (for example, in the recent works [3] and [4]). However, we calculate them again to show that our approximation method gives the same results for the dipolar field as a numerical approach [3]. In addition, we study the effect of stationary plasma in unfavorably bent field lines. When the field is dipolar and gamma rays are formed by the inverse Compton effect, the generation of secondary plasma is more efficient near the death line. In the case of an asymmetric magnetic field, radio emission can be generated beyond the tube of open field lines.

To calculate the death lines, we need information about the electric field accelerating the primary electrons.

In a regime with the free outflow of charges in a Goldreich−Julian model for a rotating neutron star possessing a magnetic field (a radio pulsar), the electric fields in the region of open magnetic field lines are determined by the relativistic effect of inertial reference-frame dragging. This was demonstrated for the case of a dipolar magnetic field by Muslimov and Tsygan [5, 6] and Beskin [7], and for an arbitrary axially symmetric magnetic field by Tsygan [8].

The electric field for the case of curved axes of the tubes of open field lines of a nondipolar magnetic field was calculated by Kantor and Tsygan [9].

We derived the death lines in analytic form. The emission spectra and energy distributions of the secondary plasma were not taken into account, and all calculations were carried out for the characteristic energies.

2. DEATH LINES FOR A DIPOLAR FIELD WITHOUT STATIONARY PLASMA IN THE REGION OF OPEN FIELD LINES

As is known, the electrostatic potential (in a coordinate system rotating with a star) in the region of open dipolar magnetic field lines at distances much less than the light-cylinder radius is [5, 6]

$$\Phi = \frac{1}{2}\kappa\Theta_0^2 \left(\frac{\Omega a}{c} \right) B_0 a (1 - \xi^2) \left(1 - \frac{1}{\eta^3} \right) \cos\chi;$$

$$\cos\chi \neq 0.$$

(1)

Here, $\kappa = (r_g/a)(I/Ma^2)$, where I is the moment of inertia of the star, $r_g = (2GM)/c^2$ is the gravitational radius of a neutron star with mass M, and a is its radius. The parameter κ describes the effect of inertial-frame dragging (described by the metric-tensor component g_{03}) on the electric field near the star; its characteristic value is equal to 0.15. Further, Ω is the angular velocity of the star, B_0 is the amplitude of the magnetic field at the magnetic pole of the star, $\Theta_0 = \sqrt{\Omega a/c}$ is the angular radius of a tube of open field lines at the stellar surface, ξ is the distance from the tube axis normalized to Θ_0, η is the distance from the stellar center normalized to its radius, and χ is the angle between the magnetic moment and angular velocity of the star. We shall not take into account the Schwarzschild terms g_{00} and g_{11} in the metric tensor describing the gravitational field near the rotating neutron star. Therefore, an accelerated electron will acquire the Lorentz factor

$$\gamma = \frac{e\Phi_{dip}}{mc^2} = 10^6 P^{-2} B_{12} \left(1 - \frac{1}{\eta^3}\right) \cos\chi,$$

where P is the period of the radio pulsar in seconds and ξ was taken to be 0.5, since this corresponds to a line with a not very small potential and curvature simultaneously.

The free path of a photon in the magnetic field is determined in the standard way [1, 10]. The photons are emitted by electrons along the magnetic field lines within an angle of about $1/\gamma$. Before a pair is born in a magnetic field with radius of curvature ρ, the photon traverses the path

$$S_{ph} = \frac{0.2mc^2\rho}{\hbar\omega}\frac{B_c}{B}.$$

This expression can be obtained if the integral of the photon absorption coefficient in the magnetic field along the photon trajectory is assumed to be unity. The main contribution to the integral is produced by the final part of the trajectory (where the pair is produced). Therefore, the magnetic field appearing in this formula is the field in the place where the pair is formed. Our estimate is valid for $B < 10^{13}$ G, because it does not take into account the processes considered in [11], such as deflection of the gamma ray by the magnetic field, the formation of a pair in a bound state, and the decay of one of the states of the gamma ray into two photons.

For a dipolar field, the radius of curvature ρ at $\xi = 0.5$ is equal to $2.2 \times 10^8 P^{1/2}$ cm. Therefore,

$$S_{ph} \approx 2 \times 10^9 \frac{mc^2}{\omega\hbar}\frac{P^{1/2}}{B_{12}} \text{ cm.}$$

The photons emitted by the primary electrons will have the following energies. Magnetic curvature

radiation results in gamma rays with characteristic energies $E_{ph} = (3/2)(\gamma^3\hbar c/\rho)$. The inverse Compton scattering of thermal photons on electrons with Lorentz factors $\gamma > mc^2/2kT$ results in gamma rays with energy $E_{ph} = mc^2\gamma$. When $\gamma < mc^2/2kT$, gamma rays with energy $E_{ph} = 2kT\gamma^2$ are generated [12].

The condition for the creation of a pair is [2, 10]

$$B_\perp = B_c \frac{0.2mc^2}{\hbar\omega}.$$

Here, $B_\perp$ is the magnetic-field component perpendicular to the direction of propagation of the gamma ray.

As the gamma ray moves away from the place it is emitted, the angle between the magnetic field and the direction of propagation increases, but the intensity of the field decreases. The transverse component of the field will be maximum at the point $\eta_0 = 1.5\eta$, where η is the distance from the stellar center to the place where the gamma ray is emitted.

The condition $\eta_0 = 1.5\eta$ can be rewritten

$$S_{ph} = \frac{10^{15}(1.5\eta)^3 P^{1/2}}{B_{12}\omega\hbar(\eta)} = \frac{\eta}{2}10^6, \qquad (2)$$

where B_{12} is the magnetic-field intensity at the stellar surface, and $\omega\hbar(\eta)$ is the energy of a photon produced at a distance η from the stellar center.

In the case of inverse Compton scattering by energetic electrons, we have

$$S_{ph} = \frac{10^{15}(1.5\eta)^3 P^{1/2}}{B_{12}5 \times 10^5 \times 10^6 P^{-2} B_{12} \cos\chi \left(1 - \dfrac{1}{\eta^3}\right)}$$

$$= \frac{\eta}{2}10^6.$$

After some manipulation of this equation, we obtain $\eta^2/(1 - 1/\eta^3) = 0.74 \times 10^2 B_{12}^2 P^{-2.5} \cos\chi$. The furthest right line in the $B-P$ plane corresponds to the minimum of the function $\eta^2/(1 - 1/\eta^3)$, i.e., $\eta \approx 1.35$. Therefore, the death line is described by the expression

$$P = 3.6 B_{12}^{0.8}(\cos\chi)^{0.4}. \qquad (3)$$

3. MULTIPLICATION FACTOR FOR THE SECONDARY PLASMA IN A DIPOLAR FIELD WITHOUT STATIONARY PLASMA IN THE REGION OF OPEN FIELD LINES

To determine this multiplication factor, we need to know how many gamma rays are produced by a single primary electron and how many pairs are formed by a single gamma ray. It is obvious that a cascade cannot

develop near the death line, and that one gamma ray cannot produce more than one pair.

The number of gamma rays produced is determined by the integrated probability of gamma ray formation. Gamma rays born very close to the stellar surface cannot form pairs because their energy is insufficient, whereas gamma rays born at very large heights cannot form pairs because the magnetic field decreases with distance from the star. The corresponding boundaries are defined by the condition that the distance from the stellar center to the point where the pair is formed is a factor of 1.5 greater than the distance from the stellar center to the point where the gamma ray is formed. From here on, we shall consider the inverse Compton scattering of thermal photons on fast electrons ($\gamma > mc^2/2kT$), when the gamma ray carries away all the energy of the electron. For this condition to be satisfied, it is necessary that $T_5 P^{0.5}/B_{12} > 1.5$. In the conditions typical for radio pulsars, the probability of photon scattering by an electron somewhere along its entire path is much less than unity.

Photons produced at a resonant cross-section will contribute to the formation of pairs if [12]

$$\gamma_{res} = 10^3 \frac{B_{12}}{T_5} > \frac{1.4 \times 10^4 P^{0.5}}{B_{12}},$$

in other words,

$$\frac{B_{12}^2}{T_5 P^{0.5}} > 14.$$

If this requirement is not satisfied, the number of photons scattered by one electron along the path from r_1 to r_2 is

$$N_\gamma = \int_{r_1}^{r_2} \frac{\frac{\sigma_T \sigma T^4}{c} \left(\frac{mc^2}{kT}\right)^2 \ln\left(\frac{2\gamma kT}{mc^2}\right) dL}{mc^2 \gamma},$$

where $\ln\left(2\gamma kT/mc^2\right)$ is a quantity of the order of unity, and r_1 and r_2 are the upper and lower boundaries for the generation of pair-forming photons. Therefore, we obtain

$$N_\gamma = \int_{r_1}^{r_2} \frac{T_5^2}{2.3 \times 10^3 \gamma} dL.$$

Consequently, the number of gamma rays generated by one electron N_γ when thermal emission is produced by the entire surface of the star is equal to

$$N_\gamma = \frac{7 \times 10^{-4} T_5^2 P^2}{B_{12} \cos\chi}. \tag{4}$$

We can see that the multiplication factor increases near the death line (we assume here that one gamma ray creates one pair, and that the multiplication factor equals N_γ; the condition for the formation of a cascade will be discussed below). If the amplitude of the magnetic field is fixed, the concentration of the secondary plasma increases as P. As a result, the efficiency of radio emission should increase near the death line. The increase in the concentration will be stopped and replaced with a decrease when the height η (the height above which photons created cannot produce pairs) approaches the value $\eta = 2$ (the height at which the flux of thermal photons from the stellar surface is substantially attenuated). This takes place when $P = 3.2 B_{12}^{4/5} \cos^{2/5}\chi$; i.e., the true death line should be within the interval $P = (3.2-3.6) B_{12}^{0.8} \cos^{0.4}\chi$.

We have not taken into account screening of the field by the electron–positron plasma, since the multiplication factor was small (this is valid for moderate temperatures of the stellar surface $T_5 < 10$, where $T_5 = T/10^5$ K).

Let us consider the case when thermal radiation is emitted only by a hot spot in the polar region. Secondary plasma is formed as long as gamma rays creating pairs are produced at heights $z_0 < 0.01 P^{-1/2}$, since the flux of thermal photons is considerably attenuated at heights exceeding the radius of the polar region.

Therefore, the death line will be given by

$$P < 1.35 B_{12}^{2/3} (\cos\chi)^{1/3}. \tag{5}$$

The number of photons produced will be

$$N_\gamma = \frac{1.9 \times 10^{-4} T_5^2 P^{1/2}}{\cos^{1/2}\chi}. \tag{6}$$

Next, let us consider the case when the photons are generated by magnetic curvature radiation. A similar calculation of the death line gives

$$P = 0.16 B_{12}^{4/7} \cos^{3/7}\chi. \tag{7}$$

Let us determine the number of gamma rays emitted per electron that are able to create a pair. Since the generation of secondary plasma becomes efficient in the case of magnetic curvature radiation, screening of the electric field should be taken into account. We shall assume that the electric field is zero everywhere above the point where the first electron–positron pair was born.

The minimum pair-creation height (the height of the gap) in the case of $P > 0.08 B_{12}^{8/17} \cos^{6/17}\chi$ will be $h = 7.5 P^{7/4}/(B_{12} \cos^{3/4}\chi)$, and the Lorentz factor at this height reaches $\gamma(h) = 2.3 \times 10^7 P^{-1/4} \cos^{1/4}\chi$.

To obtain the corresponding expressions for the case $P < 0.08 B_{12}^{8/17} \cos^{6/17} \chi$, the effect of the secondary plasma on the electric field must be taken into account. We shall not consider this case.

A single electron generates the following number of photons that are able to form pairs:

$$N_\gamma \approx \frac{10^6 \gamma(h)\eta_0}{2P^{1/2}c},$$

where $\eta_0 = 1 + z_0$, and z_0 is the height above which the photons can create pairs.

When $h > 0.01P^{-1/2}$, we find

$$N_\gamma = \frac{2.3 \times 10^2 B_{12}^{1/2} \cos^{5/8} \chi}{P^{13/8}}. \quad (8)$$

Since the number of photons we have obtained is much greater than for the inverse Compton effect, it is reasonable to assume that the true death line should be located to the right of the one obtained above. Pairs will not be formed from electrons with the characteristic energy, but they will form from electrons in the high-energy tail of the spectrum, although the number of pairs produced will be decreased by a factor of e^{E/E_0}, where $E_0 = (3/2)(\gamma^3 \hbar c/\rho)$. If we take $E = 10E_0$, the number of pair-forming gamma rays will be decreased by a factor of 2×10^4; i.e., this number will be comparable to that for the inverse Compton effect. The corresponding death line will be described by the expression

$$P = 0.22 B_{12}^{4/7} \cos^{3/7} \chi, \quad (9)$$

which agrees well with the results [4].

If a gamma ray possesses a sufficiently large energy, the electron–positron pair produced will have a large transverse momentum. The momentum of a particle across the magnetic field will be reduced by radiation, and the energy of the photons emitted could be sufficient to generate secondary pairs [13]. Therefore, a cascade can develop. However, this is impossible near the death line, and the multiplication factors will be equal to the number of gamma rays produced by a single electron.

Therefore, the multiplication factors for the dipolar field will be as follows. In the case of the magnetic curvature generation of gamma rays, the multiplication factor is

$$k = \frac{2.3 \times 10^2 B_{12}^{1/2} \cos^{5/8} \chi}{P^{13/8}}$$

if $P > 0.08 B_{12}^{8/17} \cos^{6/17} \chi$ (this is the condition for the absence of a cascade) and the spot under consideration is not very close to the death line.

In the case of inverse Compton scattering of thermal photons from the entire surface of the star, the multiplication factor is

$$k = \frac{7 \times 10^{-4} T_5^2 P^2}{B_{12} \cos \chi}.$$

This is valid for the parameter ranges $0.75 B_{12}^{0.8} \times \cos^{0.4} \chi < P < 3.2 B_{12}^{0.8} \cos^{0.4} \chi$, $P > 2.3 B_{12}^2 / T_5^2$.

In the case of inverse Compton scattering of thermal photons from a hot spot in the polar region, the multiplication factor is

$$k = \frac{1.9 \times 10^{-4} T_5^2 P^{1/2}}{\cos^{1/2} \chi}.$$

This is valid not very close to the death line at $P > 2.3 B_{12}^2 / T_5^2$ and $P > 0.3 B_{12}^{2/3} \cos^{1/3} \chi$.

4. STATIONARY PLASMA IN THE REGION OF OPEN FIELD LINES

Let us consider the electrostatic potential in the region of open magnetic field lines. As is known, there are favorable and unfavorable lines [15]. The potential varies monotonically along favorable lines up to the light cylinder, whereas there are potential wells on unfavorable lines.

The electrostatic potential in the case of a dipolar magnetic field takes the form [6]:

$$\Phi = \frac{1}{2}\Phi_0 \kappa \Theta_0^2 \left(1 - \frac{1}{\eta^3}\right)(1 - \xi^2)\cos\chi$$
$$+ \frac{3}{8}\Phi_0 \Theta_0^3 H(1)\left(\frac{\Theta(\eta)H(\eta)}{\Theta_0 H(1)} - 1\right)$$
$$\times \xi(1 - \xi^2)\sin\chi\cos\phi,$$

where the following notation has been used:

$$\Phi_0 = (a\Omega/c)B_0 a,$$
$$\Theta_0 = \sqrt{\Omega a/cf(1)},$$
$$\Theta(\eta) = \Theta_0 \left(\eta \frac{f(1)}{f(\eta)}\right)^{1/2},$$
$$f(\eta) = -3\left(\frac{\eta}{\varepsilon}\right)^3 \left[\ln\left(1 - \frac{\varepsilon}{\eta}\right) + \frac{\varepsilon}{\eta}\left(1 + \frac{\varepsilon}{2\eta}\right)\right],$$
$$\text{where} \quad \varepsilon = r_g/a \approx 0.4,$$
$$H(\eta) = \frac{1}{\eta}\left(\varepsilon - \frac{\kappa}{\eta^2}\right)$$
$$+ \left(1 - \frac{3}{2}\frac{\varepsilon}{\eta} + \frac{1}{2}\frac{\kappa}{\eta^3}\right)\left\{f(\eta)\left(1 - \frac{\varepsilon}{\eta}\right)\right\}^{-1},$$

ϕ is the azimuth angle in a cylindrical coordinate system whose axis is directed along the tube.
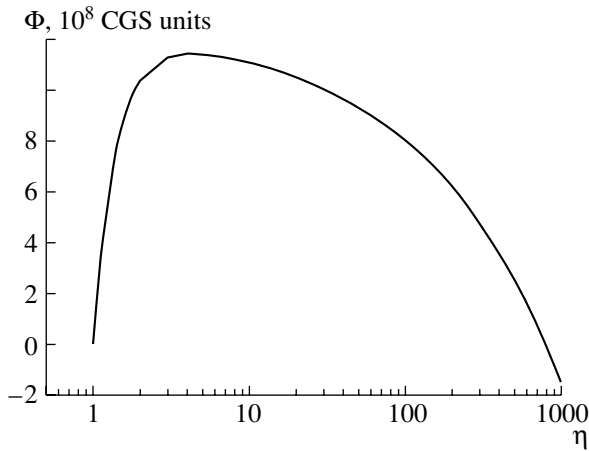
Fig. 1. Behavior of the potential for $\xi = 0.5$, $\chi = 45°$, $\cos\phi = -1$, $P = 1$, $B_{12} = 1$.
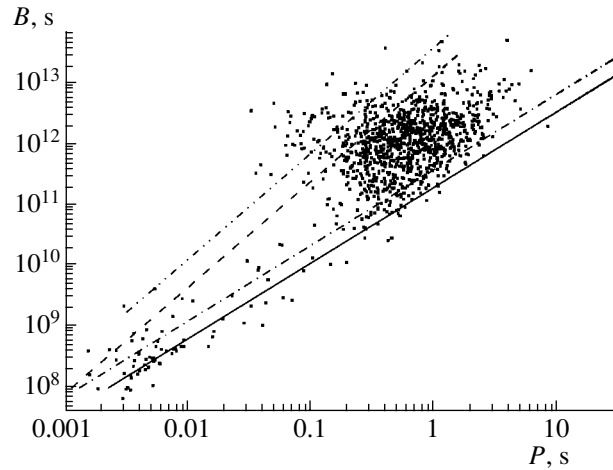

Fig. 2. Calculated death lines of radio pulsars for the magnetic curvature mechanism (dashed), the inverse Compton effect acting on thermal photons from the entire stellar surface with stationary plasma (dash–dot), the inverse Compton effect acting on thermal photons from the entire stellar surface without stationary plasma (solid), and the magnetic curvature mechanism with stationary plasma (dash–double-dot). The observational data (points in the B–P plane) were taken from the unpublished ATNF Pulsar Catalog of Hobbs and Manchester (2003).

At some angles ϕ, the potential will be nonmonotonic; i.e., there will be potential wells (Fig. 1).

If the formation of electron–positron plasma does not proceed very actively, the charged particles will be concentrated in these wells and tend to smooth the potential. Therefore, the following situation will develop in unfavorably bent field lines. The potential is zero at the stellar surface. The next layer is filled with a stationary plasma, and the potential remains zero up to some point, where a potential with an opposite sign relative to the favorable lines appears, which varies monotonically. There is no electron flux from the stellar surface along these lines (we consider the case of an acute angle between the angular velocity of the star and its magnetic moment), but there can be an inverse flow of electrons from the light cylinder. The presence of this stationary plasma with zero potential should decrease the effective cross-section of the tube, and, consequently, the value of the accelerating potential.

If a considerable amount of plasma is formed (at small periods, when magnetic curvature radiation is efficient), the electric field can become zero everywhere above the place where the plasma is formed. Therefore, the potential will be monotonic, and there will be no decrease in the tube cross-section, or, consequently, in the potential. On the other hand, it is also possible that some part of the tube will be filled. We cannot definitely answer which of these cases actually takes place.

Let us consider the influence on the death line of decreasing the cross-section of the tube in which the electrons are efficiently accelerated.

To estimate the electrostatic potential, let us assume that the part of the tube where the electron acceleration takes place possesses a circular cross-section with a radius that is half the radius of the

initial tube. Since the potential depends quadratically on the cross-sectional radius, the electron Lorentz factor should decrease by a factor of four. The death line corresponding to the inverse Compton effect acting on photons from the entire surface of the star will be $P = (1.8–2.1)B_{12}^{0.8}\cos^{0.4}\chi$, that corresponding to the inverse Compton effect acting on photons from a hot spot will be $P = 0.8B_{12}^{2/3}(\cos\chi)^{1/3}$, and that corresponding to magnetic curvature radiation $P = 0.12B_{12}^{4/7}\cos^{3/7}\chi$. These death lines and the corresponding lines without filling taken into account are drawn in Figs. 2 and 3.

5. DEATH LINES IN THE CASE OF BENT TUBES (AN ASYMMETRIC MAGNETIC FIELD)

Let us describe the specific features of bent tubes.

The potential in an asymmetric tube can be expressed [9]

$$\Phi = \frac{\Omega F}{2\pi c}(1 - \xi^2) \qquad (10)$$
$$\times \{[1 - \kappa(1/\eta)^3]\cos\chi + (\kappa - 1)\cos\chi_s\},$$

where F is the magnetic flux through the tube, $\cos\chi_s$ is the cosine of the angle between the angular velocity and the magnetic field near the stellar surface, and $\cos\chi$ is the cosine of the angle between the angular
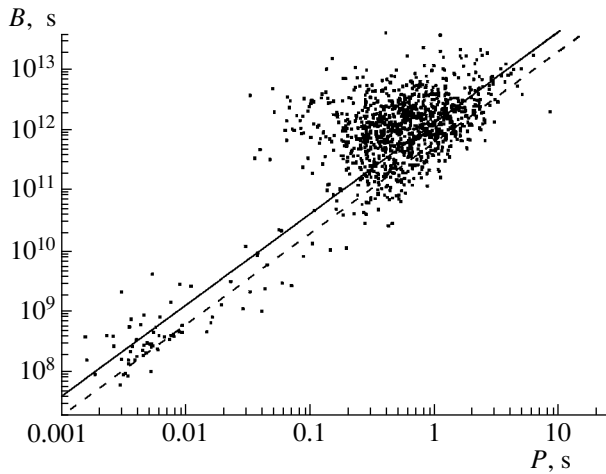
Fig. 3. Same as Fig. 2 for the inverse Compton effect acting on thermal photons from a hot spot in the polar region when stationary plasma is present (solid) and the inverse Compton effect acting on thermal photons from a hot spot in the polar region without stationary plasma (dashed).

velocity and the magnetic field at the point under consideration.

The following model was considered in our previous work [9]. A star with radius a possesses magnetic moment $\mathbf{m}$, so that the field at its magnetic pole is $B_0 = 2m/a^3$. An additional dipole with magnetic moment $\mathbf{m}_1 \perp \mathbf{m}$ is located at a depth $a\Delta$ ($\Delta \approx 0.1$) near the pole of the neutron star, so that its field at the star's pole is equal to $B_1 = m_1/a^3\Delta^3$. Assuming that $B_0 = B_1$ and a favorable axis inclination and tube curvature, we can obtain an increase by a factor of five in the potential and by a factor of 20 in the curvature, compared to the dipolar case. The corresponding potential wells will be shallower, and they will not be filled with stationary charge to the zero potential level. However, we can still describe the filling as a halving of the effective cross-section of the tube.

One characteristic feature of tubes with bent axes is that electron–positron pairs can be produced both inside and outside the tube (in the region of closed field lines). The birth of pairs in the region of closed field lines is possible because, if a photon does not have too large an energy, its path before the formation of a pair can be large enough for it to leave the tube. This path length must satisfy the condition $L > \sqrt{\rho\Theta a\eta}$ (where ρ is the radius of curvature of the tube, and $\Theta a\eta$ is the tube radius). After traversing the entire magnetosphere, pairs born near tubes in the region of closed field lines will enter the region of the opposite magnetic pole. We might expect that they would heat a spot near this pole, but this heating was found to be negligible, because pairs produced beyond the tube have a fairly small Lorentz factor (about 40), and

do not experience acceleration along their trajectory. In this case, the beams of electron–positron plasma that are generated penetrate the stationary plasma of the Goldreich–Julian magnetosphere, which is composed of electrons and positively charged particles (probably, positrons), and is characterized by ρ_{eff}. This should lead to the excitation of plasma oscillations both in the moving electron–positron plasma and in the stationary plasma, and, consequently, to the generation of radio emission. The corresponding radiation has two components: one represents a narrow beam, while the other is isotropic. The isotropic radio emission should have a lower characteristic frequency.

Let us determine which gamma rays can leave a tube through the lateral surface towards the region of the Goldreich–Julian plasma. With this aim in view, let us consider the variation of the line curvature with height.

In the model formulated above, we have the following expressions for the magnetic field [9, 14]:

$$B_r = \frac{B_0}{\eta^3}, \quad B_\theta = \frac{B_0}{2\eta^3}\left[\theta + 2\nu\left(\frac{\Delta\eta}{\eta - 1 + \Delta}\right)^3\right],$$

where $\nu = B_1/B_0$. It can easily be shown that the radius of curvature of the field lines $\mathbf{B}$ can be expressed in terms of the function $f = B_r/B_\theta$ as

$$\rho = r\frac{(1 + f^2)^{3/2}}{1 + f^2 - \dfrac{df}{d\theta}}.$$

We obtain for a dipolar field $\rho_{dip} = \dfrac{4}{3}\dfrac{r}{\theta}$.

For a nondipolar field of the kind specified above, the curvature at $1 < \eta < 2$ is

$$\rho = \frac{2r}{3\nu}\left(\frac{\eta - 1 + \Delta}{\Delta\eta}\right)^3.$$

The following radii of curvature are obtained in this model: $\rho = 1.1 \times 10^6$ cm at $\eta = 1$, $\rho = 10.4 \times 10^6$ cm at $\eta = 1.2$, and $\rho = 10^8$ cm at $\eta = 2$. Therefore, the characteristic path of a photon leaving the tube can be estimated as $L > 2.5 \times 10^5$ cm.

For a gamma ray to leave the tube, it must not have a very large energy; i.e., it must be emitted by an electron in the initial stage of its acceleration. The energy of the gamma ray should satisfy the following inequality (for this estimation, we shall use here the path length obtained for the case of constant curvature):

$$S_{ph} = \frac{5 \times 10^{12}\rho_6}{B_{12}\varpi\hbar} > L = 2.5 \times 10^5.$$

We find from this expression

$$\varpi\hbar < \frac{2 \times 10^7}{B_{12}} \text{ eV},$$

where $\rho_6 = \rho/10^6$.

Photons produced by the resonant inverse Compton effect will satisfy this inequality if

$$\frac{B_{12}^3}{T_5} < \rho_6 \approx 10.$$

In this case, the resonant photons will produce electron–positron pairs in the region of closed field lines.

Let us calculate the death line of a radio pulsar for the case of magnetic curvature radiation. The free path of a photon is

$$S_{ph} = \frac{2 \times 10^{23} \rho_6 \rho_6'}{B_{12}' \gamma^3}$$

(primed and unprimed quantities refer to the points where the pair and gamma ray are produced, respectively).

The potential in a bent tube essentially reaches its maximum at a height of about $\eta = 1.2$. Therefore, we take $\rho_6 = 10$, which corresponds to a height of $\eta = 1.2$ and $\rho_6' = 50$.

Although the condition for pair formation $S_{ph} = 10^6 \eta/2$ was obtained for the case of constant curvature of the tube, we shall use this condition to estimate the death line for the case when the curvature changes with height.

This yields the death line $P = 0.7 B_{12}^{2/3}$. If gamma rays from the tail of the spectrum ($E = 10 E_0$) are taken into account, $P = B_{12}^{2/3}$. If the stationary plasma is taken into account, $P = 0.5 B_{12}^{2/3}$.

The death line for the inverse Compton effect is determined in a similar way:

$$\frac{5 \times 10^{12} \rho_6'}{B_{12}' mc^2 \gamma} = \frac{\eta}{2} 10^6,$$

and from this expression we obtain

$$P = 32 B_{12}. \tag{11}$$

If we include the effect of filling of the unfavorable field lines with plasma, then

$$P = 18 B_{12}. \tag{12}$$

The death lines for an asymmetric magnetic field with a favorable configuration are drawn in Fig. 4.

In the case under consideration, the death line extends far to the right. When the tube axis is bent unfavorably, the potential will decrease, and the death line will be shifted to the left compared to the dipolar
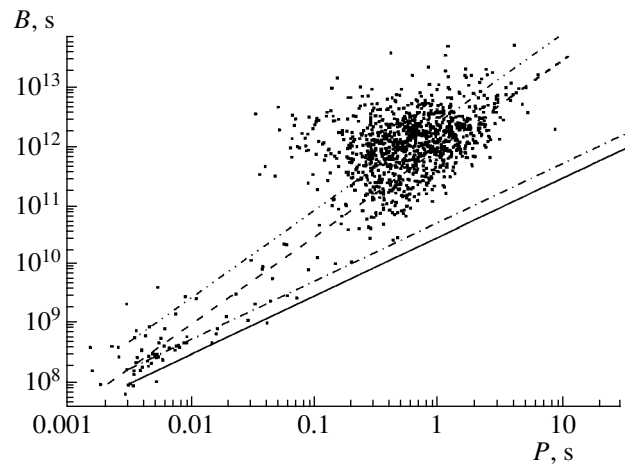
Fig. 4. Same as in Fig. 2 for the magnetic curvature mechanism (dashed), the inverse Compton effect acting on thermal photons from the entire stellar surface with stationary plasma (dash–dot), the inverse Compton effect acting on thermal photons from the entire stellar surface without stationary plasma (solid), and the magnetic curvature mechanism with stationary plasma (dash–double-dot).

case. In addition, it is possible that the run of the potential is such that the tube is filled with stationary plasma in the entire tube cross-section up to some height. In other words, the nondipolar magnetic field can also result in an earlier death of the radio pulsar.

Therefore, a nondipolar magnetic field in radio pulsars can lead to either an increase or decrease in the death periods.

6. RESULTS

We have obtained the death lines for the cases of dipolar and asymmetric magnetic fields, and estimated the multiplication factors for the secondary plasma in the case of a dipolar field.

If we assume that the pulsar radio emission is generated at the local frequency of Langmuir oscillations in the secondary-plasma beam, this frequency can be estimated as

$$\varpi = 1.4 \times 10^{10} \sqrt{k\gamma \frac{B_{12}}{P\eta^3}} \text{ rad/s},$$

where γ is the Lorentz factor of the secondary plasma and η is the normalized distance from the star to the spot where the oscillations are excited. This frequency turns out to be in the observable range for the multiplication factors obtained here.

If the field is dipolar and gamma rays are produced by the inverse Compton effect, the multiplication factor increases near the death line; i.e., the generation

of secondary plasma becomes more efficient. As a result, more efficient radio emission by pulsars should be expected near the death line. In the case of an asymmetric magnetic field, the generation of radio emission is possible beyond the tube of open field lines.

ACKNOWLEDGMENTS

REFERENCES

1. M. A. Ruderman and P. G. Sutherland, Astrophys. J. **196**, 51 (1975).
2. R. N. Manchester and J. H. Taylor, *Pulsars* (Freeman, San Francisco, 1977; Mir, Moscow, 1980).
3. A. G. Muslimov and A. K. Harding, Astrophys. J. **568**, 862 (2002).
4. A. I. Tsygan and Kh. Spruit, Pis'ma Astron. Zh. **21**, 877 (1995) [Astron. Lett. **21**, 790 (1995)].
5. A. N. Muslimov and A. I. Tsygan, Astron. Zh. **67**, 263 (1990) [Sov. Astron. **34**, 133 (1990)].
6. A. G. Muslimov and A. I. Tsygan, Mon. Not. R. Astron. Soc. **255**, 61 (1992).
7. V. S. Beskin, Pis'ma Astron. Zh. **16**, 665 (1990) [Sov. Astron. Lett. **16**, 286 (1990)].
8. A. I. Tsygan, *Pulsar Astronomy—2000 and Beyond*, Ed. by M. Kramer, N. Wex, and R. Wielebinski, ASP Conf. Ser. **202**, 473 (2000).
9. E. M. Kantor and A. I. Tsygan, Astron. Zh. **80**, 665 (2003) [Astron. Rep. **47**, 613 (2003)].
10. T. Erber, Rev. Mod. Phys. **38**, 626 (1966).
11. A. E. Shabat and V. V. Usov, Astrophys. Space Sci. **128**, 377 (1986).
12. N. S. Kardashev, I. G. Mitrofanov, and I. D. Novikov, Astron. Zh. **61**, 1113 (1984) [Sov. Astron. **28**, 651 (1984)].
13. E. Tademaru, Astrophys. J. **183**, 625 (1973).
14. V. D. Pal'shin and A. I. Tsygan, Preprint No. 1718 (Ioffe Phys.-Tech. Inst., 1998).
15. J. Arons and E. T. Scharlemann, Astrophys. J. **231**, 854 (1979).

Translated by Yu. Dumin

Relationship between Impulsive and Post-Eruptive Processes in Solar X-Ray Flares

M. A. Livshits and O. G. Badalyan

Institute of Terrestrial Magnetism, the Ionosphere, and Radio Wave Propagation,
Troitsk, Moscow oblast, 142190 Russia
Received May 4, 2004; in final form, June 15, 2004

Abstract—Powerful solar flares contain one or more impulsive events, plasma ejection, and the subsequent development of gigant post-eruptive loops. In the middle of the 1980s, Jakimiec proposed an analysis of the flare loops based on $\log T - 1/2 \log EM$ diagrams constructed from the observed soft X-rays (the so-called Jakimiec model). We have used this method to construct and analyze these diagrams not for various arbitrary events, but instead for similar flares within a single center of activity; in other words, for homological flares (two-ribbon flares observed in November 2000, powerful prolonged events observed in October-November 2003, etc.). This eliminated the effect of differences in the magnetic configurations, enabling us to find a new relationship: the slope ($\tan \alpha$) of the $\log T - 1/2 \log EM$ line during the flare decay depends on the maximum temperature $T_{\max}$ at the source of the soft X-rays. The dependence of $\tan \alpha$ on $T_{\max}$ gradually evolves from a series of short flares to a series of powerful, prolonged, nonstationary processes. Our results support the idea that the development of post-eruptive loops depends on the energy of the impulsive events for the phenomenon as a whole. Explosive evaporation simultaneously increases both the temperature and the density of the plasma at the loop top. The subsequent evolution of the post-eruptive formations depends on the difference in the initial conditions and on the degree of opening of the magnetic configuration. The importance of our analysis for the duration of flares and differences between dimmings is briefly discussed. © *2004 MAIK "Nauka/Interperiodica".*

1. INTRODUCTION

The large number of extra-atmospheric observations of solar flares that are now available has led to certain new ideas about the behavior of the phenomenon as a whole. Most powerful events include impulses, plasma ejection—eruptions in the form of a surge or coronal mass ejection (CME)—and the subsequent formation of gigant coronal loops. The post-eruptive phase can include the formation of both ordinary coronal loops, with heights below 0.1 $R_\odot$, and gigant arches that slowly ascend and live for many hours.

Loops are the main structural elements of flares. The high-temperature loop plasma radiates soft X-rays. In modern images, especially those obtained with high temporal and spatial resolution using TRACE, we can clearly see the low loops of the impulsive phase and an envelope of higher loops. We cannot conclude directly whether the formation and behavior of high loops depend on the impulsive process based on EUV and soft X-ray images. This problem is of interest for general models of flares, and can be solved using various modern observations. However, the routine detection of X-ray fluxes in two spectral ranges regularly performed by the GOES

satellites since 1988 can be used for an initial study of this problem.

The work of Jakimiec *et al.* [1], who first investigated the logarithm of the temperature as a function of the logarithm of the emission measure ($\log T - 1/2 \log EM$), was very important for analyses of flare soft X-rays. Each point on this diagram corresponds to a single time, forming a characteristic hysteresis pattern describing the formation and behavior of coronal loops. Below, we shall call this dependence the T−EM diagram.

A large number of studies of solar and stellar flares have been devoted to developing the Jakimiec model (see [2−4] and references therein). Already in [2], use of the temperature−density diagram was proposed for a loop top for diagnostics of the physical parameters of the flare, primarily the flare heating strength and duration. When the heating is sufficiently strong, the flare loops exhibit a quasi-stationary behavior, with this regime being similar to those obtained in [5], which are usually realized at activity centers. On the other hand, a significant weakening of the heating sharply decreases the loop-top temperature, although this process obviously cannot affect the radiation immediately. The Palermo−Harvard gas-dynamical code has often been used for numerical simulations

of processes during the flare decay [6]. Modeling processes at the loop bases introduces major difficulties into such simulations, since the entry of plasma from the partially ionized chromosphere into the coronal portion of the loop depends on the emission from these dense layers. In addition, the results depend on the initial temperature and density distributions and the expansion of the loop with height, especially in the transition region, all of which are poorly known. Several years ago, a simpler (in comparison with the computations of Reale [4]) approach to the gas-dynamical modeling of flare decay was used in [7], with an accurate treatment of the evolution of a constant mass of gas, taking into account both the heating and dissipative factors.

It is evident that the behavior in the post-eruptive phase could depend on the specific properties of the magnetic configuration. For example, powerful flares are very infrequent near isolated sunspots or strictly within small active regions. These are fairly compact and radiate soft X-rays for no longer than one to two hours. On the other hand, post-eruptive phenomena and the formation of distinct sigmoid flares are more frequent for active regions located in the immediate vicinity of boundaries between opposite polarities of the large-scale field, or for active regions connected to a neighboring activity center by high bundles of magnetic field lines. Most powerful flares are of this type, and their total durations can reach many hours.

If analyses of T−EM diagrams for a variety of flares does not take into account the configuration of the magnetic field of the active region, they will not lead to any definite astrophysical conclusions. Therefore, this method has become much less common over the last ∼10 yrs. We have applied it in its standard form to an analysis of powerful flares [8]. Gradual changes in the form of the hysteresis from weak coronal phenomena to powerful prolonged flares have been revealed (see Fig. 6 in [8]). Nevertheless, the usual technique has not been successful in analyses of the relations between impulsive and post-eruptive phenomena.

The objective of the present work is to study the relations between the impulsive and post-eruptive flare phases. Section 2 analyzes T−EM diagrams for flares of a single type occurring at a single activity center. New relationships found in Section 3 are further used to develop a general model for flares. Our most important finding is an independent argument supporting the idea that it is mainly the impulsive process that determines the subsequent evolution of the flare as a whole; i.e., both the maximum temperature of the source of soft X-rays and the behavior of the post-eruptive loops at the onset of the decay phase.

2. TEMPERATURE−EMISSION MEASURE DIAGRAMS FOR SERIES OF HOMOLOGICAL FLARES

The main disadvantage of previous works applying the Jakimiec model was that they considered flare phenomena occurring in different groups and/or various types of phenomena. There have been a few attempts to divide such studies according to the forms of T−EM diagrams, but these have not been successful. To improve the method, we have formulated an approach based on analyzing flares occurring in a single magnetic configuration and of roughly a single type.

Right at the start of this work, we understood that we must consider the radiation of post-eruptive loops only for processes occurring within a single magnetic configuration. Moreover, the behavior of flares sometimes changes even within a series of phenomena occurring in a single magnetic configuration when they are affected by adjacent activity centers. Therefore, we tried to select series of homological flares for our analysis.

The current (23rd) solar-activity cycle exhibited only a few infrequent powerful flares up until the end of October 2003. Nevertheless, we examined the soft X-ray data for large sunspot groups passing over the solar disk starting from 1997. We selected intervals of 14 days containing five to six powerful flares, including some X flares with almost equal durations. We identified 20 such series. The second stage of our preliminary analysis was to select flares occurring in a single group that were sufficiently isolated from each other in time (in order to eliminate the effect of the background in the second GOES channel, at 0.5−4 Å). Finally, we performed our main analysis for flares of group NOAA 9236 at the end of November 2000. This represents a rare case of flares occurring near a single large sunspot. The main radiation of these compact flares occurred in the immediate vicinity of the sunspot. We also analyzed series of very powerful events in October and November 2003. We supplemented these data with those for short flares occurring in July 2002 and typical large flares occurring at the end of April and beginning of May 1998, including the sigmoid flare of April 29.

The compact sunspot group NOAA 9236 has been studied as a part of an international program. There was a high flare activity in this group on November 24−26, with five X flares and two M flares over these three days. These powerful flares occurred, on average, at intervals of 10 h, and had fairly short durations (1−2 h). Figure 1 presents the total X-ray flux of the Sun in the two GOES-8 channels, which shows the flare activity of this group. The numbers in this figure correspond to the numbers in the Table (see below) for
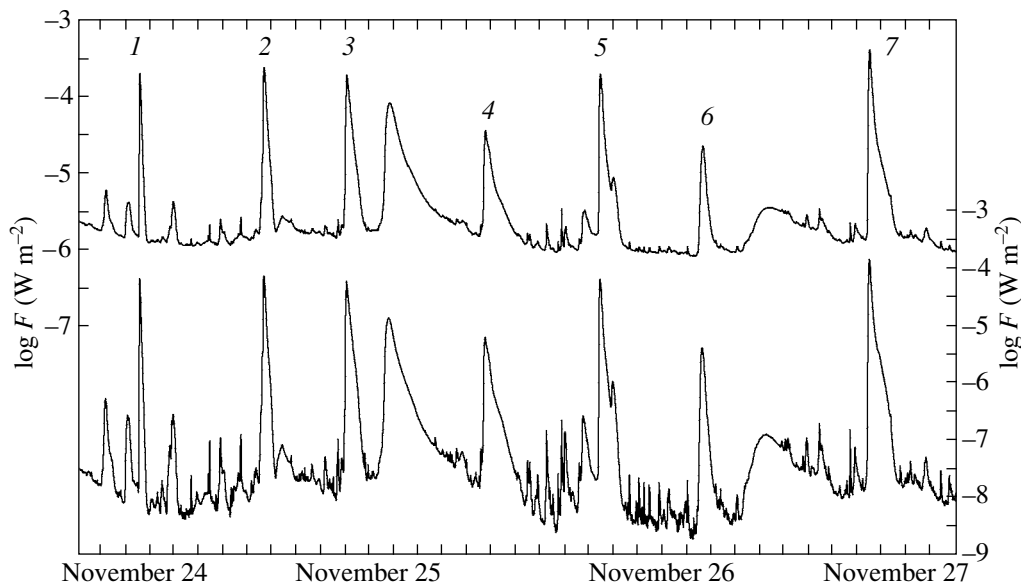
Fig. 1. GOES-8 X-ray fluxes for the end of November 2000. The upper and lower curves correspond to the ranges 1−8 Å and 0.5−4 Å, respectively. The numbers indicate the flares studied.

flares in group NOAA 9236 that were studied earlier in [9−11]. Note that the flare of November 24 (about 15 h) displayed an appreciable neutron flux [12].

The neutral line of the large-scale field in the vicinity of sunspot group NOAA 9236 was very irregular. The loops were connected to regions located near the main sunspot; that is, the loops did not reach heights exceeding the sunspot's size (1′ or 40 000 km). This was the origin of the short-duration flares in this group. Figure 2 shows two typical flares of this group. The Yohkoh difference image for the M flare (flare 4, Fig. 2a) shows that the flare loop connecting the main sunspot and emergent small hills of field of opposite polarity is still present in the middle of the decay phase. In other flares in this series, there were no high loops extending far from the sunspot. The main luminous portion to the south of the sunspot center was fairly small, and essentially did not propagate southward; i.e., the flare exhibited no sigmoid. Even powerful flares of this group displayed sigmoid sources only weakly. Namely, Figure 2b shows that the X-ray source at the very end of flare 3 is retained within the active region, and does not propagate along the neutral line of the large-scale magnetic field.

Another feature of this group, which contains a large central sunspot and numerous small formations, was that the small sunspots moved azimuthally about the large sunspot, from a certain point to the northwest (located outside but not far from the penumbra) to the opposite point. In other words, there were two gas-dynamical streams flowing around the penumbra with velocities of 150−300 m/s [13]. Series of such

powerful and also fairly short flares have occurred very seldom during the operation of modern space probes.

We discussed the time behavior of the temperatures of powerful flares in [8]. Upon reaching its maximum, the temperature decreases sharply over a characteristic time t_1 in the decay phase, and we can sometimes observe a subsequent transition (t_2) to a period of prolonged post-eruptive radiation (t_3). The giant arches formed in the powerful flares studied did not rise too high and were observed for only about an hour, in contrast to the behavior of typical prolonged, powerful flares.

Figure 3 presents the temperature behavior at the soft X-ray source for a weak and strong flare in this series. The parameters t_1, t_2, and t_3 are the reciprocals of the second terms of linear approximations for sub-intervals of the temperature function (Fig. 3a). For flare 4, $t_1 = 0.95$ h, $t_2 = 2.50$ h, and $t_3 = 5.75$ h. To some extent, the presence of three time intervals with ratios similar to these is typical for powerful, prolonged flares. It is possible that the post-eruptive prolonged X-ray radiation is associated with the high loop that is clearly visible in Fig. 2a. One characteristic of the powerful flares of this series was that a temperature plateau was observed instead of the period t_2. This is also visible in the T−EM diagrams for the final stages of large flares.

The main part of our study deals with T−EM diagrams (in the diagrams below, the temperature is in MK, the emission measure is in 10^{50} cm^{-3}). Figure 4 shows such diagrams for the studied flares of November 2000. These plots cover only time intervals
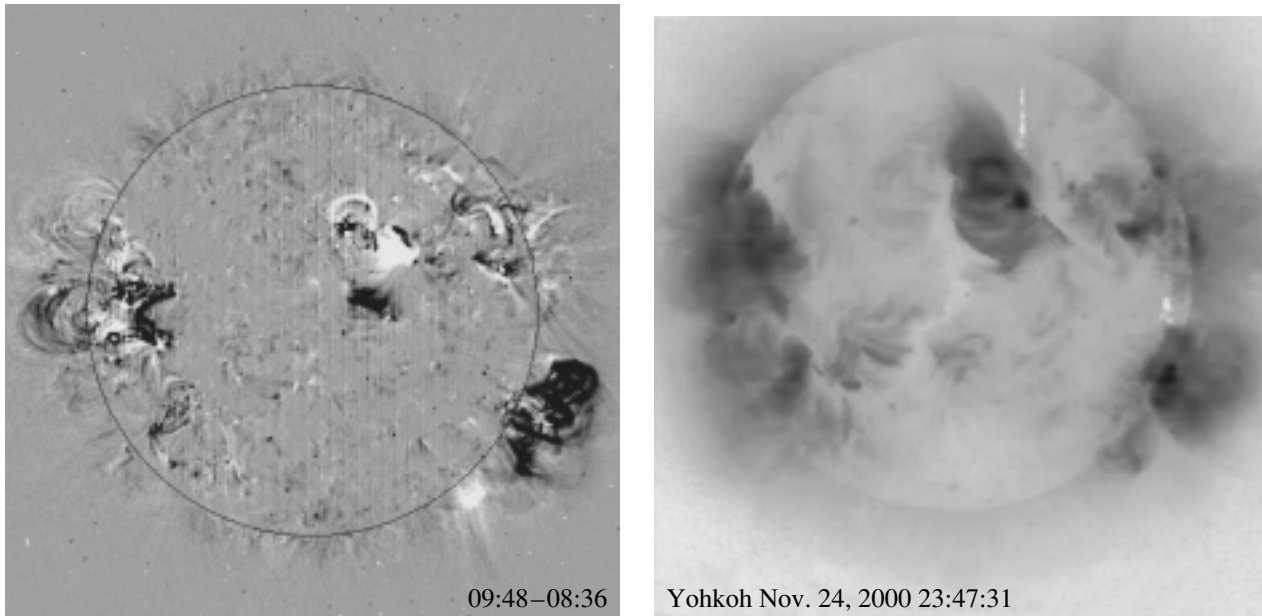
Fig. 2. Two examples of typical flares of group NOAA 9234. (a) The Yohkoh difference image of M flare 4 [11] shows that the flare loop connecting the main sunspot and emergent small hills of field of opposite polarity was still present in the middle of the decay phase. The main luminous portion to the south of the sunspot center was fairly small, and essentially did not propagate toward the south; i.e., the flare exhibited no sigmoid shape. Even powerful flares of this group have displayed sigmoid sources only weakly. (b) At the very end of flare 3, the X-ray source is still present in the active region, and does not propagate along the neutral line of the large-scale magnetic field.

in which the flare radiation appreciably exceeds the background; i.e., they do not show the very ends of the flares. The upper portions of the hysteresis curves include one or more impulsive energy releases. Figure 4 indicates some characteristic points on the hysteresis curves: the times when the maximum temperatures and emission measures of the soft X-ray source are achieved. In addition, the "break" of the hysteresis curve, when the flares enter a quiescent decay phase, is indicated for flares 1 and 5, as well as some typical times for the development of the post-eruptive arcade.

In contrast to the powerful prolonged flares studied in [8], the diagrams presented here were constructed for two-ribbon phenomena with total durations of one to three hours, including the time for the existence of the systems of gigant loops (the period t_3). All these flares, with the possible exception of the weak flares 6 and 4, appreciably occupied chromospheric layers, and the hysteresis extends to high T and EM (we discussed the form of the hysteresis in connection with Fig. 6 in [8]). In all these flares, the impulsive phase with its hard X-ray radiation [9] lasts several minutes. The maximum emission measure is reached near the maximum hard X-ray radiation recorded in the Yohkoh HXT M2 channel, and this time interval indicates the transition from the impulsive to the post-eruptive phase. In [8], this point was in the interval t_2 in the T−EM diagram, with t_2 for the most

powerful flares occurring after the maximum emission measure.

One peculiarity of the flares of November 2000 is the virtual absence of gigant arches. The diagrams in Fig. 4 indicate this via the sharp decrease in temperature observed after some time in the first three flares, accompanied by a constant emission measure. This effect is not so pronounced for the remaining flares, and the emission measure increases slightly toward the end of the flare. The short total duration of these events is associated with the same effect. It is clear that this is consistent with Fig. 2 and the weak sigmoid features of the flares considered.

3. NEW RELATIONSHIP FOR THE BEHAVIOR OF THE FLARE SOURCE OF SOFT X-RAYS

The development of flare loops corresponds to an approximately linear relation between the T and EM logarithms in the decay phase in the T−EM diagram. The Table presents the number of each flare, date, X-ray class, maximum temperature of the soft X-ray source, initial and final times limiting the approximated points for the lower hysteresis branch, and the tangent of the angle α between the approximating line and the horizontal axis. Note that, for the analyzed series of comparatively short two-ribbon flares occurring in 2000, the initial time is virtually always
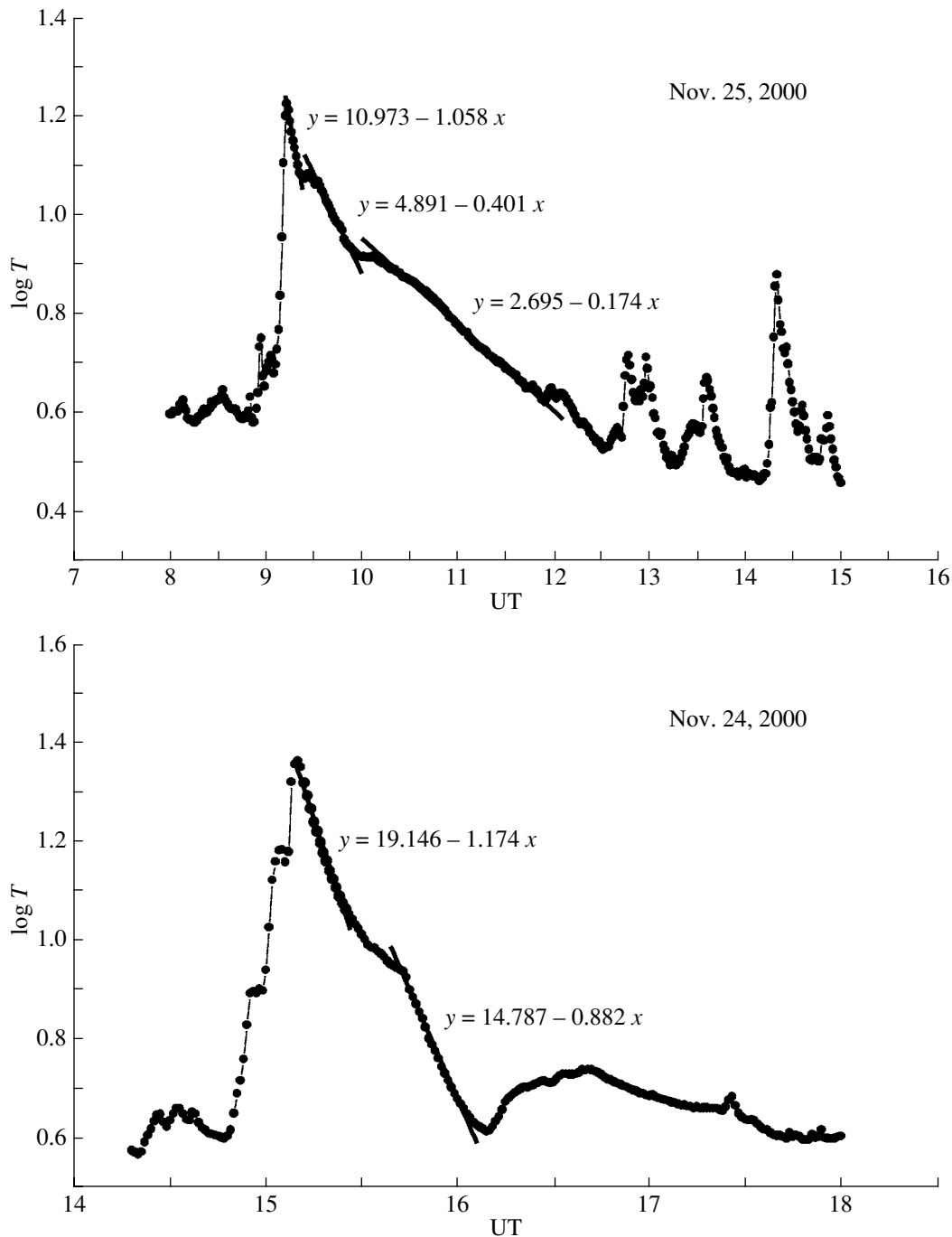
Fig. 3. Temperature of flares 4 and 2 as a function of time. Individual sections are approximated by straight line segments, $y = \log T$ (temperature in MK, time in hours).

very close to the EM maximum (except for flares 1 and 5). A comparison of Fig. 4 with the data in the Table supports this.

Figure 5 shows the portions of the T−EM diagrams selected for the time intervals indicated in the Table and the corresponding intervals for the approximating lines. The flares are ordered in accordance with the maximum temperature of their soft X-ray sources. We can see a certain relationship between the slope of the approximating line and the maximum temperature in Fig. 5. Its main feature is that the slopes $\tan \alpha = d \log T / d(1/2 \log \mathrm{EM})$ of the approximating lines for weak and strong flares in a single series of homological flares are appreciably different. For the strong flares 3, 5, and 7, there are intervals
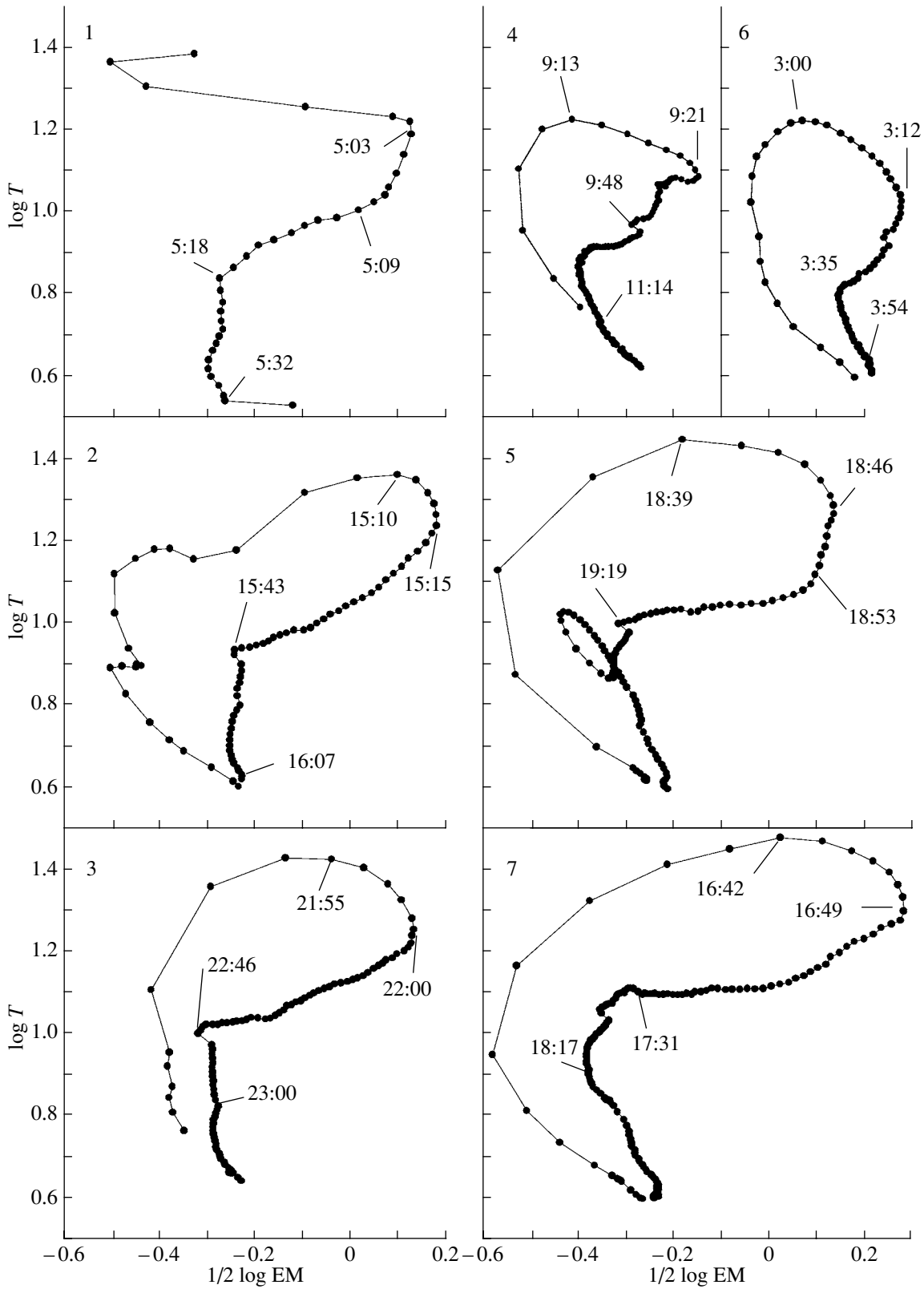
Fig. 4. $\log T - 1/2 \log \mathrm{EM}$ diagrams for seven flares indicated in Fig. 1 and here in the upper left corner. Time increases clockwise, and some characteristic times (UT) are indicated (see text).
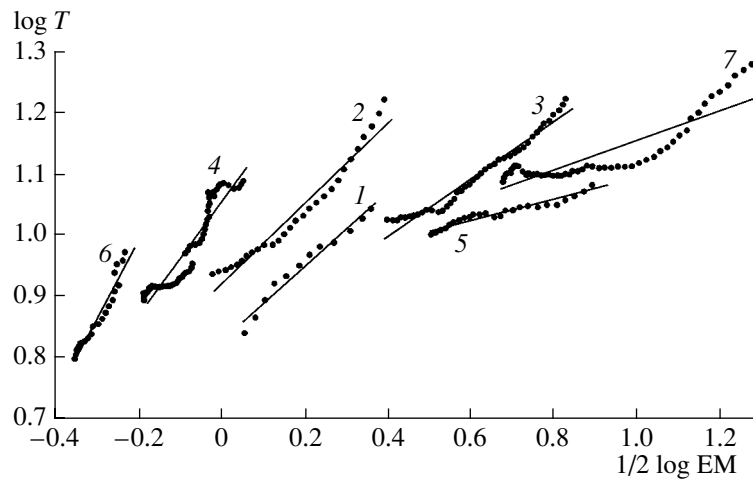
Fig. 5. Part of the T−EM diagrams for the decay phase for the same seven flares as in Fig. 4. The Table presents the beginnings and ends of the diagrams for each flare. We can see gradual changes in the slopes of approximating lines with increasing maximum temperature. For convenience, the curves for flares 4, 2, 1, 3, 5, and 7 are shifted along the horizontal axis relative to the curve for flare 6 by 0.2, 0.22, 0.27, 0.7, 0.82, and 1.0, respectively.

where the temperature decreases very slowly, so that the point in the diagram moves virtually parallel to the horizontal axis. Before any theoretical discussion, let us note that this corresponds to the quasi-stationary loops in the Jakimiec model [2, 3].

Analysis of the series of homological flares shows that the transition from large to small angles α (from weak to strong events) is gradual. Unfortunately, we do not have enough such series to statistically verify this conclusion. Nevertheless, this result may indicate that $\tan \alpha$ determines the main features of the behavior of the loop and the confined plasma. The relation between T and EM in the decay phase is determined by numerous parameters. Gradual changes in $\tan \alpha$ for the series of homological flares may indicate the dominant role of a single factor determining the macroscopic behavior of the post-eruptive loops.

The powerful flare 2 of this series displayed strong nonthermal processes and the generation of neutrons [12]. This could affect the subsequent behavior of the loops. Similar effects were more clearly manifest in the powerful flares of October–November 2003 considered below.

The low flare activity of nearly the entire 23rd solar-activity cycle was followed by high activity associated with the rise of group NOAA 10486 at the end of October 2003. This group gave rise to series of powerful events during successive solar rotations, with flares not being confined to this group even during the first rotation; namely, a flare in group NOAA 10486 induced an instability and extension of the process into group NOAA 10484.

We analyzed six flares occurring in October–November 2003 in the same way as the events of November 2000 described above. These include a flare near the eastern limb (October 23), two very powerful flares with some flux saturation in the hard GOES-10 channel (October 28 and November 4), X 10 and X 8.3 flares (October 29 and November 2, respectively), and, finally, a weak M 7.6 flare. The list indicates that this series contains more powerful events than those analyzed above. Though we tried to select homological flares solely in group NOAA 10486, the influence of the adjacent group and of the large-scale field probably affected these phenomena. For these reasons, we eliminated the two strong compact flares of October 23 (20 UT) and October 26 (7 UT) from our consideration (see also [14]).

The powerful homological flares of October–November 2003 were prolonged, and their rise phases each included several impulsive episodes. For example, the hard X-ray and microwave radiation of the October 23 flare contained two group of spikes, near 8:30 and 8:45 UT; in other words, the linear relation between $\log T$ and $\log EM$ in the decay phase begins when the impulsive energy release has already finished.

Figure 6 presents the diagrams for this series of flares. The maximum emission measures of the soft X-ray sources are higher than those in Fig. 4. The temperatures in Figs. 4 and 6, determined from the ratio of the signals in the two GOES channels, do not differ much. However, due to the very soft X-ray energies used, the real differences between the plasma temperatures in the loops for weak and strong flares are likely to be underestimated. If we adopt the Yohkoh HXT data on the thermal emission of flares occurring before February 2001, the temperatures of

Parameters of the flares and their analysis

Flare number	Date	Class	$\log T_{\max}$ (MK)	Approximation interval		$\tan\alpha$
				beginning (UT)	end (UT)	
1	24.11.00	X2.0	1.39	5:07	5:18	0.606
2	24.11.00	X2.3	1.36	15:16	15:43	0.652
3	24.11.00	X1.8	1.43	22:02	22:43	0.468
4	25.11.00	M3.5	1.22	9:21	10:17	0.923
5	25.11.00	X1.9	1.45	18:54	19:19	0.176
6	26.11.00	M2.2	1.22	3:16	3:35	1.274
7	26.11.00	X4.0	1.47	16:50	17:41	0.241
8	23.10.03	X5.4	1.43	8:42	9:47	0.635
9	24.10.03	M7.6	1.27	3:01	4:20	0.720
10	28.10.03	X > 17	1.6	11:16	13:13	0.404
11	29.10.03	X10	1.43	20:56	21:49	0.477
12	2.11.03	X8.3	1.42	17:30	18:23	0.594
13	4.11.03	X > 17	1.55	19:59	23:59	0.569

powerful events increase by approximately a factor of 1.5. The maximum temperatures (and EM) of the most powerful flares of 2003 cannot be determined using the GOES-10 data due to flux saturation. We have estimated the maximum temperatures for the two most powerful flares both by extrapolating the GOES-10 data and by using the fluxes of thermal emission in harder channels. Note also that there were gigant loops associated with the 2003 flares. Figure 6 shows only part of the decay phase, and weak X-ray radiation continued long after the end time in Fig. 6 (in other words, t_3 was tens of hours).

The form of the hysteresis curves in Fig. 6 is usual for powerful flares, except for the weaker flare of October 24. Two sets of gigant loops rather than one frequently occur in the decay phase of these flares, affecting the lower part of the hysteresis curve. However, they do not strongly affect the approximating lines. The Table presents the beginnings and ends of the time intervals for the six 2003 flares, and each straight line approximates all points of the lower branch of the hysteresis curve for the corresponding interval.

We could, in principle, construct a diagram such as Fig. 5 for this series of flares. This would similarly show some gradual changes in $\tan\alpha$ from weak to strong events. We can see this by considering Fig. 6 together with the Table.

Figure 7 presents $\tan\alpha$ as a function of the maximum temperature of the source of soft X-rays for two series of flares. Figure 7a shows a line based on

data for seven flares occurring in November 2000. Analyzing the series of homological flares, we obtain a result that could not be predicted *a priori*: the behavior of post-eruptive loops depends on the maximum temperature reached in one or more impulsive energy releases.

It is important to verify that this new relationship is not valid only for the selected series of typical two-ribbon flares. Our analysis shows that it is probably manifested in other series of homological flares as well, especially those occurring within a single activity center. We can consider the series of flares occurring in October–November 2003 to be an extreme case, with the corresponding relationship shown in Fig. 7b. Despite the fact that we have only rough estimates for the maximum temperatures of the most powerful flares, the general weak dependence can be discerned.

We analyzed some other series of homological flares in a similar way. Let us summarize the results obtained. First, the hysteresis diagrams obtained for a series of very short flares on July 17–18, 2002 are typical for flares occupying chromospheric layers. The Hα observations of A.N. Shakhovskaya obtained at the Crimean Astrophysical Observatory show that the ejection during the X flare of July 18 (at about 8^h UT) seems to shorten the lifetimes of the flare loops. This effect is likely responsible for the short durations of both this flare and other events in this series. These flares display similar maximum temperatures, but different lower branches of their hysteresis
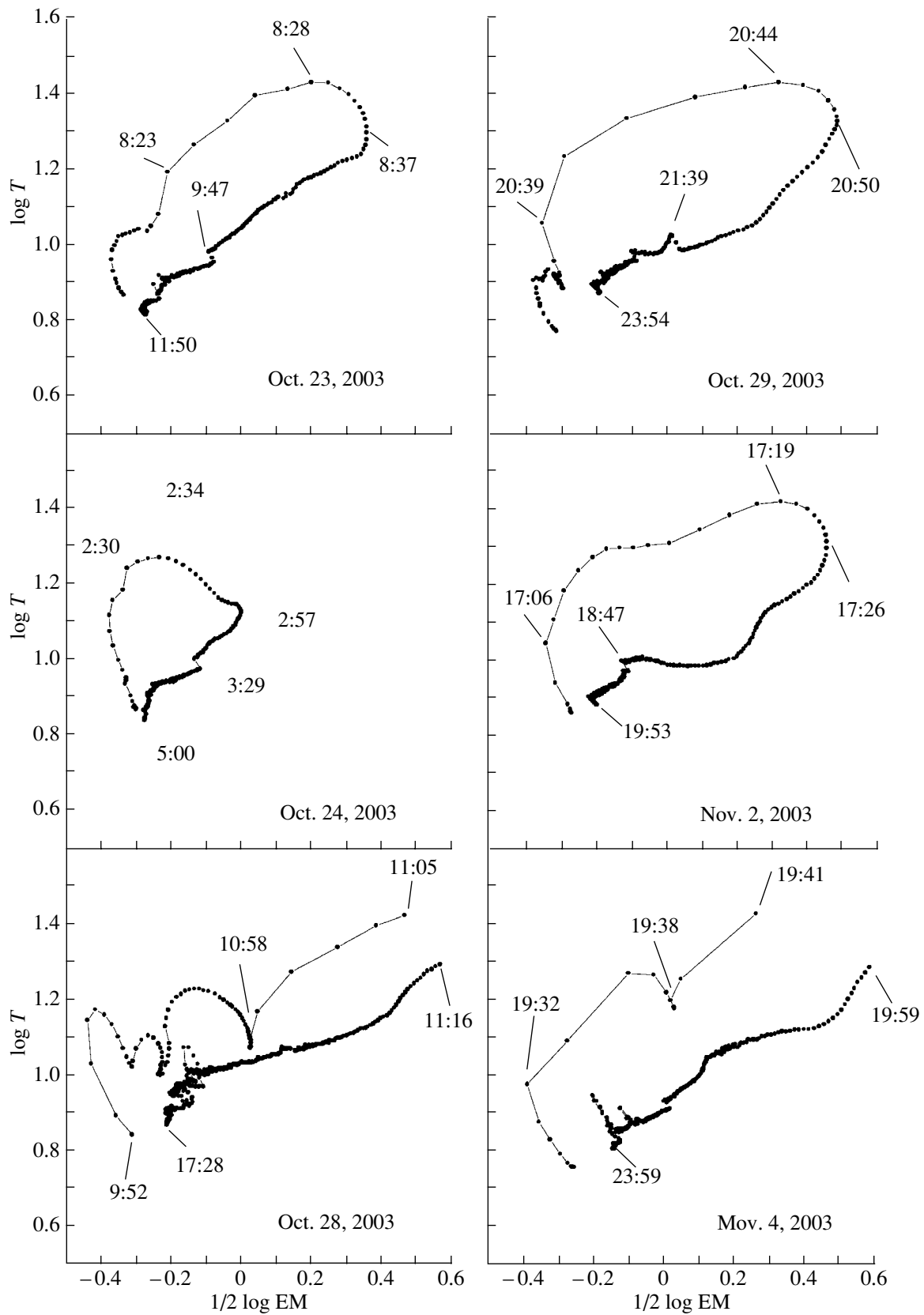
Fig. 6. $\log T - 1/2 \log EM$ diagrams for the flares of October–November 2003. The curves for the most powerful flares (two lower diagrams) are discontinuous at high temperatures due to saturation of the X-ray fluxes. The UT times are indicated.
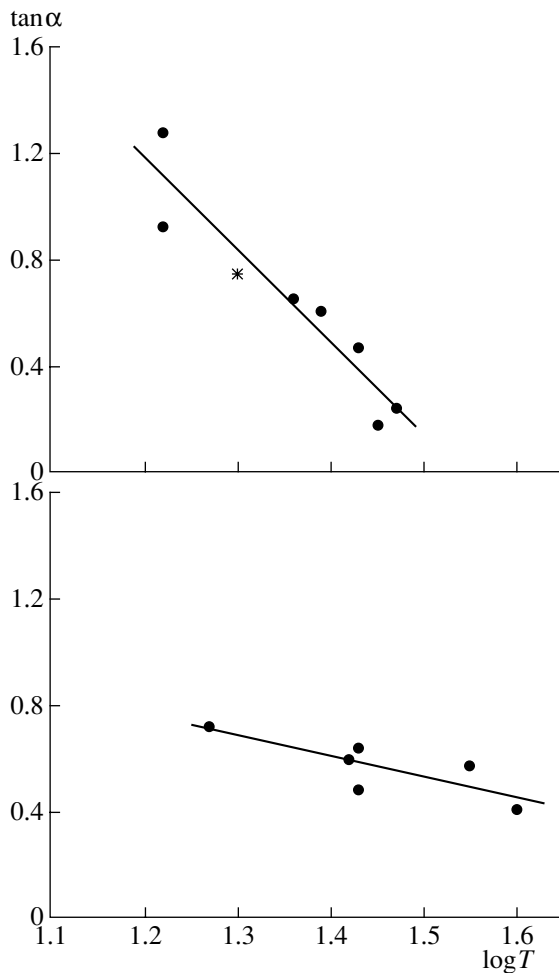
Fig. 7. Relation between the slope of the linear interval of the T−EM diagram during the decay phase and the maximum temperature (in MK) for (a) the flares of November 2000 and (b) the flares of October−November 2003. The line in the upper plot uses data for seven flares occurring in 2000; the asterisk indicates the flare of July 18, 2002.

curves. Therefore, the corresponding inclination angle in Fig. 7 becomes large. The asterisk in Fig. 7a shows one point corresponding to the distinct two-ribbon flare occurring on July 18 at about 8^h UT. The position of this point displays a typical $\tan \alpha$ value for fairly powerful two-ribbon flares.

We analyzed ordinary powerful flares with appreciable post-eruptive phases occurring at the end of April and beginning of May 1998, and these likewise demonstrate a relationship similar to that in Fig. 7. The slope here is intermediate between those shown in Figs. 7a and 7b. We note, however, that some sigmoid flares (such as that of April 29, 1998 [15]) fall away from the general relationship, and display low $\tan \alpha$ values for comparatively low maximum temperatures.

The gigant post-eruptive loops of sigmoid flares

frequently occur far from the first impulsive flare centers, and the relationship between impulsive and post-eruptive processes becomes disrupted. However, in most cases, the maximum temperature is reached precisely at the end of the impulsive energy release, when sufficient material is evaporated from chromospheric layers into the flare loops. The subsequent behavior of the flare depends largely on the processes occurring in the impulsive phase. These ideas provide a basis for interpreting the relationship we have found between the slope of the hysteresis curve in the decay phase and the maximum flare temperature.

4. PHYSICS OF THE RELATIONSHIP

The physical evolution of the plasma contained in gigant loops depends on numerous parameters. In this section, we address the question of whether there is some dominant process responsible for the relationship between $\tan \alpha$ and the maximum temperature.

It would be most natural to use numerical simulations for this purpose. Such an attempt was undertaken in [3], although, in our opinion, without any subsequent progress. A comparison of dozens of studies of the plasma dynamics in loops (see the review [4] on computations of stellar flares) with modeling of processes in a tube containing a constant mass of plasma [7] only demonstrate that prolonged radiation of soft X-rays requires prolonged heating, and the loop size corresponds to the heating applied.

Numerical computations have clarified the role of thermal conductivity as a dissipative process. In the nonstationary regime, thermal conductivity tends to equalize the plasma temperatures along the loop, but the downward energy flow due to thermal conductivity decreases after the maximum temperature (and maximum loop length) is reached, especially in comparison with radiative losses. Thermal conductivity supports the transport of energy and its efficient radiation at the loop bases. Therefore, we can disregard this dissipative process in the total energy balance of the loop as a whole (or of a set of loops) in a first approximation.

Let us try to understand what determines $\tan \alpha$ for a given flare. For this purpose, consider the energy balance in the flare loop using the results of [16]. A change in the energy of a unit mass of quasi-stationary plasma takes the form [17]

$$\frac{d\epsilon}{dt} = \frac{\eta}{\rho} - \frac{1}{\rho}n^2 L(T) - p\frac{d(1/\rho)}{dt}, \qquad (1)$$

where ϵ is the thermal energy per gram of material (erg/g), $\rho = Mn$ is the density (g/cm^3), $M \approx 2 \times$

10^{-24} g is the mean nuclear mass for the cosmic abundance of the elements given, p is the pressure, and η is the heating rate per unit volume (erg cm^{-3} s^{-1}). Note that the last term is the work of the gas under arbitrary changes in the physical conditions within a closed volume. The quasi-stationary regime allows volume changes but not any macroscopic plasma motions or siphon flows from one loop base to another.

The energy balance equation (1) is applied here to an optically thin plasma, and we can further simplify by neglecting the thermal conductivity. For a completely ionized plasma, $\epsilon = 3nkT/\rho = 3kT/M$ and $p = 2nkT$. Consequently, (1) takes the form

$$3k\frac{dT}{dt} = \frac{\eta}{n} - nL(T) + 2kT\frac{d\ln n}{dt}. \qquad (2)$$

Note that, when the source expands (the density decreases), the last term and the radiative-loss term are both negative. When the last term describing the energy changes associated with volume changes dominates in (2), the limiting solution can be found easily:

$$(T/T_0)^{3/2} = n/n_0. \qquad (3)$$

The solution (3) results from the monatomic gas behavior of the plasma, where the ratio of specific heats γ is 5/3. We assume here the absence of heating, dissipative terms, and special boundary conditions. Nevertheless, this limiting solution is always realized when the expansion of the emitting volume is significant and the term describing the expansion exceeds the term responsible for the radiative losses. In this case, with weak or no heating, the plasma can cool very rapidly; that is, faster than via radiation losses alone. Thus, we observe a rapid decay of soft X-rays at CME.

When both heating and expansion are absent, (2) describes radiative cooling on a characteristic time $t_{rad} = 3kT/nL(T)$. If we neglect the last term in (2) for a given lifetime of the source, multiply by Mn, and integrate over the plasma volume, we obtain

$$3kN\frac{dT}{dt} = \int \eta dV - L(T)\int n^2 dV. \qquad (4)$$

Here we assume that, at a given time, each volume element dV has the same temperature T and a total number of particles $N = \int n dV$.

Equation (4) shows that the changes in temperature are due to the difference between the heating and cooling in the emitting region. In order to delay a decrease in temperature, i.e., to increase the cooling time compared to t_{rad}, additional heating throughout the emitting region must compensate a considerable fraction of the radiative losses. We can explain this as follows. Let us introduce a quantity $u =$ $\eta/(n^2 L(T))$—the ratio of the additional heating to the radiative losses—and assume that u is independent of spatial position within the emitting volume. Equation (4) then reduces to

$$3kN\frac{dT}{dt} = -(1 - u)L(T)\text{EM}(T). \qquad (5)$$

If the density in the source is constant, this equation takes the form

$$\frac{d\ln T}{dt} = -\frac{1 - u}{t_{rad}}. \qquad (6)$$

In this simple case, the heating increases the characteristic radiation time by a factor of $1 - u$.

Let us then assume that the emission measure varies exponentially:

$$\frac{d\ln \text{EM}}{dt} = -\frac{1}{t_{em}}, \qquad (7)$$

where t_{em} is the characteristic time for an exponential decrease of the emission measure.

In this case, (6) and (7) yield a formula for $\tan\alpha$:

$$\frac{d\log T}{0.5 d\log \text{EM}} = \frac{2(1 - u)t_{em}}{t_{rad}}. \qquad (8)$$

Spectral observations enable us to determine the temperature and density in the post-eruptive loops. As a rule, the plasma temperature is higher for more powerful events, but the evaporation of material increases the density significantly. Therefore, the final t_{rad} does not differ much for different prolonged solar events, although it decreases somewhat with the overall power of the event. The behavior of t_{em} is mainly determined by the rate of expansion of the loop. Numerous TRACE films demonstrate a remarkable persistence of gigant arches over long time periods. This indicates a small range of t_{em} variations from case to case. For periods at the beginning of the decay phase of the November 2000 flares indicated in the Table, we find t_{em} varies from three to one hour from weak to powerful flares. Therefore, the ratio t_{em}/t_{rad} remains virtually constant for flares of this series. Thus, (8) indicates that the slope of the lower branch of the hysteresis curve is mainly determined by u: the relative heating of plasma in the upper portions of the loops.

This suggests the following scenario. A pulse of a certain power opens the coronal loops and, according to the Kopp–Pneuman model, results in energy release in the vertical current sheet that is formed. The total energy of the process is related to the power of this pulse, which, in turn, is related to the maximum temperature in the soft X-ray source at the end of the impulsive phase. In strong events with appreciable $T_{\max}$ values, this current sheet is large and well defined, and u approaches unity. For weak changes

in the characteristic time, $\tan\alpha$ becomes small, in accordance with (8). On the other hand, a weak pulse will usually give rise to a weak ejection, and reconnection in the vertical current sheet becomes inefficient. The increase in $\tan\alpha$ for this case is apparently related directly to the small value of u. It is most likely that this simple reasoning is applicable to a series of flares with various powers but of similar types occurring within a single magnetic configuration.

In this scenario, the difference between the slopes of the lines in Figs. 7a and 7b could be associated with different u approaching unity, which should be accompanied by a weakening of the dependence of $\tan\alpha$ on $T_{\max}$ for the powerful flares of October–November 2003.

5. DISCUSSION AND CONCLUSIONS

The T–EM diagram technique proposed by Jakimiec *et al.* [1] proves to be successful since these diagrams do indeed describe the thermodynamics of the plasma contained in the post-eruptive flare loops. A new element in our work is that we apply this method not to arbitrary events, but to similar events occurring in a single active region; in other words, to homological flares. This enables us to eliminate some factors that affect changes in $\log T$ and $\log EM$ similarly in the decay phase (in particular, those associated with the magnetic field configuration). This results in a new relationship, in which the changes depend on the maximum temperature in the soft X-ray source. Figure 7 shows that this dependence differs somewhat, at least for the compact flares of the end of November 2000 and the powerful events of October–November 2003. Adding several more flare series to these data (the very short event of July 2002, the sigmoid events and typical large flares of the end of April and beginning of May 1998) indicates that the approximately linear relation between $\tan\alpha$ and $T_{\max}$ remains valid for these series as well, but the slope gradually changes from the shortest to powerful, prolonged events.

Despite the large number of works on the Jakimiec model applied to solar and stellar flares, no relations between post-eruptive phenomena and high-energy processes in the initial impulsive stages of flares have been considered earlier. There is certainly a correlation between the maximum fluxes of hard and soft X-rays in a single event. Just this implies a possible relation between the corresponding stages of the flare. Our study provides evidence that the post-eruptive loops depend on the energy of impulsive episodes occurring throughout the event. Some general scenarios for powerful solar flares have been proposed recently. These include several energy releases at various points of the center of activity and subsequent

radiation by the gigant loops. The ejection of material in the form of either a low-temperature surge or a CME is a connecting link between these phases of the flare. Although the real timing of the CME (before, during, or after the flare) remains unknown, the Kopp–Pneuman model seems to be quite applicable. Under favorable conditions, a halo CME succeeding a rather powerful pulse could open the magnetic configuration in an extended region above the neutral line of the large-scale field. Subsequent reconnection in the vertical current sheet supports the prolonged heating and, consequently, the existence of gigant flare arches. In contrast, under unfavorable conditions, ejection can disrupt the processes supporting the coronal loops in two-ribbon flares, causing the gradual phase to become very short.

Note that the impulsive and post-eruptive phases become connected due to the large amount of plasma evaporated into the coronal portions of the flare loops. In the case of high energies, both the total amount of material and its temperature increase synchronously. In addition, the conditions for post-eruptive heating become more favorable. However, this relation may manifest itself differently at centers with different magnetic configurations. In certain cases, the ejections result in prolonged events, and in others, in series of very short flares. This makes the peculiarities of dimmings occurring during flares of various types of special interest. There can be both channelled dimmings (along the neutral line) and dimmings localized inside the activity center. These features have been brought into consideration in some the works of Chertok and Grechnev [11, 14], in particular, for the flares of November 2000 and of October–November 2003.

Some previous studies, such as the numerical simulations of Reale [4] and his colleagues, have indicated that the quasi-stationary regime is associated with plasma cooling due to radiative losses. This conclusion is supported by both the numerical simulations of [7] and our own analysis. The simple interpretation of our effect presented above shows that there is another important reason for the relation between T and EM in the flare decay, which is more important for the temporal behavior of the emission measure and is related to the loop geometry, which is first determined by the magnetic field. The net force of the pressure gradient, gravitation, and magnetic field frequently results in the loops maintaining a constant height for a long time, although the loops sometimes rise continuously, escaping into interplanetary space, or, on the contrary, become compressed. This second "geometric" reason helps us to understand the origin of the relationships observed for the lower branch of the hysteresis diagram.

If our proposed interpretation is correct, the power of the impulse exerts an indirect effect on the total duration of the X-ray flare, although this is mainly determined by the post-eruptive phase. The formation of post-eruptive arcades is sensitive to the specific properties of both the magnetic configuration and the impulse. Therefore, flares with similar energies can have significantly different durations. We can find very short X-ray flares, with durations of less than 10–20 min, when the ejection either destroys high flare loops or, in most cases, disrupts the processes necessary for the realization of two-ribbon flares. Typical compact (or two-ribbon) flares with durations of one to two hours occur within a single active region and support heating of the upper portions of the loops. Finally, flares displaying well defined post-eruptive phenomena involve the formation of gigant arches above large regions of the neutral line of the large-scale magnetic field. In this case, the reconnection of magnetic lines of force in the vertical magnetic field is most characteristic, and continues at higher and higher altitudes over many hours. As a rule, the height of the post-eruptive arches remains limited, even for rather powerful and long-duration flares; the escape of the loops into interplanetary space is rather rare. The relationship between the impulsive and prolonged phases of a flare that we have found, as well as the dependence of the duration on the properties of the magnetic configuration and ejection, should be taken into account in analyses of some space weather phenomena.

Examining the plasma thermodynamics in the flare loops, we must take into account the fact that the temperature used here is related to the sources of soft X-rays. This limits the temperature to the range relevant for the observed radiation. Moreover, we use here the approximation of a single temperature for simplicity. For the most powerful phenomena, for which the high-temperature contribution is significant, our approach underestimates the calculated quantities compared to the real plasma temperatures averaged over the source.

ACKNOWLEDGMENTS

REFERENCES

1. J. Jakimiec, J. Sylwester, B. Sylwester, *et al.*, Adv. Space Res. **6**, 237 (1986).
2. J. Jakimiec, J. Sylwester, B. Sylwester, *et al.*, Astron. Astrophys. **253**, 269 (1992).
3. B. Sylwester, J. Sylwester, S. Serio, *et al.*, Astron. Astrophys. **267**, 586 (1983).
4. F. Reale, *Stellar Coronae in the Chandra and XMM-Newton Era*, Ed. by F. Favata and J. Drake, ASP Conf. Ser. **277**, 103 (2002).
5. G. H. J. van den Oord and F. Zuccarello, in *Stellar Surface Structure*, Ed. by K. G. Strassmeier and J. L. Linsky (Kluwer, Dordrecht, 1996), p. 433.
6. R. M. Betta, G. Peres, F. Reale, and S. Serio, Astron. Astrophys., Suppl. Ser. **122**, 585 (1997).
7. K. V. Getman and M. A. Livshits, Astron. Zh. **77**, 295 (2000) [Astron. Rep. **44**, 255 (2000)].
8. M. A. Livshits, O. G. Badalyan, and A. V. Belov, Astron. Zh. **79**, 659 (2002) [Astron. Rep. **46**, 597 (2002)].
9. N. Nitta and H. S. Hudson, Geophys. Res. Lett. **28**, 3801 (2001).
10. V. N. Borovik, M. A. Livshits, I. Yu. Grigor'eva, *et al.*, in *Proceedings of a Conference of the CIS and Baltic Countries* (Nizhni Novgorod, 2003), p. 63 [in Russian].
11. I. M. Chertok, V. V. Grechnev, H. S. Hudson, and N. V. Nitta, J. Geophys. Res. **109** (A2), 1 (2004).
12. K. Watanabe, Y. Muraki, Y. Matsubara, *et al.*, Astrophys. J. **592**, 590 (2003).
13. T. T. Ishii, H. Kurokawa, and T. T. Takeuchi, in *Proceedings of the 8th IAU Asian-Pacific Meeting*, Ed. by S. Ikeuchi, J. Hearnshaw, and T. Hanava **2**, 431 (2002).
14. I. M. Chertok and V. V. Grechnev, Astron. Zh. **82** (2005, in press).
15. H. Wang, P. R. Good, C. Denker, *et al.*, Astrophys. J. **536**, 971 (2000).
16. M. Katsova, J. Drake, and M. A. Livshits, Astrophys. J. **510**, 986 (1999).
17. D. Mihalas, *Stellar Atmospheres* (Freeman, San Francisco, 1978), Vol. 2.

Translated by V. Badin

Some Results of 22-Year Monitoring (1982−2003) of Sagittarius B2 in the 1.35-cm Line

E. E. Lekht[1], O. Ramírez Hernández[2], and A. M. Tolmachev[3]

[1]*Instituto Nacional de Astrofísica, Óptica y Electrónica, Luis Enrique Erro No. 1, Apdo Postal 51 y 216, 72840 Tonantzintla, Puebla, México*

[2]*Sternberg Astronomical Institute, Universitetskiĭ pr. 13, Moscow, 119992 Russia*

[3]*Pushchino Radio Astronomy Observatory, Astro Space Center, Lebedev Physical Institute, Russian Academy of Sciences, Pushchino, Moscow oblast, 142290 Russia*

Received February 14, 2004; in final form, July 15, 2004

Abstract—A catalog of $\lambda = 1.35$ cm water-vapor maser spectra in Sgr B2 obtained in 1992−2003 is presented; this supplements our results for earlier observations in 1982−1992. Sgr B2 was monitored using the 22 m radio telescope of the Pushchino Radio Astronomy Observatory. The whole monitoring dataset for 1982−2003 has been analyzed. The emission received is a superposition of radiation from various parts of the entire Sgr B2 region, but the main contribution is made by two sources: Sgr B2(M) and Sgr B2(N). The monitoring did not reveal any long-term component of the integrated maser flux variations with a period shorter than 20 years. The flare component of the flux variability and a short-period component with a mean period of two years have been found. The latter are correlated with variations of the velocity centroid, supporting the reality of the short-period variations. It is likely that all the various types of variations are inherent to both Sgr B2(M) and Sgr B2(N), and represent a superposition of the variations occurring in each of these sources. There is an alternation of maxima of the emission from Sgr B2(M) and Sgr B2(N). © 2004 MAIK "Nauka/Interperiodica".

1. INTRODUCTION

The source Sagittarius B2 forms a composite region near the center of the Galaxy. All phenomena characteristic of active star-forming regions are observed there: very dense molecular material [1], complex molecules, ultracompact HII regions [2], hot cores [3], and H_2O, OH, H_2CO, CH_3OH, and SiO maser emission. There are two large centers of star formation (molecular-cloud cores): Sgr B2(M) and Sgr B2(N). Massive outflows are associated with these regions, which have been observed in lines of the NH_3 [4, 5], HC_3N [6], $C^{18}O$ [7], and CS [8] molecules.

The H_2O maser emission in Sgr B2 comes from four separate areas. Three are associated with Sgr B2(N), Sgr B2(M), and Sgr B2(S), while the fourth is between Sgr B2(N) and Sgr B2(M). According to Kobayashi *et al.* [9], these regions contain at least 39 maser spots. The strongest emission comes from two groups of maser spots: N and M. Lekht *et al.* [10] showed that, in 1984−1986, the emission from group N was more intense at radial velocities of 40−80 km/s. The source N is associated with a rotating accretion disk of molecular gas [11] in which three ultracompact HII regions are embedded [2]. The bipolar molecular outflow is aligned with the

disk rotation axis [4]. This outflow could be a source of maser excitation. A bipolar outflow was also observed in some molecular lines emitted in the main source Sgr B2(M), and SiO line emission is observed only in this source and not in Sgr B2(N) [12]. This suggests that a detectable amount of SiO has not yet formed in region N, indicating that this region is younger than region M [12].

We present here an analysis of our entire set of monitoring data for the H_2O maser source in Sgr B2 carried out in 1982−2003.

2. OBSERVATIONS AND DATA ANALYSIS

We have monitored the H_2O maser source in Sgr B2 ($\alpha_{1950} = 17^h44^m10^s$, $\delta_{1950} = -28°22'00''$) using the 22-m radio telescope of the Pushchino Radio Astronomy Observatory from 1982 until the present. The results of our first decade of observations (1982−1992) were published in [10]. We present here our analysis for the entire interval of our monitoring of Sgr B2.

We used a cooled FET 22-GHz amplifier for the 1992−2003 observations. Symmetrical beam switching was applied to lessen the effect of atmospheric radiation. The system noise temperature at low elevations was 150−250 K. The antenna beamwidth at
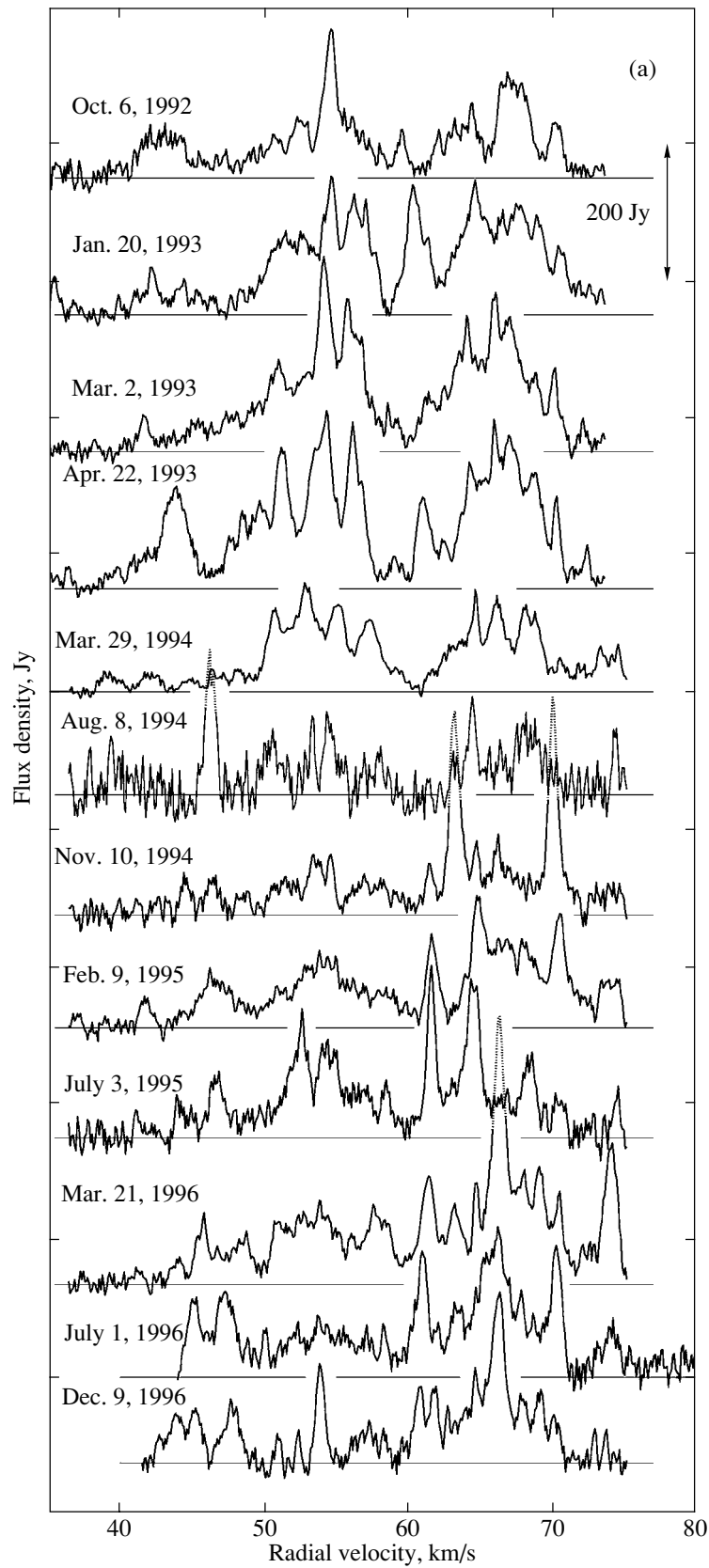
Fig. 1. Spectra of the H₂O maser emission of Sgr B2 obtained in 1992−2003. The vertical arrows show the scale in Jy; the horizontal axis plots the LSR velocity in km/s.

(b)

200 Jy

Jan. 21, 1997

Feb. 26, 1997

Apr. 1, 1997

May 7, 1997

June 5, 1997

Aug. 18, 1997

Sep. 15, 1997

Jan. 23, 1998

Mar. 25, 1998

June 2, 1998

Flux density, Jy

Radial velocity, km/s
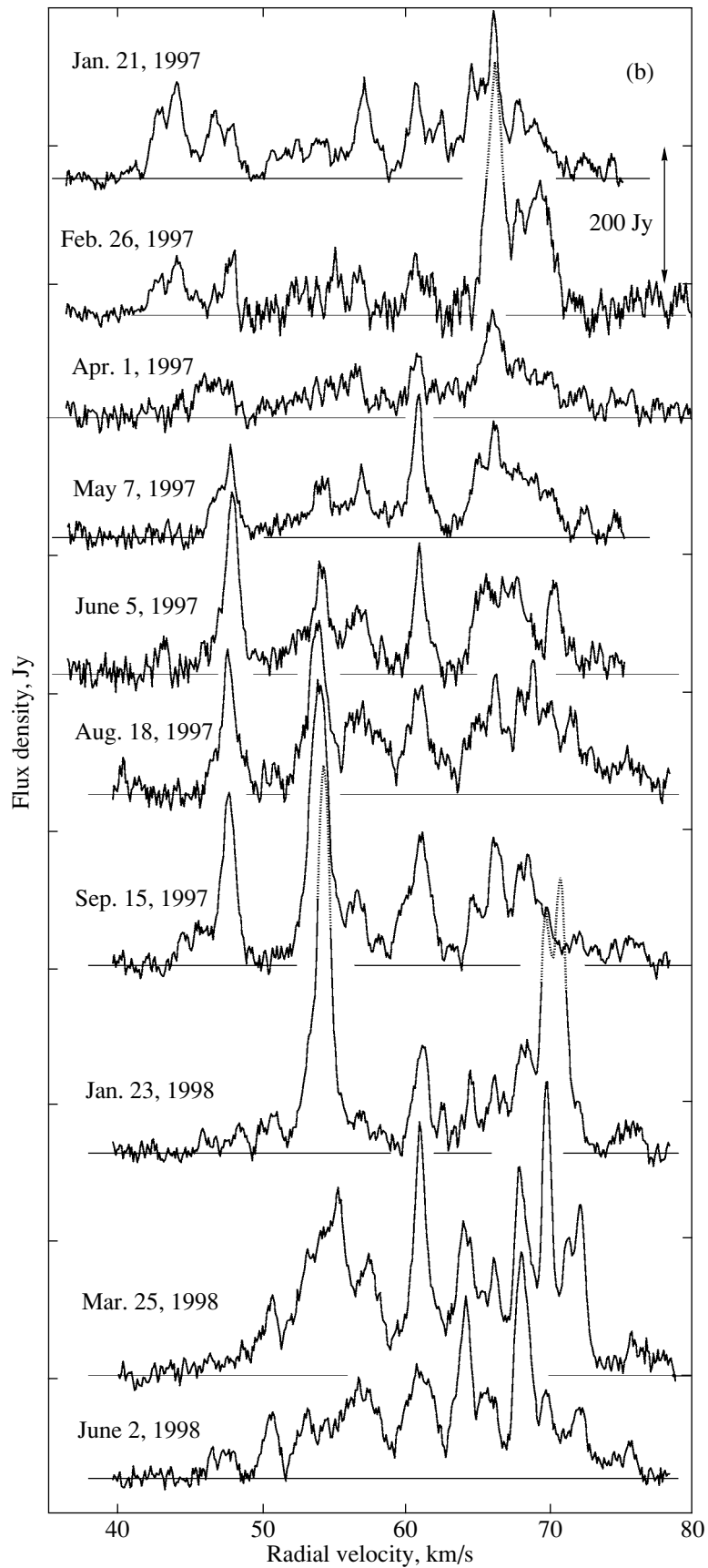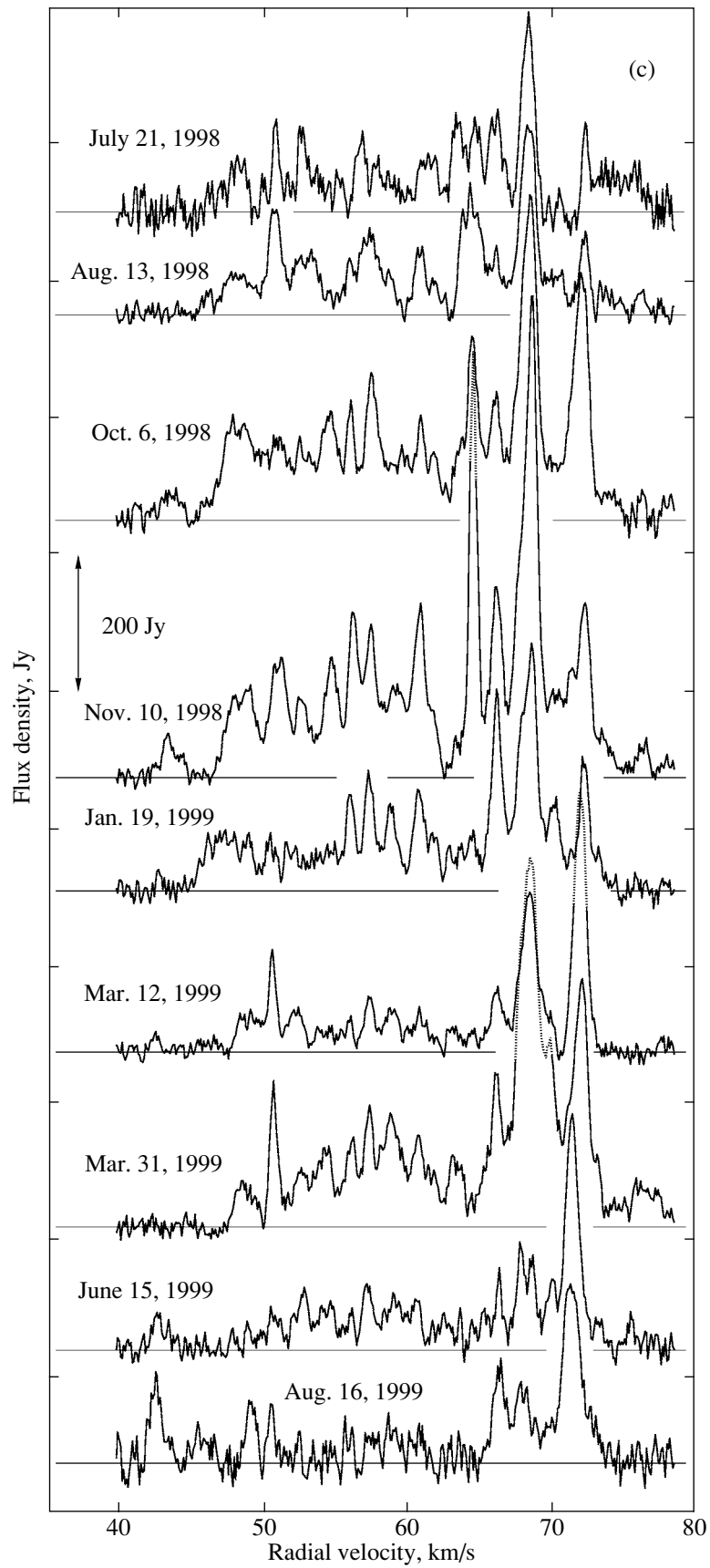
Fig. 1. (Contd.)
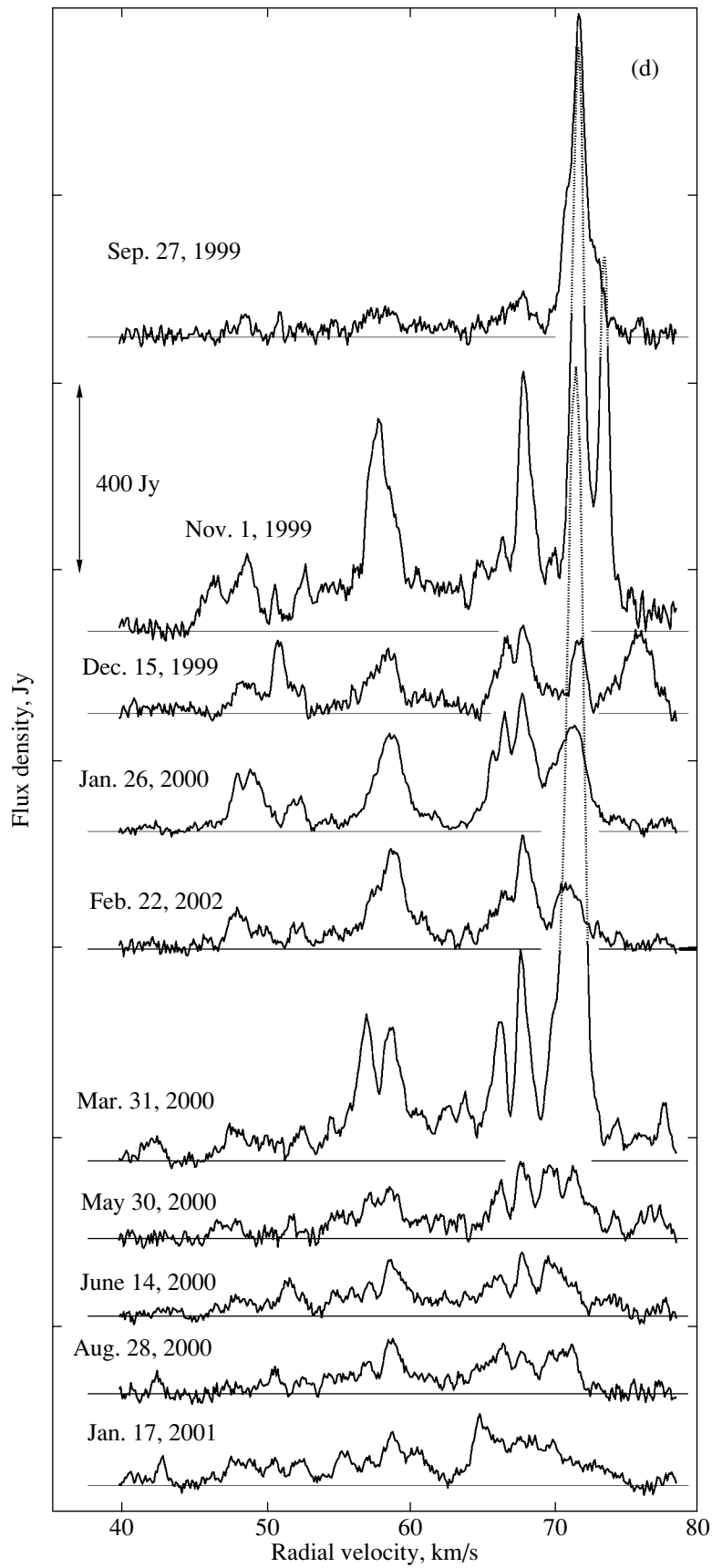
Fig. 1. (Contd.)
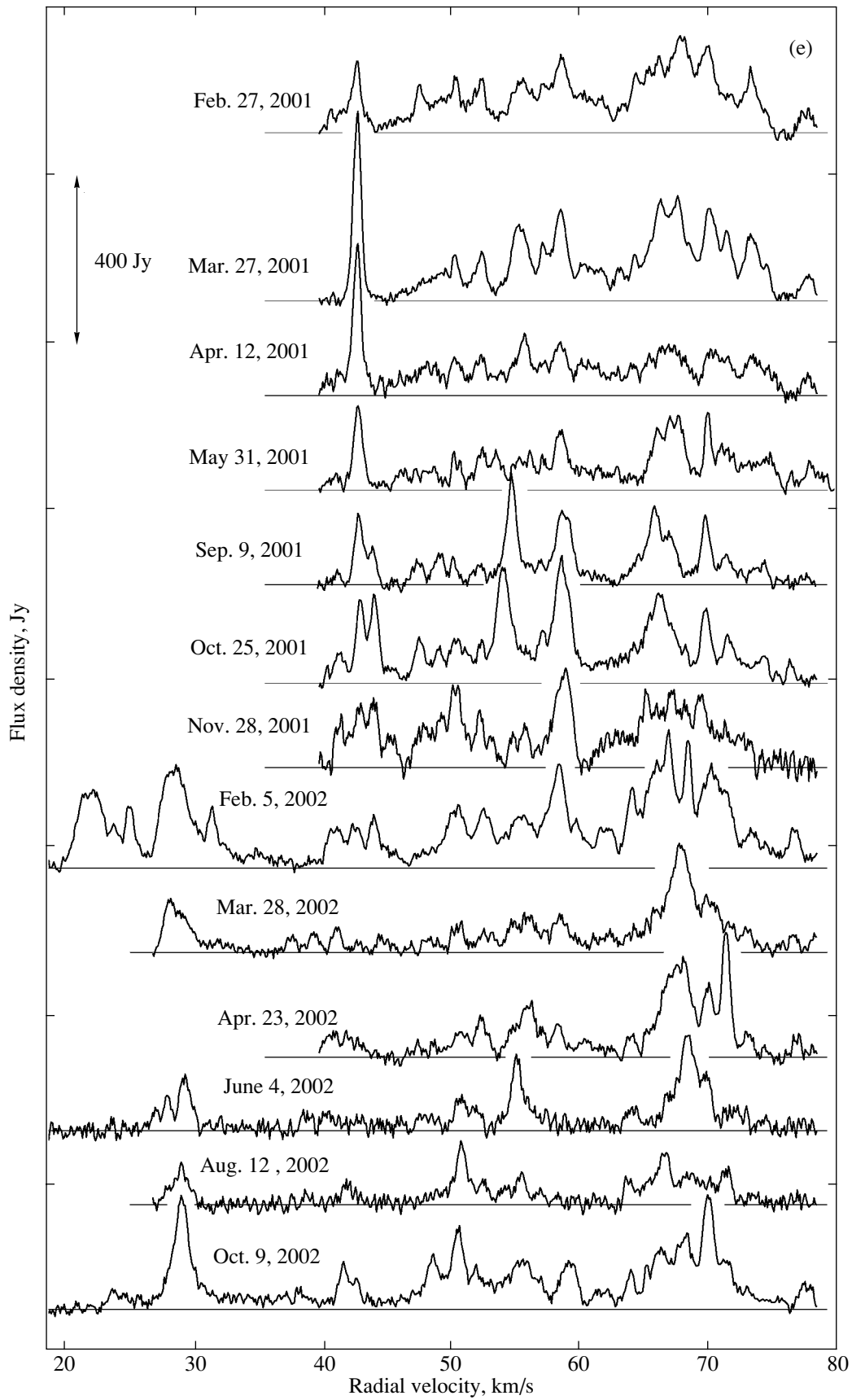
Fig. 1. (Contd.)
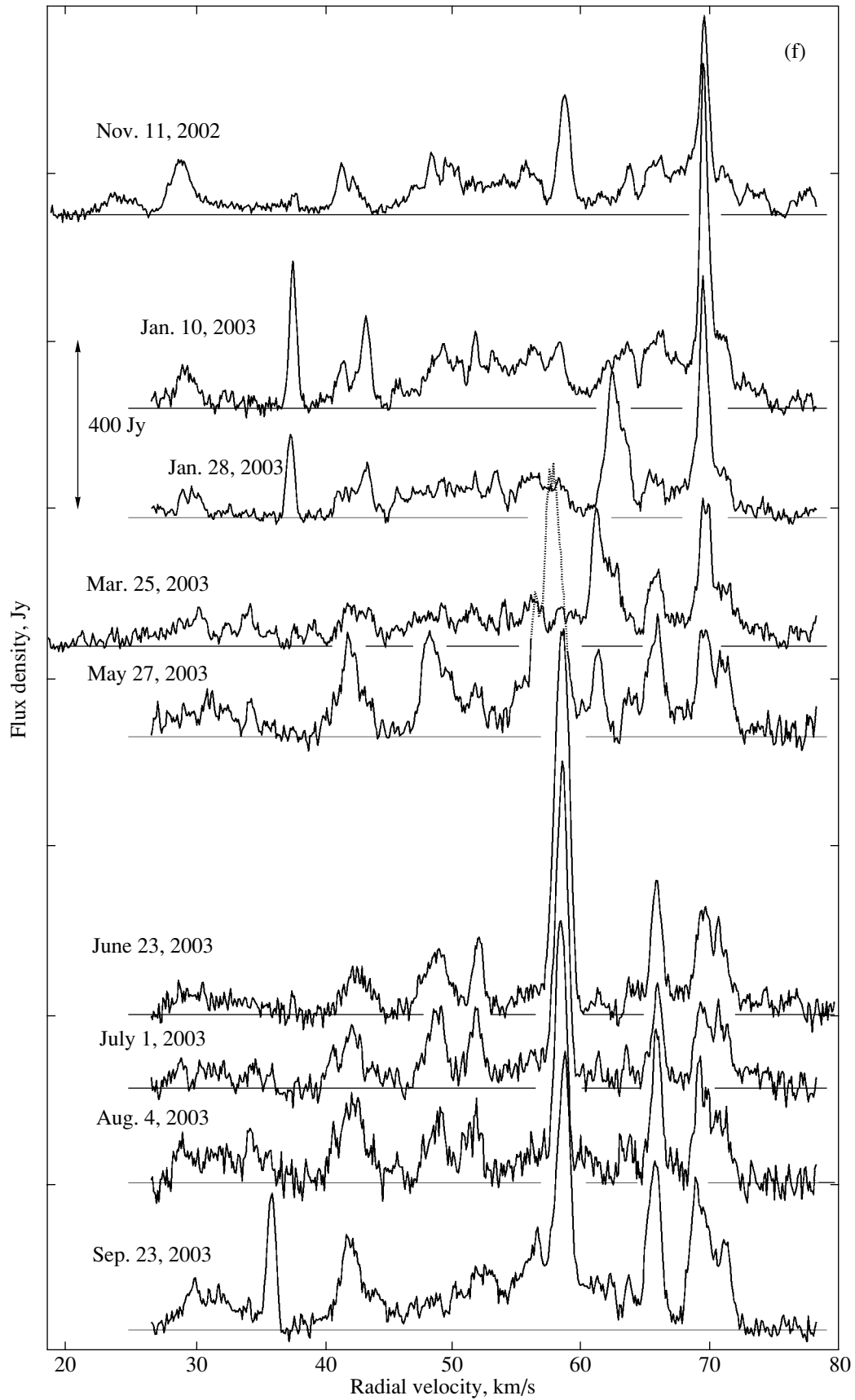
Fig. 1. (Contd.)

Fig. 1. (Contd.)
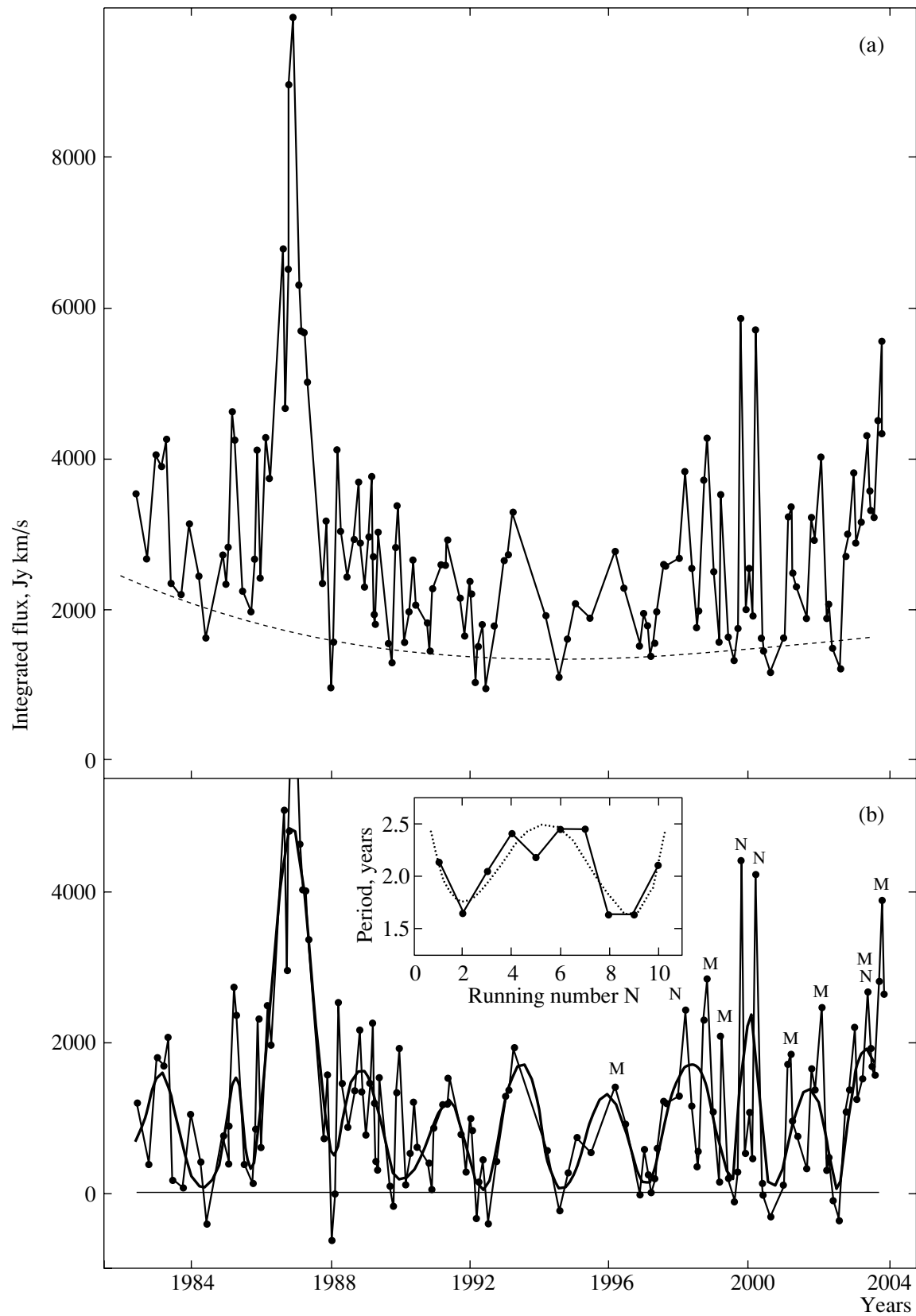
Fig. 2. (a) Variations of the integrated H$_2$O maser flux toward Sgr B2 at radial velocities of 40−80 km/s. (b) Same as (a) after subtraction of the component with a long variability time scale (dashed curve). The thick smooth curve represents the fast variability of the integrated flux. The insert shows changes of the period of this variability component.
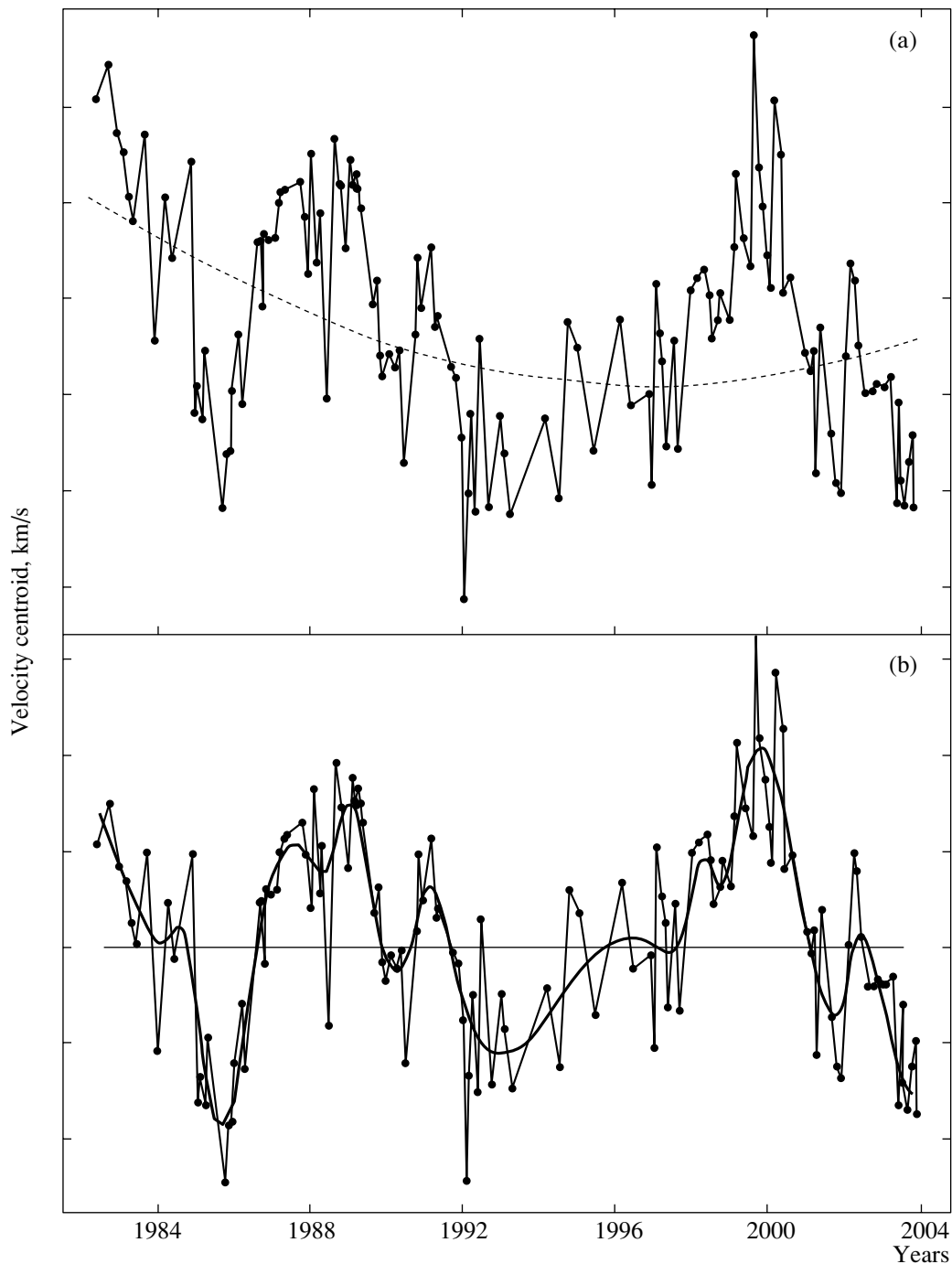
Fig. 3. Same as Fig. 2 for the velocity centroid (see text).

1.35 cm is 2.6′. For a pointlike source of unpolarized emission, an antenna temperature of 1 K corresponds to a flux density of 25 Jy. The signal analysis was performed using a 96-channel (128-channel since 1997) filter-bank spectrum analyzer with a resolution of 7.5 kHz (0.101 km/s at 1.35-cm).

Figure 1 shows the H_2O spectra of Sgr B2 corrected for absorption in the Earth's atmosphere. The horizontal axis plots the radial velocity with respect to the Local Standard of Rest and the vertical axis the flux density in Jy. In view of the large range covered by the signal, the figures are given on different scales. The vertical arrows show the scale intervals in Jy, and the horizontal lines trace the zero levels of the spectra.

We have obtained most of the H_2O spectra at velocities of $\approx 40-80$ km/s. Since the beginning of
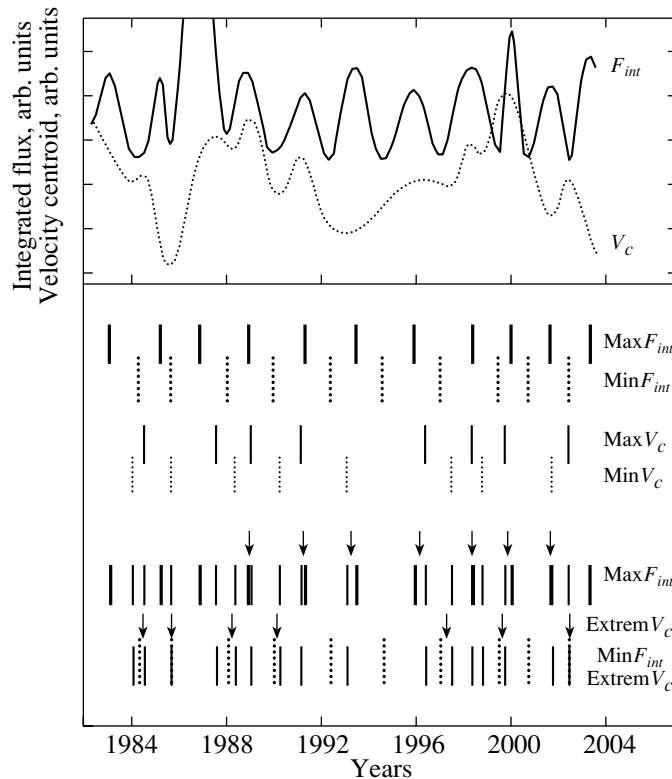
Fig. 4. Top: normalized curves showing the fast variability of the integrated flux F_{int} (solid) and of the velocity centroid V_c (dotted). Bottom: positions of the extrema of these curves (see text). The arrows mark flux extrema for which good correlations with velocity-centroid extrema are observed.

2002, the studied range was extended toward lower velocities, to $20-25$ km/s. We have observed a number of flares of individual components at velocities of $20-40$ km/s. The activity of the maser spots responsible for this emission decreased in 2003. According to the VLBI observations of Kobayashi *et al.* [9], the emission at $V_{LSR} < 40$ km/s comes primarily not from source N, but from other groups of maser spots. For this reason, we calculated the integrated flux and velocity centroid for velocities of $\approx 40-80$ km/s.

Figure 2a shows the variations of the integrated H_2O maser emission for the entire monitoring interval at velocities of $\approx 40-80$ km/s. The dashed curve is a fitted smooth curve describing the slow flux variations (the "base curve"). The curve obtained after subtracting the base curve is shown in Fig. 2b. Strong, short-lived flares of emission are observed. However, we were able to fit a component exhibiting quasiperiodic changes in the integrated flux with a mean separation between consecutive maxima (period) of two years. The maximum period is 2.45 years, and the minimum period 1.6 years. Each cycle of activity includes several (from one to three) bursts. The insert in Fig. 2b presents the time variations

of the period (the horizontal axis shows the running number of the "wave" corresponding to the quasiperiodic variations). The dashed curve is a fitted fourth-power polynomial. It is obvious that the variability of the periods is not random and displays a more or less regular character.

Figure 3a presents the variations of the velocity centroid, also for the entire monitoring interval. The dashed curve is a fitted second-power polynomial. The result of subtracting this polynomial from the velocity centroid curve is given in Fig. 3b. The thick curve is a fitted composite curve reflecting the fast variations of the centroid. As noted earlier in [10], we found no correlation between the long-term variations of the integrated flux and the velocity centroid in the monitoring data for 1982–1992. The entire monitoring data set (1982–2003) shows that the base curve of the integrated flux and the slow variations of the centroid have similar characters, displaying slow changes with a time scale considerably longer than our monitoring interval, i.e., >22 years.

To search for correlations between the fast flux variations with a mean period of two years and the velocity centroid, we normalized the flux and centroid variations. The variability of these parameters

of the H_2O maser emission after this normalization is shown in the top panel of Fig. 4. The vertical segments at the bottom of the figure show (from top to bottom): (1) the position of the flux maxima (solid) and minima (dotted), (2) the same for the velocity centroid, (3) a superposition of the flux maxima and centroid extrema (maxima and minima), and (4) the same for the flux minima. The arrows mark flux maxima and minima for which good correlations with extrema of the velocity centroid are observed. The differences in their positions do not exceed 0.2 periods of the short-period variations.

3. DISCUSSION

The second stage of the monitoring shows strong variability of the spectra, which always contain a large number of components (more than 30). The emission of the components virtually always overlaps at velocities of 45−75 km/s, forming a jagged total spectrum. However, emission features with high fluxes appeared quite frequently, whose fluxes, radial velocities, and linewidths we could estimate. Studies of the variability of the integrated flux and velocity centroid are of interest for such composite spectra.

Our results can be understood as a consequence of the fact that there are two main clusters of maser spots in Sgr B2: N and M, separated by only $45''$. With the beamwidth of the 22 m antenna ($2.6'$), we receive emission from N and M essentially as a single source. As we showed earlier [10], the very strong flare of 1986−1988 was probably associated with Sgr B2(N). This conclusion was based on the VLBI observations of Kobayashi *et al.* [9] in December 1985.

Another difficulty is that there were no interferometric observations of Sgr B2 in 1992−2003. In addition, our 1982−1992 observations revealed a strong radial-velocity drift for some emission features. This complicates an unambiguous identification of spectral components with the N and M sources based purely on the 1985 VLBI observations.

3.1. Main Results of the Monitoring

In spite of the difficulties noted above, we were able to derive some results on the variability of the emission as a whole, reflecting the total activity of the regions of maser emission; i.e., the two main groups of maser spots.

(1) We detected no slowly varying component of the integrated flux (at radial velocities of 40−80 km/s) with a period less than the duration of our monitoring interval, 22 years. There is only one fairly pronounced minimum in 1992−1994. If such long-term variability exists, its characteristic period will be considerably
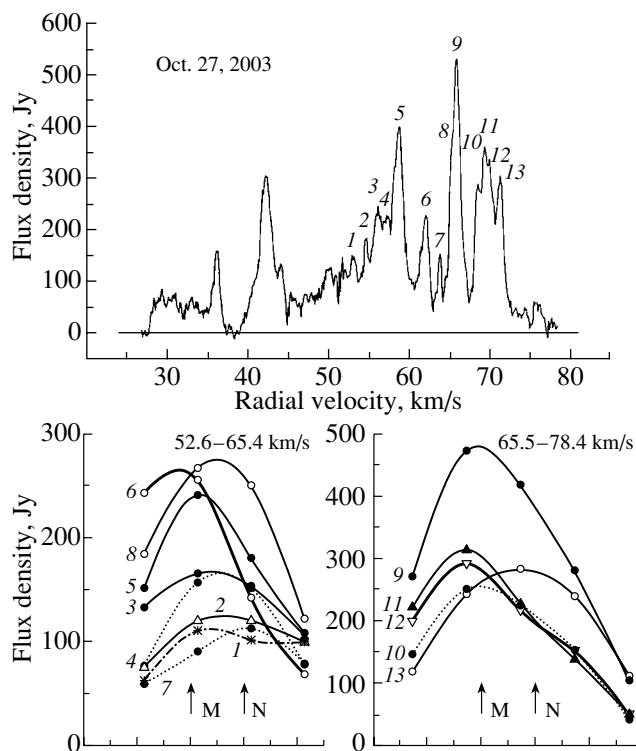
Fig. 5. Top: H_2O spectrum of Sgr B2 obtained on October 27, 2003. Bottom: flux variations for emission features 1−13 ($V_{LSR} = 52.6−78.4$ km/s) as a function of the antenna pointing relative to the main source M. The large bin corresponds to 45.

longer than 22 years (dashed curve in Fig. 2a, which is likely only a section of the complete variability curve).

(2) There are faster variations of the integrated flux with a mean period of approximately two years (thick curve in Fig. 2b). In turn, the period varies along the curve, which is fairly well approximated by a fourth-power polynomial (see the insert in Fig. 2b).

(3) As a rule, each two-year cycle consists of one to three short bursts of emission.

(4) The velocity-centroid variations have a composite character; like the integrated flux, these variations can be represented as a superposition of components with different variability time scales (Fig. 3).

(5) The variations of the integrated flux and velocity centroid are correlated (Fig. 4), supporting the reality of the detected two-year variations. This correlation is associated with both the appearance and disappearance of the emission of individual strong features or a group of features.

(6) The mean spectra for 1981−1992 and 1993−2003 are fairly similar.

3.2. Structure of the Sources Sgr B2(N) and Sgr B2(M)

Both of the main sources—M and N—are composite, in terms both of their structure and the most probable interpretation of the observed maser emission. The extent of the Sgr B2(N) region is $4'' \times 4''$, within which there are individual maser spots and groups of spots [9]. Some of these form an elongated structure $4'' \times 2''$ in size (0.2 pc $\times$ 0.1 pc for a distance to Sgr B2 of 10 kpc). This configuration is associated with a bipolar gaseous outflow from the accretion disk [4], which hosts the three ultracompact HII regions K1, K2, and K3 [2].

The most intense H_2O maser emission in Sgr B2(M) is associated with a compact group of maser spots, which are projected against the ultracompact HII region F. According to Kobayashi *et al.* [9], the maser spots occupy an area 0.04 pc $\times$ 0.04 pc in size (the distance to Sgr B2 adopted in [9] is 8.5 kpc). It is supposed that the HII region F is the center of activity of the OH, H_2CO, and H_2O masers. Later, Gaume *et al.* [2] showed that this region contains four subsources (F1—F4). The diameters of each are close to 0.01 pc, and their brightness temperatures are no lower than 23 400 K [13], whereas the standard temperatures of HII regions in the Galaxy are 6000—9000 K. The radial velocity found from the H66α hydrogen radio recombination line emitted by the source F as a whole is $\approx$70 km/s [13].

The strongest emission in the H_2O spectrum of Sgr B2(M) appeared at velocities of 60—70 km/s. This group of maser spots is located between the subsources F1—F4 [7]. Another difficulty with the model is that the Sgr B2(M) region contains a molecular outflow [6, 14], which is also associated with ultracompact HII regions and maser sources [9]. It cannot be excluded that the water vapor maser is not located at the edge of any part of the region F, but instead in the molecular outflow. Thus, the most intense H_2O sources in Sgr B2(N) and (M) are probably associated with molecular outflows. The difference between them consists in the sizes of the regions hosting the main groups of H_2O maser spots and in the temperatures of the HII regions K and F.

3.3. Identification of Spectral Components

To identify the strongest spectral components with the sources M and N, we carried out special observations at several points along the line connecting these sources on October 27, 29, and 30, 2003. This line is exactly aligned with the declination axis. The spacing between the points was equal to the projected distance between the sources M and N, $45''$. For 13 components at radial velocities of 52.6—78.4 km/s, we obtained flux curves for the various antenna pointings in declination relative to the main source Sgr B2(M) (Fig. 5). The numbers indicate the strongest emission components. The arrows on the lower graphs show the positions of the sources M and N.

The H_2O spectra of each of the sources are fairly complex, and contain emission features overlapping in velocity. For this reason, the maxima of the curves usually do not coincide with the directions toward M or N, but are instead somewhere between them. The position of the maximum is determined by the ratio of the emission from the two sources. We estimated qualitatively the contribution of each of the sources to the total spectrum. Some intense emission features in 1992—1998 fall in gaps in the spectrum for October 27, 2003. We were able to identify these in the spectra obtained by Kobayashi *et al.* [9].

We took the H_2O spectra for 1992—2003, which correspond to the maxima of the bursts, for identification. We then estimated the contribution of each of the sources to the integrated flux. The letters M and N in Fig. 2b denote bursts in which the emission of the corresponding source dominated. When the emission of both regions is comparable, both M and N are indicated (May 2003). We can see that the emission maxima for these sources alternate; this is important for our understanding of the integrated-flux and velocity-centroid variations and, especially, the component with the two-year period.

On December 4, 2003, we performed observations similar to Fig. 5 at velocities of 39.9—52.6 km/s. These observations show that this emission is associated with the northern source. According to Kobayashi *et al.* [9], most of the emission features belong to the group of maser spots "j," which is located to the southwest of Sgr B2(N).

3.4. Variability of the Emission Flux and Velocity Centroid

As we noted above, using the complete set of monitoring results (1981—2003), we can distinguish three variability components in the integrated flux. The fastest variations—bursts of emission—were observed throughout the monitoring interval, with the duration of a burst being approximately two to six months. The structure of the whole spectrum changed or was dominated by the emission of one or two features. The bursts of groups of maser spots associated with the sources M and N alternated. No correlation in the periodicity of this alternation was observed.

We believe the variations with a mean period of two years are real, since they are correlated with variations of the velocity centroid (Fig. 4). The spectra changed

strongly from period to period, resulting in variations of the velocity centroid. The periods of fast variability of the integrated flux are not constant, but these variations display a more or less regular character that is fairly well approximated by a fourth-power polynomial. It is difficult to explain this, since the observed emission is a superposition of the radiation from two comparable groups of maser spots.

We can also note a correlation between the flux and the velocity centroid associated with slow variations of the emission.

3.5. Mean Spectra

Since there was a minimum of the maser emission in 1992−1994, we plotted mean H_2O spectra for the time intervals before and after this minimum. The thick solid curve in Fig. 6 shows the mean spectrum for 1981−1992. The dashed curve shows segments of this spectrum from which two components of the strong flare of 1986−1987 (at 55.4 and 65.7 km/s) are eliminated. The thin curve represents the spectrum for 1993−2003.

We note the following facts.

—The H_2O spectra are superpositions of the emission from two more or less comparable sources (M and N).

—The structure of the spectrum undergoes strong time variations.

—Spatial displacements of the maser spots in source N have been detected [14].

—A radial-velocity drift of individual emission features has been observed [10].

In spite of the noted variations of the emission, the two mean spectra are quite similar in both amplitude and structure, which is especially important. The emission is present throughout the velocity range 45−73 km/s, but there is a large gap at 60.5 km/s during 1982−1992. Individual peaks present in both spectra were due to emission that was faint (for the Sgr B2 maser) but continuously present in the spectra for many years. Some peaks were associated with strong single or repeated bursts of emission. Flares occurred during the entire monitoring interval.

The observed drift of the components in space and in the H_2O spectrum could indicate the presence of a radial-velocity gradient in the masing region. A shock wave from a stellar wind or molecular outflow propagating in such a medium will consecutively excite regions with different radial velocities, giving rise to spatial and spectral drifts of maser spots.

Such structures have been detected, for example, as chains or filaments. The stellar wind from a central star or molecular outflow can also result in appreciable motion of a maser spot with some acceleration.
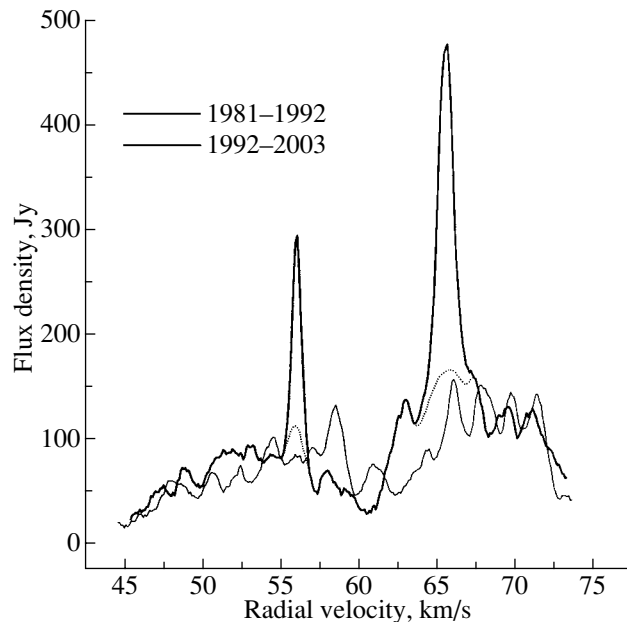
Fig. 6. Mean H_2O spectra of Sgr B2 calculated for the two time intervals 1981−1992 (thick curve) and 1993−2003 (thin curve).

As the effect of these factors subsides, the spot may be decelerated in the interstellar medium.

The recurrence of the mean H_2O spectra for various epochs suggests that the former effect is relevant for the two main groups of maser spots associated with Sgr B2(M) and Sgr B2(N), although the possible influence of the latter effect on the character of the spectral variability cannot be ruled out. The masing medium is strongly fragmented, and such fragments must be fairly stable.

Analysis of the variations of individual emission features for the entire interval of 1982−2003 could be important for refining models for the source. The results of such an analysis will be given in a separate paper. Approximately two−three times per year, we also included in our monitoring program observations at several points similar to those observed on October 29 and 30, 2003. This will enable us to derive spectra separately for Sgr B2(M) and Sgr B2(N), which is very important for interpreting the integrated flux variations.

4. CONCLUSION

To conclude, we summarize our results.

(1) We have presented a catalog of H_2O spectra for Sgr B2 obtained in 1992−2003.

(2) The results of our monitoring in 1982−2003 reveal slow changes of the integrated flux, which has a minimum in 1992−1994, and of the velocity centroid

(at radial velocities of 40−80 km/s). The 22-year observation interval proved to be too short to reveal any periodic character of this long-term variability.

(3) There is an alternation of the emission maxima for Sgr B2(M) and Sgr B2(N). No periodicities were found.

(4) We detected short-term variations of the integrated flux with a mean period of two years, which correlate with the velocity-centroid variations.

(5) All the detected types of variability are superpositions of variations in the emission from the two main groups of maser spots associated with Sgr B2(M) and Sgr B2(N).

REFERENCES

1. S. Hüttemeister, T. L. Wilson, C. Henkel, and R. Mauersberger, Astron. Astrophys. **276**, 445 (1993).

2. R. A. Gaume, M. J. Claussen, C. G. De Pree, *et al.*, Astrophys. J. **449**, 663 (1995).

3. P. de Vicente, J. Martin-Pintado, and T. L. Wilson, Astron. Astrophys. **320**, 957 (1997).

4. S. N. Vogel, R. Genzel, and P. Palmer, Astrophys. J. **316**, 243 (1987).

5. R. A. Gaume and M. J. Claussen, Astrophys. J. **351**, 538 (1990).

6. D. C. Lis and P. F. Goldsmith, Astrophys. J. **356**, 195 (1990).

7. Y. J. Kuan and L. E. Snyder, Astrophys. J. **470**, 981 (1996).

8. D. M. Mehringer, Astrophys. J. **454**, 782 (1995).

9. H. Kobayashi, M. Ishiguro, Y. Chikada, *et al.*, Publ. Astron. Soc. Jpn. **41**, 141 (1989).

10. E. E. Lekht, O. Ramires Hernandes, A. M. Tolmachev, and I. I. Berulis, Astron. Zh. **81**, 195 (2004) [Astron. Rep. **48**, 171 (2004)].

11. D. C. Lis and P. F. Goldsmith, Astrophys. J. **402**, 238 (1993).

12. S. Y. Liu, D. M. Mehringer, Y. Miao, and E. Snyder, Astrophys. J. **501**, 680 (1998).

13. C. G. De Pree, R. A. Gaume, W. M. Goss, and M. J. Claussen, Astrophys. J. **464**, 788 (1996).

14. M. J. Reid, M. H. Schneps, J. M. Moran, *et al.*, Astrophys. J. **330**, 809 (1988).

Translated by G. Rudnitskiĭ

Star Formation Region in Orion KL. Epoch 1985.8

V. A. Demichev and L. I. Matveenko

Space Research Institute, Russian Academy of Sciences, Moscow, Russia
Received February 4, 2004; in final form, July 15, 2004

Abstract—We have derived the fine structure of the region of the H_2O supermaser flare in the Orion Nebula at epoch 1985.8. This structure includes a chain of compact components that extends to 25 AU and has a width of 0.4 AU. The velocities of the components vary along the chain. The structure corresponds to an accretion disk separated into protoplanetary rings, viewed edge-on. The velocities of the components correspond to Keplerian motion around an object with a mass of $M = 0.3 \pm 0.2 M_\odot$. The velocity of the central object relative to the Local Standard of Rest is $V_{LSR} = 4.0 \pm 0.7$ km/s. The radius of the inner part of the disk is 9 ± 4 AU, while the radius of the outer disk is 35 ± 6 AU. The rotational velocities of the inner and outer rings are 5 ± 1 km/s and 2.5 ± 0.5 km/s, respectively. The emission of the structure is amplified in the ambient medium—an envelope with velocities of 7.6 ± 0.3 km/s. The rate at which the envelope is accreting onto the central object is 3.6 ± 0.7 km/s. The gradient of the infall velocity is 1.1 km/s. © 2004 MAIK "Nauka/Interperiodica".

1. INTRODUCTION

Galactic gas-dust complexes are unique cosmic laboratories where a a broad spectrum of physical conditions are realized. As a result of gravitational instability, active zones containing protostars are formed. Star formation is accompanied by powerful water maser emission at $\lambda = 1.35$ cm, which corresponds to the $6_{16}-5_{23}$ ($f_o = 22\,235.08$ MHz) rotational transition. This emission is a sensitive tracer of processes accompanying star formation, and provides opportunities for detailed structural studies using Very Long Baseline Interferometry (VLBI).

In the dense molecular cloud Orion KL, H_2O maser sources are concentrated in eight active zones with sizes reaching 2000 AU [1]. Occasionally, powerful flares of maser emission occur, whose nature and triggering mechanism are not completely clear. High activity in the Orion nebula was first observed in 1979−1987. The flux density of the maser emission at a velocity of ∼8 km/s reached 9 MJy [2] and was highly (∼60%) linearly polarized [3].

The maser flare was detected in its initial phase in September 1979 by the Simeiz−Pushchino interferometer [4]. The flux density of the flare reached 0.5 MJy, with most of the emission determined by a compact (0.25 AU) core located at the edge of an elongated (2.5 AU) component. Subsequent observations involving an increasing number of telescopes showed that the flare region has a more complex multi-component structure [5]. Therefore, observations are performed with an increasingly large number of radio telescops. In November 1985, observations were carried out by a global array, yielding very high angular resolution [6−8]. Four groups of components were discovered. Flare emission of $F = 2.6$ MJy was detected for two of these with $V \approx 8$ km/s. The processing of radio interferometric data requires powerful computers, which were not available in Russia in 1985. The currently available computers are sufficient for this task, and have enabled us to detect low-brightness structures and establish their connection with compact components. Below, we present the results of our study of the fine structure of the H_2O supermaser region in Orion KL at epoch 1985.8.

2. OBSERVATIONS OF THE H_2O FLARE IN Orion KL

Observations were carried out on November 2 and 3, 1985. The emission profile had a Gaussian shape with a low-velocity "tail." The maximum radio flux density reached 2.6 MJy at a velocity of 7.7 km/s, with a linewidth of $\Delta V = 0.6$ km/s (Fig. 1). Seven telescopes of the global array participated in the observations: Simeiz (22-m), Onsala (20-m), Effelsberg (100-m), Haystack (37-m), Green Bank (43-m), Socorro (VLA-14.25-m), and Owens Valley (40-m). The telescopes formed an array containing 21 baselines. The baseline ($u-v$) coverage is shown

Flux, 10^6 Jy
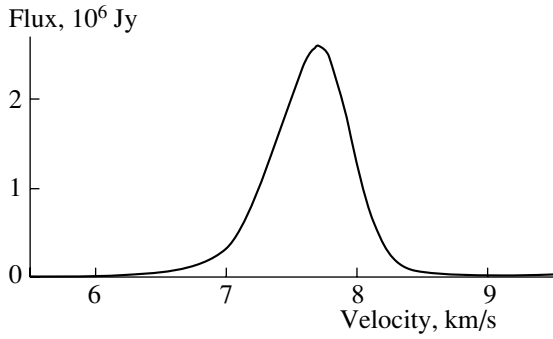
Fig. 1. Spectral profile of the H_2O supermaser emission in Orion KL at epoch 1985.8.

in Fig. 2. The maximum and minimum sizes of the interferometric fringes were $\varphi_{max} = 7$ mas and $\varphi_{min} = 0.3$ mas, enabling us to determine both the large-scale and small-scale structure of the object. The signals were recorded using the MK-II VLBI system, with a bandwidth of 500 kHz in the first experiment and 250 kHz in the second experiment. Hydrogen frequency standards were used to synchronize the local-oscillator frequencies. The observations were correlated at the Max Planck Institute for Radio Astronomy in Bonn (Germany) and the National Radio Astronomy Observatory in Socorro (New Mexico, USA). The frequency resolution was 5.2 and 2.6 kHz (or 0.07 and 0.035 km/s). The high signal-to-noise ratio made it possible to achieve very high angular resolution. In practice, the measurement errors were determined by the accuracy of the calibration. The amplitudes and phases of the correlated signals were calibrated using the continuum source 3C 84, and the self-calibration was done relative to the signal in the channel 51 ($V = 7.22$ km/s).

3. IMAGING WITH THE VLBI DATA

The response of a radio interferometer to a source with brightness distribution $T_b(x, y)$ is

$$R(u, v) \sim \iint T_b(x, y) \exp[-j2\pi(ux + vy)]dxdy,$$

where x, y are the relative coordinates of the source on the celestial sphere and u, v is the projected interferometer baseline in wavelengths.

The measured responses correspond to correlated fluxes and phases of spatial harmonics of the brightness distribution $T_b(x, y)$; i.e., to its Fourier transform. We restored the image using a version of the CLEAN algorithm developed by Högbom[9]. This algorithm represents a numerical inversion of the convolution of the true source brightness distribution with the synthesized beam:

$$T_{bc}(x, y) = T_b(x, y)^{**}D(x, y).$$

Here, $T_b(x, y)$ is the source brightness distribution and $T_{bc}(x, y)$ the computed brightness distribution obtained by taking the inverse Fourier transform of the interferometer responses $R(u, v)$ for each point of the map x_i, y_i:

$$T_{bc}(x_i, y_i) = \iint R(u, v) \exp[j2\pi(ux_i + vy_i)]dudv.$$

The synthesized beam is

$$D(x_i, y_i) = \iint \exp[j2\pi(ux + vy)]dudv.$$

The radio-brightness distribution is represented by a set of point sources. Their responses are replaced later by the response of a "clean" beam, which has no sidelobes.

Thus, the processing can be reduced to the following steps.

(1) The map $T_{bc}(x, y)$ is computed by taking the inverse Fourier transforms of the response $R(u, v)$ and the synthesized beam $D(x, y)$ (the response to a point source).

(2) The peak intensity in the map is found and the response to a point source is subtracted from that position. The maximum amplitude of the subtracted response is equal to the product of a coefficient γ (the loop gain) and the corresponding amplitude of that point in the map, $A = \gamma T_{bc}(x_{peak}, y_{peak})$. The resulting values of $A(x_{peak}, y_{peak})$ are stored as δ functions, and are used further to construct the clean map.

(3) This procedure is repeated until all significant elements of the source structure are removed from the map.

(4) The set of δ functions making up the model is convolved with the clean beam; i.e., each δ function is replaced by the clean-beam function with the appropriate amplitude. A Gaussian whose width is equal to the initial width of the synthesized (dirty) beam is usually adopted as the clean beam.

(5) The cleaning yields an intensity distribution made up of a set of δ functions whose amplitudes and positions correspond to the subtracted components. Subtracting a δ function is equivalent to subtracting a complex harmonic with maximum amplitude $R(\delta)$. The model response, $R(\text{mod})$, approaches the measured response, $R(u, v)$, as the number of components increases.

We separated the region under study into pixels with step 0.1 mas in x and 0.2 mas in y. We used a Gaussian with a full width at half-maximum of 0.5 mas as the "clean" beam. In this way, we obtained maps of the supermaser-emission brightness distribution in all channels with a velocity resolution of 0.07 km/s. As an example, we present in Fig. 3 the measured and model interferometer responses for
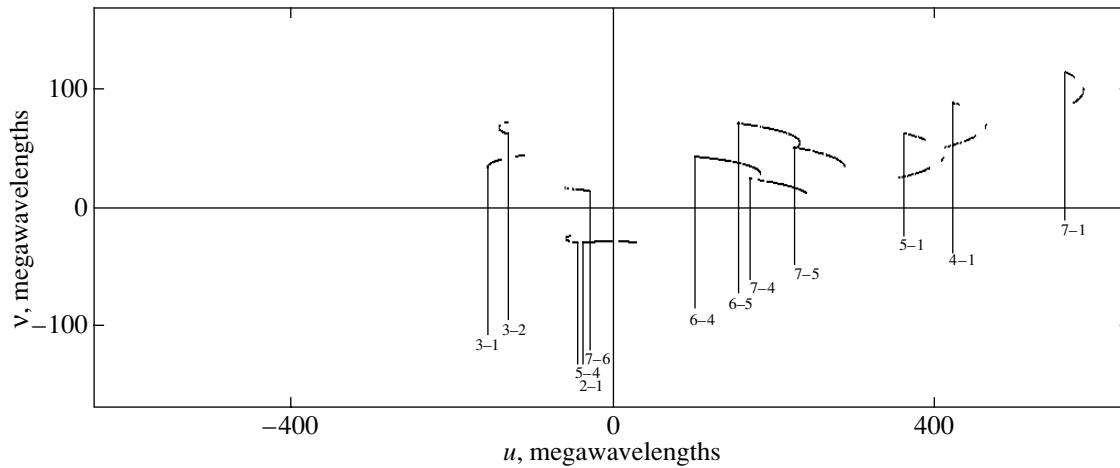
Fig. 2. Coverage of the $u-v$ plane for the global VLBI observations of Orion KL at 1.35 cm. The antennas involved were (1) Effelsberg, (2) Onsala, (3) Simeiz, (4) Green Bank, (5) Haystack, (6) VLA-14, and (7) Owens Valley Radio Observatory.

channel 57 ($V = 6.8$ km/s). The difference between the model curves and observational data does not exceed 10% in amplitude and 6° in phase. The high relative accuracy of measurements allowed us to distinguish components in the channels down to the 1% level over a wide range of brightness temperatures from 10^{11} to 10^{15} K.

4. STRUCTURE OF THE FLARE REGION

The supermaser emission is determined by a structure that consists of a chain of components with velocities that smoothly change with the relative positions of the components. Figure 4 presents radio maps of the supermaser emission at velocities of 5.79 to 9.15 km/s, averaged over pairs of channels. The velocity resolution is 0.14 km/s and the angular resolution 0.5 mas. With increasing velocity, the eastern emission (positive x) becomes more prominent. We combined all the maps in order to obtain a more complete representation of the structure (Fig. 5a). Figure 5a shows that the structure consists of an elongated bent chain of components with a length of 50 mas ($\sim$25 AU) and a half-power thickness of about 0.4 AU. The angular resolution is 0.5 mas. Two bright components separated by 5 mas, marked in the upper part of Fig. 5, can be distinguished in the structure. Their intensities are $I_1 \approx$ 350 kJy/beam or $T_{b1} \approx 4 \times 10^{15}$ K ($V_1 = 7.5$ km/s) and $I_2 \approx 260$ kJy/beam or $T_{b2} \approx 3 \times 10^{15}$ K ($V_2 = 7.8$ km/s). The brightnesses of the remaining components do not exceed $I \approx 1$ kJy/beam or $T_b \approx 10^{13}$ K. This significant brightness excess at a velocity of $\sim$7.7 km/s is typical for the entire period of activity, and can be explained by amplification of the emission

to the supermaser level in the ambient medium— an envelope with a radial velocity of $V \approx 7.6$ km/s. Evidence for this is also provided by the preservation of the velocity of the supermaser emission during the second period of activity in 1998−1999 [10].

We analyzed the fine structure of the components using the data obtained from the intercontinental baselines, in particular, Effelsberg−Haystack, Effelsberg−Green Bank, and Effelsberg−Owens Valley. We distinguish compact nuclei $\leq$0.1 mas in size at the centers of the brightest components (Fig. 5). The flux density of the two nuclei are 2600 and 750 in relative units or 12 and 3.4 kJy, see Fig. 6. Their brightness temperatures correspond to $T_b \approx 10^{16}$ K. The emission linewidths are $\sim$0.6 and $\sim$0.5 km/s. Similar nuclei are present in low- and high-velocity components located $\sim\pm$25 mas from the center, with fluxes of $\sim$2 kJy and brightness temperatures of $T_b \sim 10^{15}$ K.

5. AMPLIFICATION IN THE ENVELOPE

Amplification in the envelope changes the brightness of components and influences their effective positions and velocities. In the unsaturated amplification regime, the visible brightness temperature of the source is

$$T = T_b \exp[-\tau(V)] + T_{\text{env}}\{1 - \exp[-\tau(V)]\},$$

where $T_b \approx 10^{12}$ K is the brightness temperature of the structure, $T_{\text{env}} \approx 100$ K is the kinetic temperature, and $\tau(V) < 0$ is the optical depth of the maser amplifier; i.e., the envelope:

$$\tau(V) \approx e^{\frac{-(V-V_0)^2}{\Delta V^2}},$$

where V_0 is the velocity of the amplifying medium and ΔV is the amplification bandwidth (linewidth).
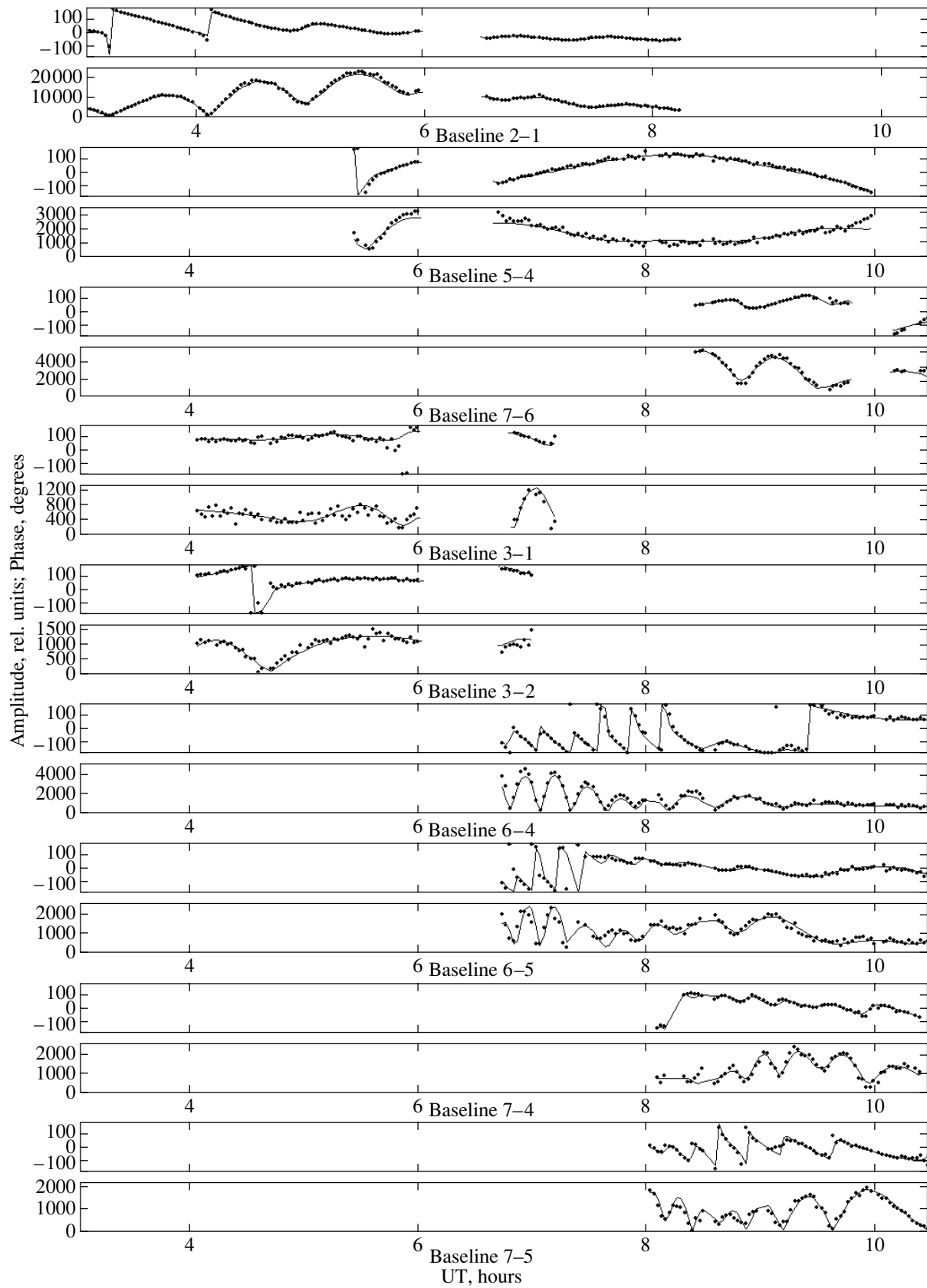
Fig. 3. Correlated flux densities and phases (channel 57) for the Orion KL maser flare at epoch 1985.8. See Fig. 2 for the participating antennas.
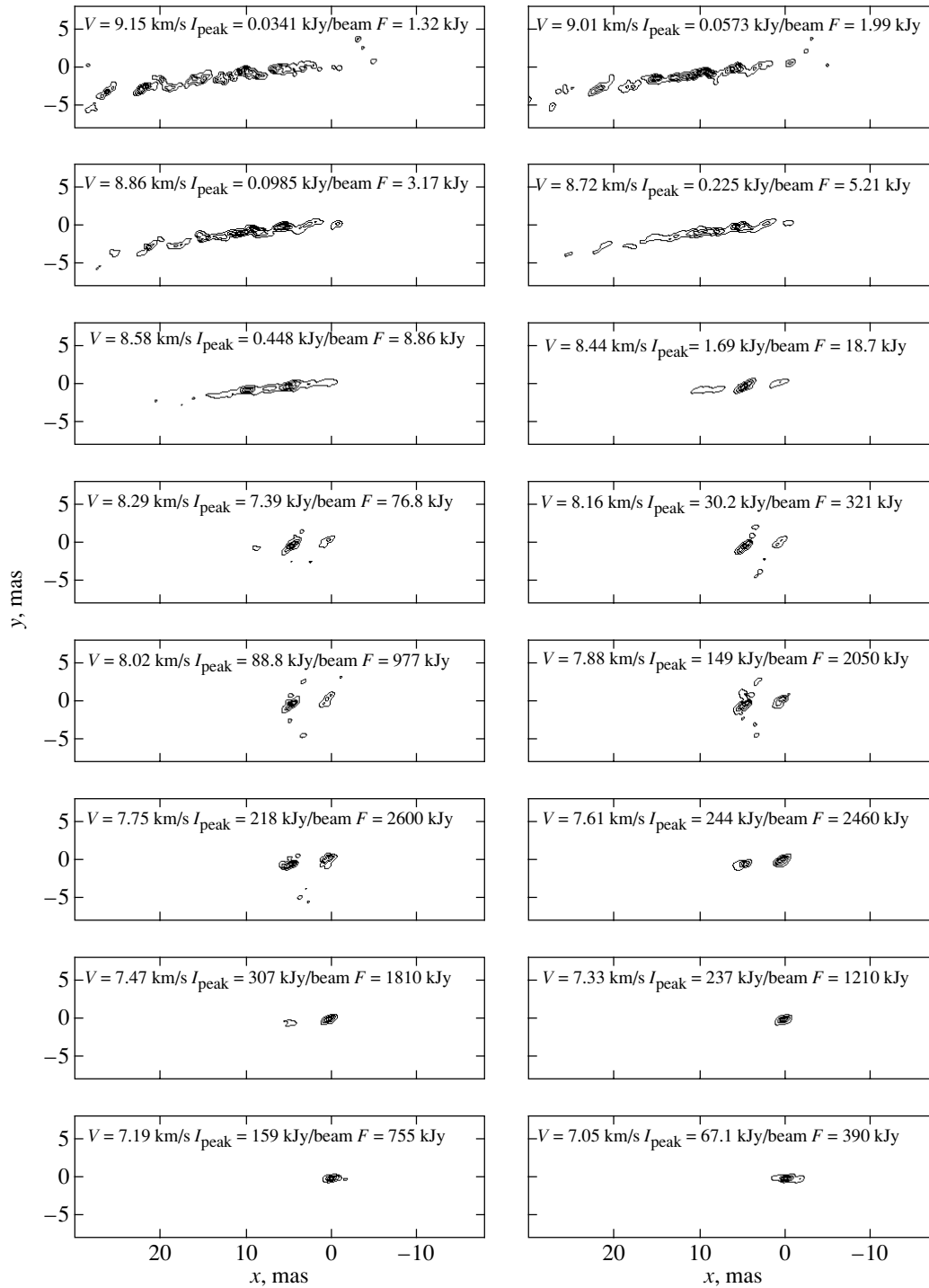
Fig. 4. Radio brightness distribution for the supermaser flare region in Orion KL ($V = 5.79 - 9.15$ km/s). The angular resolution is 0.5 mas, and the velocity resolution is 0.14 km/s. The contours correspond to 10, 30, 50, 70, 90% of the peak brightness.

The amplification is determined by the line profile and, to the first approximation, is Gaussian-like. The Doppler half-power linewidth is determined by the thermal-velocity dispersion of the molecules of mass M and the rms microturbulence velocity $\langle V \rangle$:

$$\Delta f_D = 2 f_{mn} / c [\ln 2 (2k T_k / M + \langle V \rangle^2)]^{0.5},$$

where f_{mn} is the frequency of the molecular line (22 GHz), c is the speed of light, and T_k is the kinetic temperature of the medium.

For a kinetic temperature of the water vapor molecules $T_k \sim 100$ K, the linewidth is $\Delta f_D = 37.6$ kHz or ~ 0.5 km/s. In the unsaturated maser
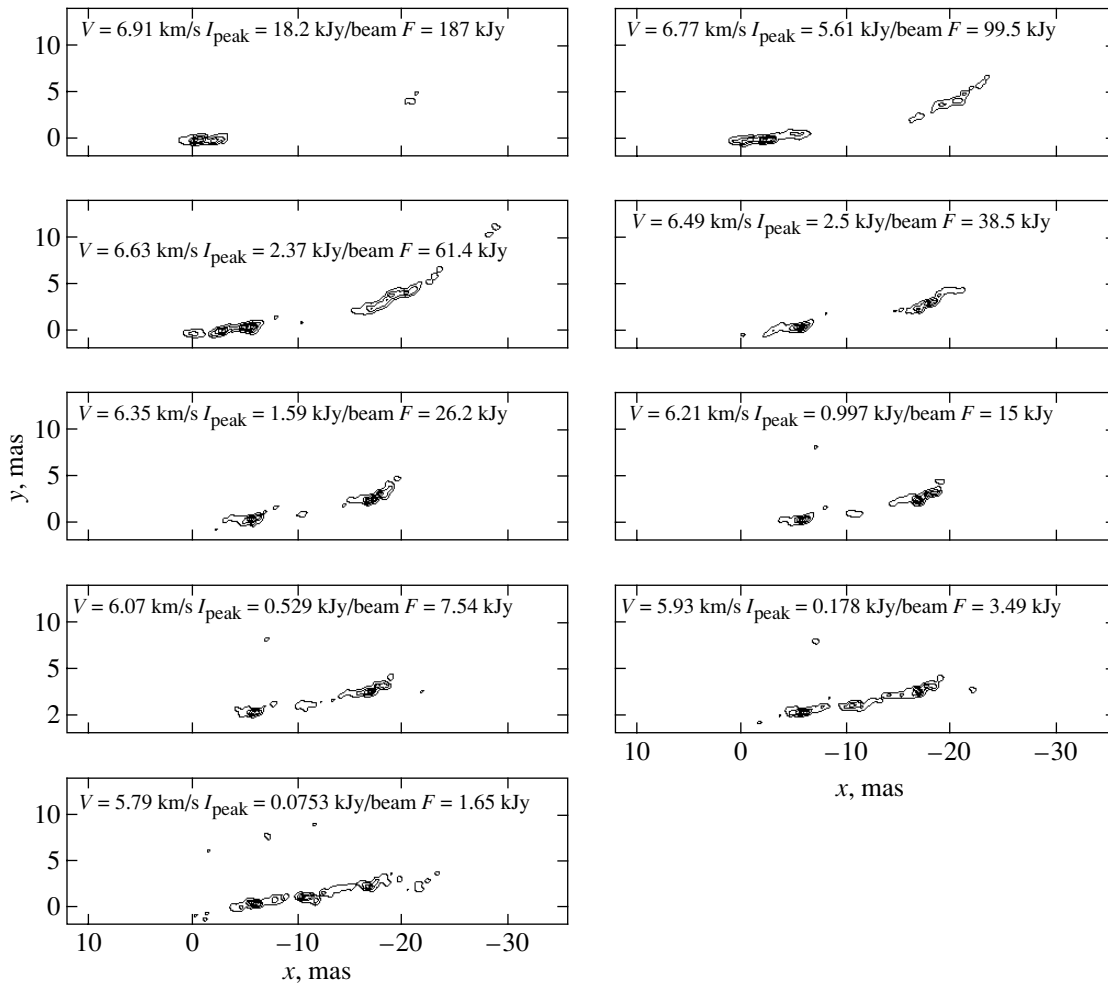
Fig. 4. (Contd.)

pumping regime, the linewidth would be a factor of $\tau^{0.5}$ narrower, however, microturbulence in the medium broadens the linewidth.

If we assume that the intensity of the compact components is approximately equal at all velocities, the observed amplified emission of the two components shown in Fig. 5a is determined by their amplification by a factor of $G_o \approx 200$ in the envelope with velocity $V = 7.6$ km/s and with a profile width of $\Delta V = 0.7$ km/s. Figure 5c shows the brightness distribution corrected for amplification in the envelope. The component velocities vary along the structure from 6.73 to 9.16 km/s, and their brightness temperatures are in the range $T_b = 10^{12}-10^{13}$ K. The effect of the finite angular resolution will be to reduce the brightness temperatures of components that are smaller than 0.5 mas. In this case, the actual amplification will be larger than the factor given above ($G_o \approx 200$).

6. MODEL OF THE FLARE REGION

The structure of the active region of maser flare emission shown in Fig. 5c corresponds to an accretion disk viewed edge-on. The disk is in the phase of separating into protoplanetary rings containing dirty ice particles. Water vapor forms during the sublimation of ice and produces a maser halo around the rings; the maximum optical depth of the rings is $\tau \geq 25$ in the tangential direction, and this direction corresponds to the bright compact sources. The maser emission is strongly directed and concentrated in the plane of the rings. This structure is surrounded by an envelope. The supermaser emission is produced by the amplification of the emission of components with velocities close to the velocity of the envelope ($V = 7.6$ km/s). Only the right-hand part of the disk is observed. The velocity of the opposite segment of the disk differs substantially from the observed velocity, and is beyond the range of our measurements.

The dependence of the relative velocities of the components ΔV on the distance ΔR (Fig. 7) implies
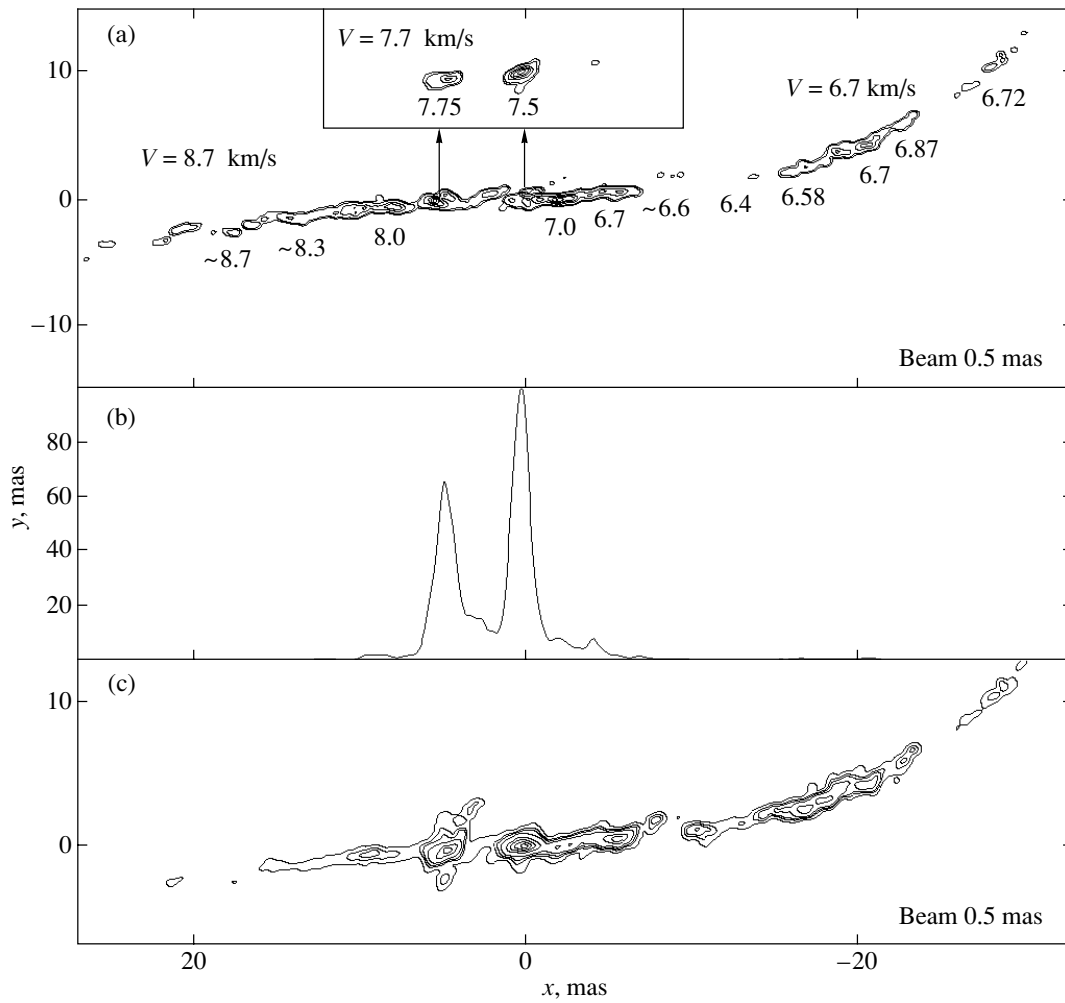
Fig. 5. General structure of the flare region: (a) velocities of 6.7, 7.7, and 8.7 km/s (the numbers in the diagram indicate the velocities of components in km/s, and the contours correspond to 5, 10, 30, 50, 70, and 90% of the peak brightness); (b) strip brightness distribution along the structure; (c) general structure corrected for amplification in the envelope (the contours correspond to 1, 3, 5, 10, 30, 50, 70, and 90% of the peak brightness).
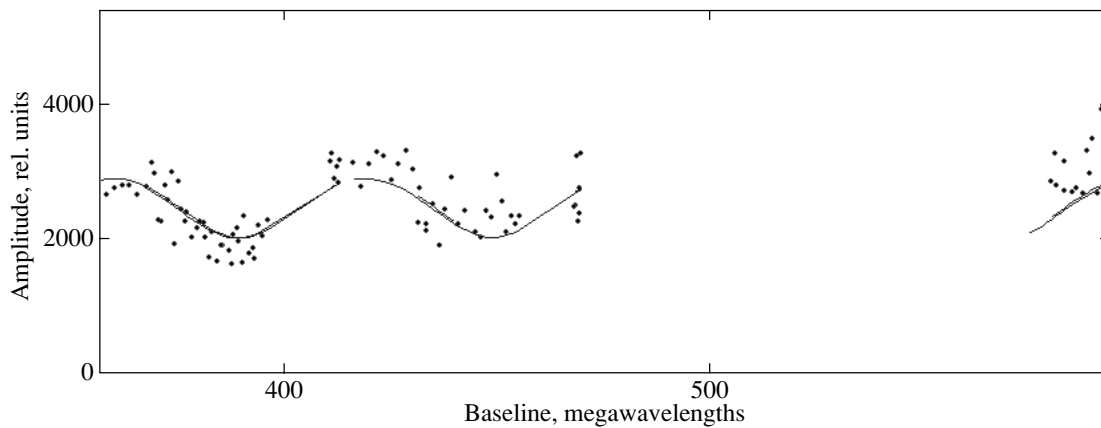
Fig. 6. The amplitude of the correlated flux from Orion KL on the longest intercontinental baselines (Effelsberg–Hayslack, Effelsberg–Owens Valley).
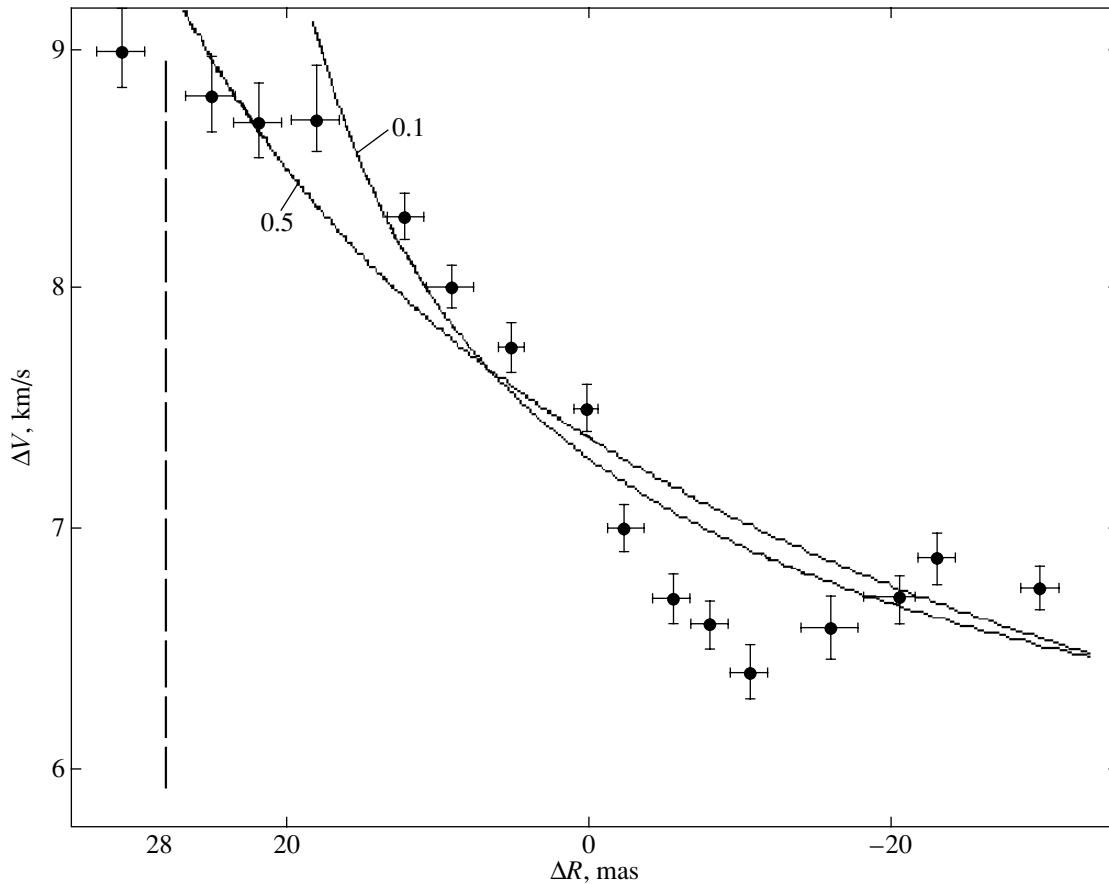
Fig. 7. Position of components vs. their velocity. The lines correspond to Keplerian rotation, $RV^2 = MG$, for $M = 0.1$ and $0.5M_\odot$.

Keplerian motion. We do not know the velocity of the central body relative to the Local Standard of Rest. The asymptote of the dependence $\Delta V - \Delta R$ for increasing ΔR gives an upper limit of $V_{LSR} \leq 6$ km/s (Fig. 7). The position of the rotational axis is defined by the vertical asymptote, which approaches $\Delta R \geq 28$ mas (or 14 AU). The mass of the central body is in the range $M = 0.1{-}0.5M_\odot$. For $M = 0.1M_\odot$, the velocity of the central body is $V_{LSR} = 4.7$ km/s, whereas $V_{LSR} = 3.3$ km/s for $M = 0.5M_\odot$. The zero-point $\Delta R = 0$ in Fig. 7 corresponds to $R = 28$ mas and $R = 52$ mas, respectively. The calculated curves shown in Fig. 7 correspond to these two cases. For $M = 0.1M_\odot$, the radius of the inner ring is $R_{\mathrm{min}} \approx 5$ AU and the rotational velocity is $V_{\mathrm{rot}} = 4$ km/s, the radius of the maser disk (outer ring) is $R_{\mathrm{max}} \approx 29$ AU and the rotational velocity is $V_{\mathrm{rot}} = 2$ km/s. For $M = 0.5M_\odot$, $R_{\mathrm{min}} \approx 13$ AU, $V_{\mathrm{rot}} = 5.7$ km/s, and $R_{\mathrm{max}} \approx 41$ AU, $V_{\mathrm{rot}} = 3$ km/s. The planes of the distant rings deviate from the planes of the rings in the central part of the disk by $\sim 7°$, probably due to disturbance of the disk by accreting matter.

The observed deviations of the points from Keplerian motion may be due to the expansion velocities of water molecules that are blown off by the stellar wind and radiation pressure, forming an expanding halo around the ring (an expanding maser ring). The radial component of the velocity could also originate due to nonstationarity in the initial phase of formation of the system.

The emission is amplified in the envelope (the ambient medium) by a factor of $G \approx 200$; this corresponds to an optical depth of $\tau \approx 5.3$ in the unsaturated regime. The amplification profile width is a factor of 2.3 narrower than the thermal linewidth (~ 0.5 km/s), and is equal to 0.2 km/s. However, the observed amplification profile width is 0.7 km/s. This broadening may be due to saturation of the maser pumping. However, it is more likely determined by either microturbulence in the ambient medium or the velocity gradient in the maser amplifier (envelope), which is equal to ~ 1.1 km/s. The velocity of the envelope relative to the central object is $V_{\mathrm{env}} = 2.9$ km/s (for $M = 0.1M_\odot$), and is directed toward the central

object. For $M = 0.5M_\odot$, the rate at which the envelope is accreted is $V_{\mathrm{env}} = 4.3$ km/s.

7. CONCLUSION

We have carried out observations of an H_2O supermaser flare in Orion KL at epoch 1985.8 using a global VLBI array. We resolved the fine spatial structure of the flare region with an angular resolution of 0.5 mas at a wide range of velocities from 5.79 to 9.15 km/s (in steps of 0.07 km/s).

The region of maser emission is a bent extended structure 25 AU long and 0.4 AU wide, with compact components distributed inside this structure. The maximum brightness temperatures of two of these approach $T_b \approx 4 \times 10^{15}$ K and $T_b \approx 3 \times 10^{15}$ K. The brightnesses of the remaining components do not exceed $T_b \leq 10^{13}$ K. Compact nuclei smaller than 0.1 mas are present at the centers of these components. The brightness temperatures of the nuclei of the two brightest components approach $T_b \sim 10^{16}$ K.

This structure corresponds to an accretion disk viewed edge-on. The disk is in the stage of separating into protoplanetary rings. The inclination of the distant rings differs from the inclination of the rings in the central part of the structure, probably due to an asymmetric external disturbance. The compact bright components correspond to the tangential directions of the rings. The ring emission is concentrated in the azimuthal plane, so that their visibility is restricted. This implies periodicity of the high maser activity, which is determined by the precession rate.

The velocities of components depend on their relative positions, and correspond to Keplerian motion around an object with mass $M = 0.3 \pm 0.2M_\odot$. Its velocity relative to the Local Standard of Rest is $V_{LSR} = 4 \pm 0.7$ km/s. The radius of the inner ring is $R_{\min} = 9 \pm 4$ AU, and its rotational velocity is $V_{\mathrm{rot}} = 5 \pm 1$ km/s. The radius of the disk is $R_{\max} = 35 \pm 6$ AU, with $V_{\mathrm{rot}} = 2.5 \pm 0.5$ km/s.

The H_2O supermaser emission is associated with additional amplification of the emission of the protoplanetary rings at a velocity of $V = 7.6$ km/s by more than two orders of magnitude. This amplification occurs in the external medium, in an envelope with a profile width of 0.7 km/s. The envelope is being accreted onto the central body at a rate of $V \approx 3.6 \pm 0.7$ km/s. The velocity gradient within this envelope is $\Delta V \approx 1.1$ km/s.

ACKNOWLEDGMENTS

REFERENCES

1. R. Genzel, D. Downes, J. M. Moran, *et al.*, Astron. Astrophys. **66**, 13 (1978).
2. Z. Abraham, J. W. S. Vilas Boas, and L. F. del Ciampo, Astron. Astrophys. **167**, 311 (1986).
3. L. I. Matveenko, Pis'ma Astron. Zh. **20**, 456 (1994) [Astron. Lett. **20**, 388 (1994)].
4. L. I. Matveyenko, Pis'ma Astron. Zh. **7**, 100 (1981) [Sov. Astron. Lett. **7**, 54 (1981)].
5. V. A. Demichev, K. M. Zakharin, and L. I. Matveenko, Astron. Zh. **80**, 118 (2003) [Astron. Rep. **47**, 99 (2003)].
6. L. I. Matveyenko, P. J. Diamond, D. A. Graham, and W. Junor, in *Astrophysical Masers* (Arlington, Virginia, USA, 1992), p. 176.
7. L. I. Matveenko, D. A. Graham, and P. J. Diamond, Pis'ma Astron. Zh. **14**, 1101 (1988) [Sov. Astron. Lett. **14**, 468 (1988)].
8. V. A. Demichev and L. I. Matveyenko, Baltic Astron. **13**, 478 (2003).
9. J. A. Högbom, Astron. Astrophys., Suppl. Ser. **15**, 417 (1974).
10. L. I. Matveenko, K. M. Zakharin, P. J. Diamond, and D. A. Graham, Pis'ma Astron. Zh. **32**, 121 (2004).

Translated by L. Yungel'son

A Study of the Star-Forming Group RNO 129

T. A. Movsessian and T. Yu. Magakian

Ambartsumian Astrophysical Observatory, Academy of Sciences of Armenia, Byurakan, 378433 Armenia
Received March 10, 2004; in final form, July 15, 2004

Abstract—We have studied the compact star-forming group RNO 129 in the cloud L1228. New images and both slit and integrated spectroscopy for several nebulas and HH objects are presented. We have detected several new HH objects, including two blobs embedded in a bright reflection nebula. The central star of this nebula is binary and is ejecting at least one collimated jet. Some peculiarities in the spectrum of the nebula indicate its similarity with NGC 2261. © *2004 MAIK "Nauka/Interperiodica"*.

1. INTRODUCTION

It is considered proven that directed flows of matter are observed in very young stars (so-called "young stellar objects"—YSOs)[1]. The presence of Herbig—Haro (HH) objects in stellar aggregates and molecular clouds formed in the course of these outflows provides evidence for active star formation. YSOs tend to be concentrated in compact regions, sometimes forming sets of collimated outflows and ejections. Searches for and studies of various manifestations of YSOs are essential if we wish to uncover a consistent pattern for the origin and evolution of low- and medium-luminosity stars.

The nebulous object RNO 129 [2] is the most northern (according to its declination) of all known compact star-formation regions ($\alpha = 20^{\rm h}59^{\rm m}13.6^{\rm s}$, $\delta = +78°23'04''$, J2000). The nebula is located in the dark cloud L1228 in Cepheus, at a distance of $\sim$300 pc [5]. RNO 129 is also known as Be 48 [3] and GN 21.00.4.01 [4].

Slit spectra of the central star of RNO 129 have revealed emission typical of HH objects, as well as some peculiarities in the reflected spectrum of the nebula [6]. On this basis, it was suggested in 1988 that the object is associated with a directed outflow. Subsequent observations confirmed the presence of a jet and an HH object located in the vicinity of the main nebula [7]. Later, RNO 129 was detected in searches for emission-line stars [8], IR sources [9], and HH objects [10, 11]. The latest of these studies confirmed the presence of HH objects in the region (denoted HH 198) and again investigated the anomalous spectrum of the compact reflection nebula in RNO 129. Other HH flows were also found in L1228, indicating a high star-formation rate.

Detailed studies of RNO 129 are complicated by the small size and complex structure of the object. New observations were needed to elucidate the nature of the nebula. Two-dimensional spectroscopic data are most valuable in this regard.

2. OBSERVATIONS

RNO 129 was observed with the 6-m telescope of the Special Astrophysical Observatory of the Russian Academy of Sciences and the 2.6-m telescope of the Byurakan Observatory.

The direct images of the object presented here were obtained on October 15, 1998 with the ByuFOSC camera [12] installed at the prime focus of the 2.6 telescope, using a narrow-band filter corresponding to the [SII] emission line ($\lambda_c = 6730$ Å, $\Delta\lambda = 75$ Å) and a broad-band I filter ($\lambda_c = 8500$ Å, $\Delta\lambda = 1200$ Å). The field of view was $5.5' \times 11'$, with a scale of $0.65''$/pixel. The total exposure in the [SII] filter was 3600 s and in the I filter was 300 s; the images were recorded with a Thomson 1060×514 CCD.

We carried out slit spectroscopy of RNO 129 several times in 1984—1995 with the 6-m telescope using various equipment, including a photon-counting 1024-channel scanner (1984—1986), echelle spectrograph (1991), and long-slit spectrograph (1986 and 1995). The light was recorded using a 512×512 photon-counting system; a 530×580 CCD was used in 1995. The data were processed in the MIDAS system developed at the European Southern Observatory.

Integrated spectroscopy was carried out on July 25, 2000 using the VAGR multipupil spectrograph [13] mounted at the prime focus of the 2.6-m telescope, together with the same Thomson CCD detector. The total exposure was 3600 s. The field of the multipupil spectrograph was $20'' \times 40''$, with a scale of $1.2''$ by the pupil. To avoid overlapping of
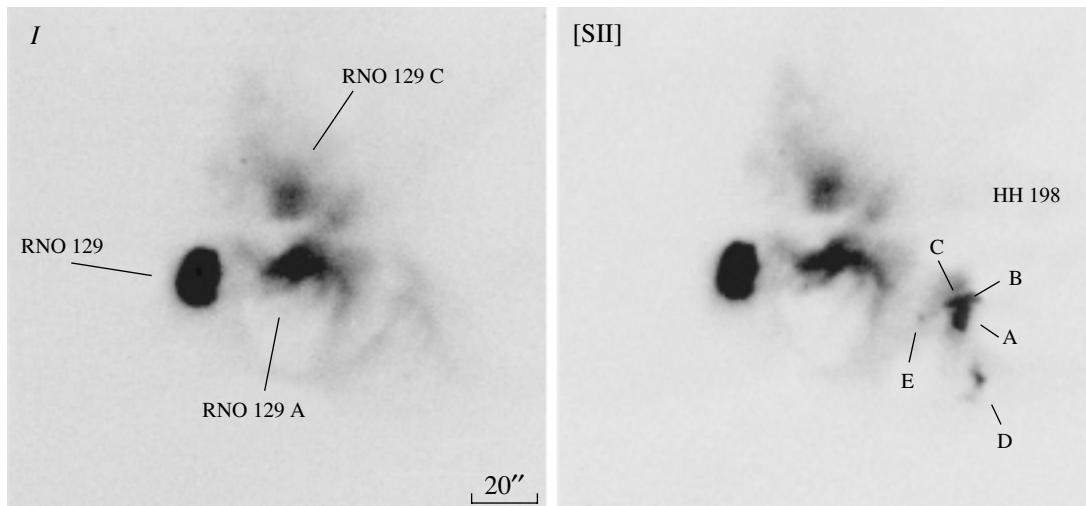
Fig. 1. RNO 129 in the I-band continuum (left) and the [SII] emission line (right). The main components of the group and blobs in the object HH 198 are marked.

the spectra, a narrow-band filter transparent to the red [SII] $\lambda6716 + \lambda6731$ Å doublet was used.

The integrated spectroscopic data were processed with the ADHOCw package, developed at the Marseille Observatory (http://www-obs.cnrs-mrs.fr/ADHOC/adhoc.html). The individual spectra were automatically extracted and subjected to wavelength calibration. These data were used to construct [SII] line and continuum maps of the object, as well as to determine the radial velocities of lines.

3. THE MORPHOLOGY OF RNO 129

In the studied region, we can see a moderate-size group of bright and dark dust nebulas with signs of filamentary structure. The entire group is embedded in a faint conelike nebulous envelope directed towards the northwest, with the dominant central object (essentially, RNO 129) at the tip. The central object is a star of about 16^m closely surrounded by a compact nebula with high surface brightness and sharp edges, which extends to the north about 15″. Another distinct reflection nebula (object A of [6]) can be seen $\sim$30″ to the east of the central object. It appears to be a separate formation illuminated by a faint star at its center. This nebula displays signs of bipolar structure, and its central star stands out clearly in I images, being even more prominent in near-IR 2MASS frames. Note also that the nebula is adjacent to a region of particularly strong absorption in the south. Another reflection nebula that is not related directly to any star (object C) lies to the north of object A. The bright object HH 198 is located further from and to the west of the central star (it was tentatively denoted the RNO 129B nebula in [6]). All these components

of the RNO 129 group are clearly visible in Fig. 1, which presents I continuum and [SII] line images of the region. Neither the shape of the nebula nor the mutual positions of the objects in it indicate directly which of the stars is the source of HH 198. At the same time, it is clear that HH 198 consists of at least three individual condensations, which we denote in Fig. 1 blobs A, B, and C; in addition, another blob that also displays signs of internal structure (HH 198D) lies to the south. Another probable blob (HH 198E) lies directly to the east.

Because the continuum surface brightness of the main object is so high (especially in its southern part), it is difficult to distinguish the star against the bright background of the nebula. This makes RNO 129 similar to the star R Mon, which lies at the vertex of a bright nebulous triangle, against which it is barely discernable. An image with a short integration time enabled us to see the core of the object directly, which is elongated, suggesting that the central star is binary. It consists of two components with comparable brightnesses separated by 2−2.5″ in position angle 60°. Note also the curious variations in the shape of the nebula: while it is generally directed roughly toward the north from the star (the position angle is about 343°), its bright inner part bends towards the east. All these features are clearly visible in the continuum map of the object presented in Fig. 2. Apart from the group HH 198, several small emitting HH blobs are detected inside the bright nebula RNO 129 after subtraction of the continuum image from the [SII] image. Although these are very hard to analyze due to the bright continuum background, their existence is beyond doubt, as is shown by the integrated spectroscopic data (see Section 5).
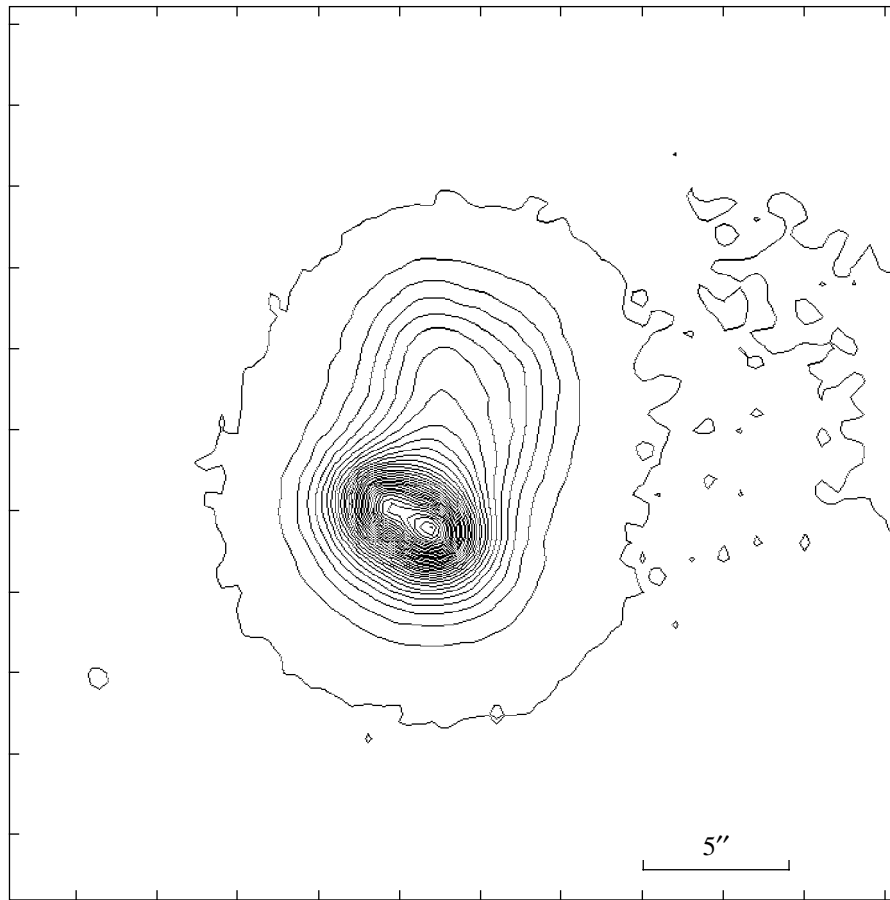
Fig. 2. Isophotes of the central star of RNO 129 and its reflection nebula in the *I* continuum. The binarity of the star is clearly visible.

4. SLIT SPECTROSCOPY

We have carried out spectroscopic observations of the central star and adjacent nebula on several occasions. Our first observations were described in detail in [6]. We selected several of the most typical spectrograms from the data we obtained later to use as illustrations (Figs. 3 and 4).

The general appearance of the continuum emission indicates that the spectral type of the RNO 129 star is rather late. More accurate classification is complicated by the faintness of the photospheric absorption lines of the star. The MgI triplet is the easiest to recognize, primarily via its strongest $\lambda5184$ Å line. This suggests that the spectrum of the star displays so-called veiling, which is typical of active T Tauri stars. The veiling sometimes becomes weaker: for example, observations obtained in 1985 display distinct gaps in the continuum, which can be identified with TiO bands and whose strength corresponds to a spectral type of approximately K8, which we adopted as a preliminary classification.

This late-type spectrum is superimposed with emission lines typical of T Tauri stars. The number and equivalent width of these lines are basically consistent with the previous data of [6], since the spectral variability of the emission spectrum is expressed via small oscillations of the intensities of the FeII and FeI lines. The CaII emission-line intensities may also vary, but we cannot be sure of this, given the weakness of the UV continuum. Based on measurements covering several years, the average radial velocity of the Hα and Hβ emission lines in the spectrum of the star are $+61 \pm 12$ km/s and $+53 \pm 32$ km/s, respectively (from now on, all quoted velocities will be heliocentric). The forbidden emission lines display appreciable blue shifts; the average velocities are -75 ± 11 km/s for the [OI] $\lambda6300$ Å line, -89 ± 23 km/s for the [SII] $\lambda6716$ Å line, and -70 ± 26 km/s for the [SII] $\lambda6731$ Å line. The radiation in the stellar envelope may be stratified, since the negative velocity is even larger for the [SII] $\lambda4068$ Å line (-191 ± 20 km/s), while it is only -23 km/s for the [NII] $\lambda6548$ Å line. Note
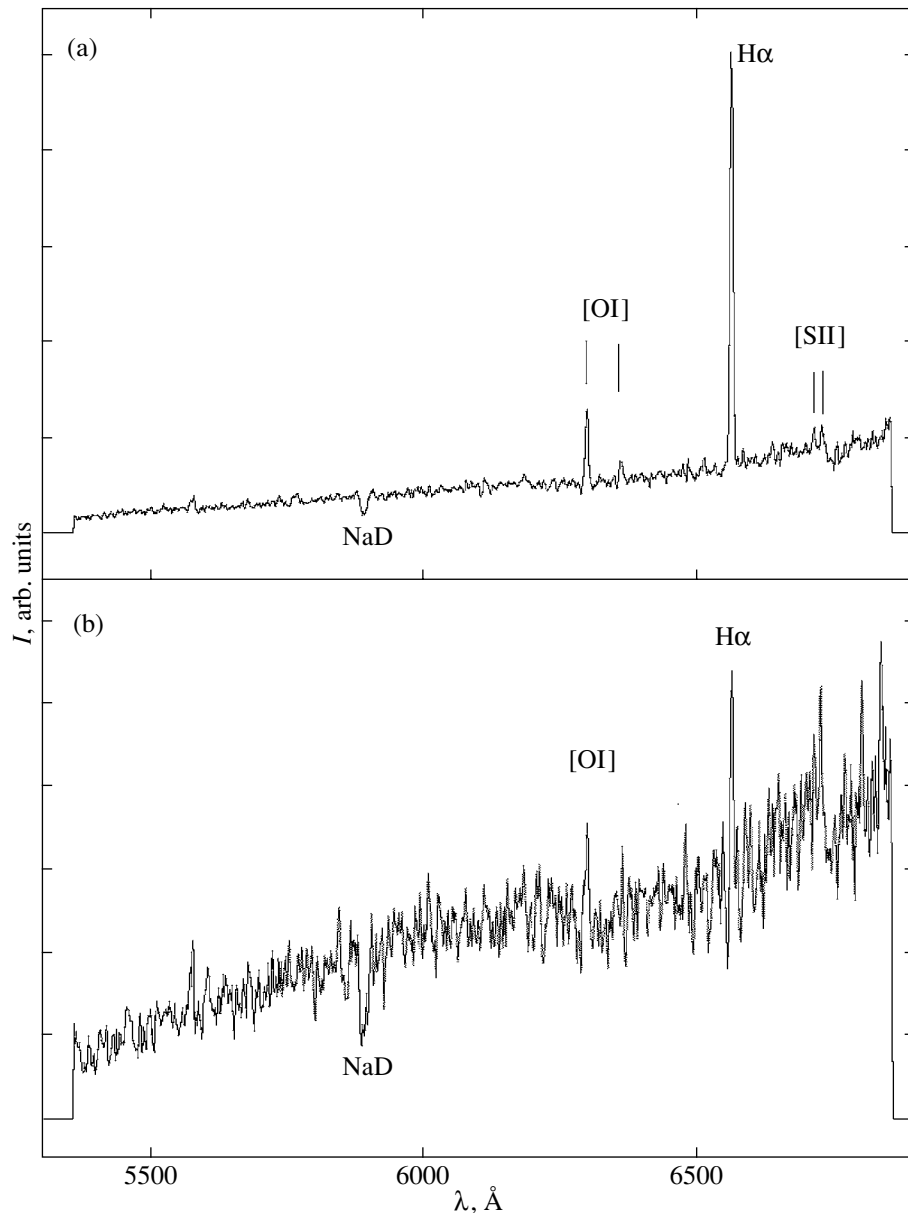
Fig. 3. The spectra of the RNO 129 (a) star and (b) nebula in relative intensities at red wavelengths obtained on December 17, 1984 with the 6-m telescope equipped with the 1024-channel scanner.

also that these lines are substantially weaker, so these measurements may be less reliable. The general development of the the T Tauri spectrum is fairly moderate, and is not comparable to that for such objects as R Mon or V350 Cep [14]. This is confirmed by the echelle spectrum of the star, which has high resolution and covers a large wavelength interval, and also displays a very steep Balmer decrement and a two-peaked structure for the Hα and Hβ lines. It is also obvious that the [SII] emission lines are broad and consist of several components. Note also that the intensity ratio for the [SII] lines is essentially constant, and often corresponds to the upper limit;

i.e., the electron density is very high and reaches at least 5000–6000 cm^{-3}. In addition to the forbidden lines, the absorption components of the Balmer lines and the NaD absorption lines display negative radial velocities.

The new data have fully confirmed the anomalous nature of the reflection spectrum of the nebula, which differs radically from a stellar spectrum in the sharp increase in the intensities of the absorption components of several lines, primarily those in the Balmer series. At the same time, the intensities of essentially all emission lines generally decrease. It is particularly noticeable that not only the Balmer lines, but also
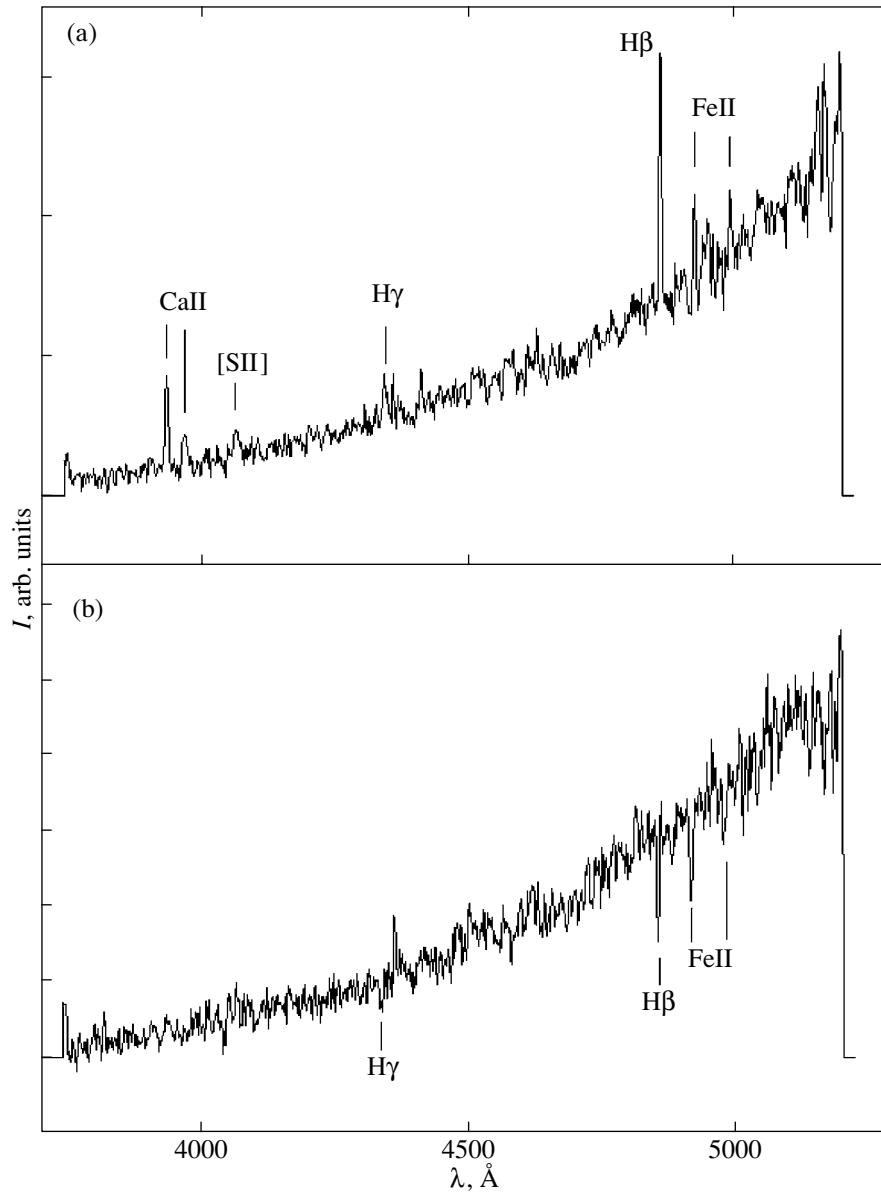
Fig. 4. Same as Fig. 3 at blue wavelengths.

several of the most intense FeII lines, are transformed from emission to absorption, as can clearly be seen in the pairs of spectra obtained on December 17, 1984 (Fig. 4). All these absorption lines display strong blue shifts (from −200 to −300 km/s, appreciably larger than the shifts for the forbidden emission lines). The conclusion of [6] that the intensity and negative radial velocity of the NaD absorption lines remain essentially constant in the transition from the stellar to the nebular spectrum is also confirmed.

The echelle spectrograms confirm the scanning observations, and suggest that, like [SII], the shifted absorption lines consist of several components. The continuum energy distributions of the nebula and star are roughly the same, but the equivalent widths of the absorption components are rather different.

We also obtained several long-slit spectra of the object in different position angles. These revealed a faint and appreciably blue-shifted Hα emission that extends 5−6″ to the north of the continuum emission of the star [7] and is probably formed by a collimated flow. The K8 spectral type for the star was also confirmed, as well as the decrease of the emission-line equivalent widths in the spectrum of the nebula. In addition, our observations clearly demonstrate that the spectrum of the nebula varies from point to point. This can be elucidated only via integrated spectroscopy using multipupil systems.

Apart from the main star and nebula, we also observed the object HH 198 with the long slit. Its integrated spectrum indicates that the basic object (blobs A, B, and C) possesses a fairly high excitation (judging from the [NII]/Hα line ratio) and a moderate electron density ($500-700$ cm^{-3} based on the [SII] lines). The [OI] lines in the spectrum are so faint that they are essentially indistinguishable against the background emission of the night sky. Despite the complex structure of the object, the internal dispersion of the radial velocities was insignificant, although the radial velocity varies across the object: from -29 ± 13 km/s in the western part, to -51 ± 8 km/s in the center, and -98 ± 15 km/s in the eastern part. Note that these data are in good consistency with the earlier estimates of [7].

5. INTEGRATED SPECTROSCOPY

Multipupil spectroscopy makes it possible to obtain spectra for individual sections of an extended object, and thereby construct maps of the intensity distributions of spectral lines or other physical parameters. Figure 5 presents images of the object in the [SII] line and in the continuum derived from the observations with the VAGR system.

Two emission condensations denoted a and b are clearly visible against the background of the reflection nebula. Blob a is located $\sim$2.5$''$ to the north of the central star. The intensity of its lines even exceeds those of the central star, whose spectrum also displays [SII] line emission; however, the blob is nearly indistinguishable in the direct images due to the high surface brightness of the reflection nebula. It probably corresponds to the shifted emission lines seen in the long-slit spectra described above. Since the integrated spectroscopic data enable us to derive pseudo-long-slit spectra for arbitrary slit orientations, we constructed a position–velocity diagram for a north–south orientation of the pseudoslit, for comparison with the spectrum of [7] (Fig. 6). These data, which were obtained using completely different methods, are perfectly consistent.

Blob b is located $\sim$8$''$ to the northwest of the star, and is substantially weaker. Curiously, it lies along essentially the same line as blob a and the secondary component of the central star (whose position is marked with the cross in Fig. 5). In contrast to its appearance in the I images, this component is barely visible in the reconstructed continuum image, which may indicate that it is very red; however, it is also possible that it is variable.

The radial velocities of both blobs were determined from two S lines, and were found to be -103 km/s for blob a and -140 km/s for blob b, with a dispersion
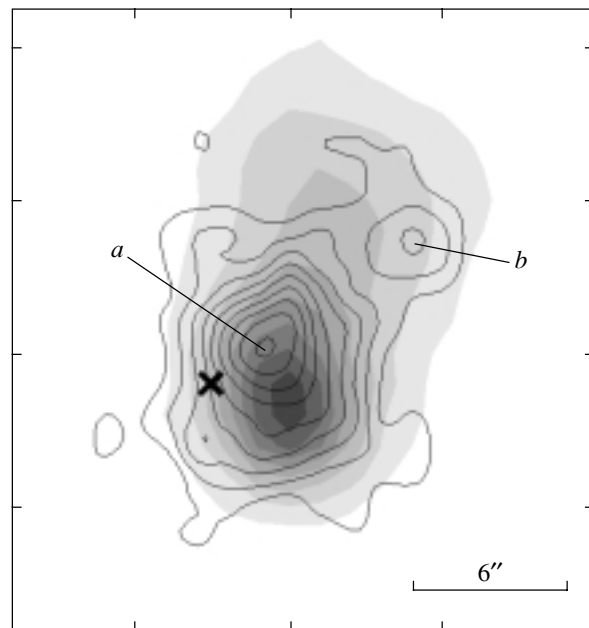
Fig. 5. Images of the RNO 129 nebula in the [SII] $\lambda6716 + \lambda6731$ Å lines (contours) and in the continuum (grey scale) reconstructed from the integrated spectroscopic data. Two HH blobs are denoted a and b. The cross indicates the approximate position of the secondary component of the central star.

of $\pm$20 km/s. Systematic errors may also be present here. The electron density of blob a derived from the [SII] line ratio is fairly high—almost the same as in the vicinity of the star (see Section 4), $\sim$5000 cm^{-3}. The density in blob b is appreciably lower, about 500 cm^{-3}.

6. CONCLUSION

Our results clearly indicate that RNO 129 is a compact star-formation group containing at least three young stars. Its spectral properties and the presence of HH objects indicate collimated outflows. The central object in the front portion of the general nebular structure, in which the stars are embedded, is particularly active, and illuminates its own bright cometlike nebula. Our observations have shown that the central star is binary.

Long-term spectral studies of the object identify it with reasonable certainty as a T Tauri star with a pronounced emission spectrum containing clearly visible forbidden lines. The emission lines probably originate in both components. The presence of shifted forbidden emission lines indicates that the main component produces a collimated flow. Other indirect evidence for a directed outflow is provided by the cometlike nebula, whose spectral peculiarities are similar to those of NGC 2261 [15, 16]. Thus, the RNO 129 nebula
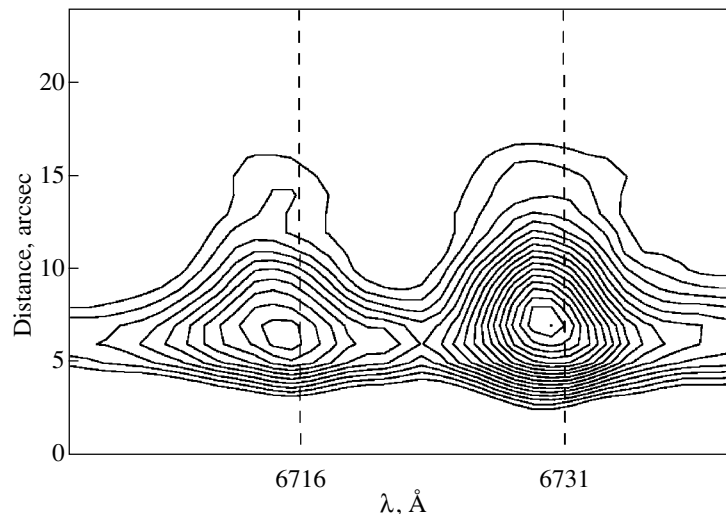
Fig. 6. Position−velocity diagram for the region of the [SII] $\lambda6716 + \lambda6731$ Å lines derived from the integrated spectroscopic data. The coordinate axis is directed from north to south and contains the central star (located in the lower part of the figure). The dashed lines mark the wavelengths corresponding to zero radial velocity.

presents a second well defined example of "spectral asymmetry," and as such is worthy of further study.

In addition, two small emission blobs with HH spectra were detected inside the reflection nebula in RNO 129. They lie on a straight line far from the axis of symmetry of the nebula (the position angles are 305° and 343°, respectively). This pattern is unusual for cometlike nebulas, since collimated outflows are usually directed along the axis of the nebula, perpendicular to the circumstellar disk. The flow may be ejected by the secondary component, closer to its own axis. Since few examples of young multiple stars producing multiple jets oriented in sharply differing directions are known, further studies of this system are of particular interest.

It is clear that the very red faint star at the center of the nebula RNO 129A displaying Hα emission is also a post-main-sequence object. The extent of its activity—in particular, whether it is a source of collimated outflows—is yet to be determined. The origin of the bright HH object HH 198 also remains unclear, and neither its location within the group nor its radial velocity provide conclusive evidence about its nature.

REFERENCES

1. B. Reipurth and J. Bally, Annu. Rev. Astron. Astrophys. **39**, 403 (2001).

2. M. Cohen, Astron. J. **85**, 29 (1980).

3. C. Bernes, Astron. Astrophys., Suppl. Ser. **29**, 65 (1977).

4. T. Neckel and H. Vehrenberg, *Atlas of Galactic Nebulae* (Treugesell Verlag, Dusseldorf, 1985−1990), Vols. I−III.

5. L. K. Haikala and R. J. Laureijs, Astron. Astrophys. **223**, 287 (1989).

6. T. Yu. Magakyan and E. E. Khachikyan, Astrofizika **28**, 139 (1988).

7. T. Yu. Magakian and T. A. Movsessian, *IAU Symp. No. 137: Flare Stars in Star Clusters, Associations and the Solar Vicinity*, Ed. by L. V. Mirzoyan *et al.* (1990), Vol. 267.

8. K. Ogura and F. Sato, Publ. Astron. Soc. Jpn. **42**, 583 (1990).

9. P. Persi, M. Ferrari-Toniolo, M. Busso, *et al.*, Astron. J. **95**, 1167 (1988).

10. E. W. Brugel and R. A. Fesen, Bull. Am. Astron. Soc. **22**, 1258 (1990).

11. J. Bally, D. Devine, R. A. Fesen, and A. P. Lane, Astrophys. J. **454**, 345 (1995).

12. T. Movsessian, J. Boulesteix, J.-L. Gash, *et al.*, Baltic Astron. **9**, 652 (2000).

13. T. Movsessian, J.-L. Gash, J. Boulesteix, and F. Zhamkotsian, Baltic Astron. **9**, 518 (2000).

14. T. Yu. Magakian, T. A. Movsessian, and E. R. Oganesyan, Astrofizika **42**, 165 (1999).

15. B. F. Jones and G. H. Herbig, Astron. J. **87**, 1223 (1982).

16. T. Yu. Magakian and T. A. Movsessian, *IAU Symp. No. 182: Low Mass Star Formation: from Infall to Outflow*, Ed. by F. Malbet and A. Castets (1997), Vol. 158 (poster proceedings).

Translated by K. Maslennikov

Star Formation and the Kinematics of Gas in the Disk of NGC 628

F. Kh. Sakhibov[1,2] and M. A. Smirnov[1]

[1]*Institute of Astrophysics, Academy of Sciences of Tajikistan, ul. Bukhoro 22, Dushanbe, 734670 Tajikistan*
[2]*Institute of Astronomy, Russian Academy of Sciences, Pyatnitskaya ul. 48, Moscow, 119017 Russia*
Received August 28, 2003; in final form, July 15, 2004

Abstract—The radial profile of the star-formation rate (SFR) in the galaxy NGC 628 is shown to be modulated by a spiral-density wave. The radial profile of the velocity of gas inflow into the spiral arm is similar to the radial distribution of the surface density of the SFR. The position of the corotation resonance is determined along with other parameters of the spiral-density wave via a Fourier analysis of the azimuthal distribution of the observed radial velocities in annular zones of the disk of NGC 628. The radial profile of the surface density of the SFR is determined using the empirical SFR—linear size relation for star-formation complexes (giant HII regions) and measurements of the coordinates, Hα fluxes, and the sizes of HII regions in NGC 628. © *2004 MAIK "Nauka/Interperiodica"*.

1. INTRODUCTION

The emergence of density-wave theory has shed new light on the problem of star formation in galaxy disks. A density wave traveling through the disk of a galaxy produces a shock in the gas, which should favor the formation of stars in the spiral arms. This can easily explain the observed concentration of young stars in spiral arms. Many studies of spiral structure in galaxies compare various observational data in order to try to link star formation with spiral-density waves in disks. These comparisons are mostly qualitative. In this respect, the diagram of Roberts *et al.* [1], which relates the expected velocity of gas inflow into the spiral arm and the magnitude of the spiral-arm shock with the morphological characteristics of the spiral structure and van den Bergh luminosity classes is very illustrative. The earlier the luminosity class of the galaxy (i.e., the higher its luminosity), the brighter and more conspicuous the spiral pattern it possesses. In this case, the galactic gas meets the spiral arm at a higher velocity. The higher this velocity, the higher the degree of compression of gas and the higher the luminosity of the galaxy. To directly compare the velocity of gas inflow into the spiral arm, the amplitude of the gravitational potential of spirals, the density jump in the gas, or the position of the corotation resonance with the distribution of the star-formation rate (SFR) in the disk, we must know the field of the spiral-density perturbations produced by the density wave. This requires high-quality and sufficiently dense observations of the two-dimensional velocity field of the gas in the disk,

as well as complete catalogs of HII regions with measured positions and Hα fluxes (or sizes). The two-dimensional radial-velocity field contains information about the characteristics of the spiral-density wave that is distorting the circular rotation of matter in the disk. The radial distribution of the surface density of the SFR in the disk is then computed from the known fluxes (or linear sizes) and coordinates of HII regions.

The aim of the present paper is to compare the radial behavior of the SFR with the radial dependence of the velocity of gas inflow into the spiral arm and the positions of the corotation and Lindblad resonances in the disk of a spiral galaxy. Observations of the velocity field in the disk are available for only a few galaxies for which complete catalogs of HII regions are available, which can be used to analyze the relation between the SFR and the parameters of the density wave. One such well studied object is the spiral galaxy NGC 628.

The outline of this paper is as follows. Section 2 discusses the perturbations of the velocity field in a galactic disk produced by a spiral-density wave. Section 3 describes the method we use to allow for non-circular motions and to determine the position of the corotation resonance and other characteristics of the spiral-density wave from the observed radial-velocity field in the galaxy. Section 4 presents the results of our analysis of the velocity field in the galaxy NGC 628. Section 5 describes the distribution of the SFR in an individual star-forming complex (giant HII region) and the construction of the radial distribution of the SFR in the galactic disk, which we compare to the radial profile of the velocity of gas inflow into the spiral

arm and the positions of resonances in NGC 628. Section 6 presents our discussion and conclusions.

2. CONTRIBUTION OF SPIRAL-DENSITY-WAVE PERTURBATIONS TO THE RADIAL-VELOCITY FIELD

The radial-velocity field of the gas in galactic disks exhibits systematic effects that consist of deviations from purely circular motion, and which coincide with the observable spiral pattern of the galaxy [2]. These deviations could be due to the effect of the spiral-density wave on the purely circular rotation of the gas in the disk [3]. The perturbed velocities due to the spiral wave depend on the amplitude of the wave, the position of the corotation and Lindblad resonances, and the mass distribution in the galaxy (the shape of the rotation curve). The same parameters affect the radial behavior of the velocity of gas inflow into the spiral arm, and thereby probably also the radial profile of the SFR in the disk. Consider the spiral-density wave's contribution to the observed radial velocity $V_r^{obs}(R, \theta)$, where R is the galactocentric distance and θ is the polar angle, measured from the major axis of the galaxy. The spiral coordinates (η, ξ), where η and ξ are directed across and along the spiral, respectively, are related to the polar coordinates (R, θ) as:

$$\eta = m\theta + mh \cot \mu \ln \left(\frac{R}{R_0} \right), \qquad (1)$$

$$\xi = mh\theta \cot \mu - \ln \left(\frac{R}{R_0} \right),$$

where $h = +1$ and $h = -1$ for an S- and Z-spiral, respectively, μ is the pitch angle, and m is the number of arms. The components (u_η, u_ξ) of the velocity perturbation produced by the spiral-density wave in the plane of the disk can, to the first approximation, be written

$$u_\eta = A\nu \cos \eta, \qquad (2)$$

$$u_\xi = A\frac{\kappa}{2\Omega} \sin \eta,$$

where A is a scale factor and Ω is the angular rotational velocity of the matter in the disk, which is a function of the galactocentric distance R. The epicyclic frequency κ is related to the angular rotational velocity as

$$\kappa^2 = (2\Omega)^2 \left(1 + \frac{R}{2\Omega} \frac{d\Omega}{dR} \right).$$

The rotational frequency ν in (2) can be written in terms of the rigid-rotation velocity of the spiral pattern Ω_p as:

$$\nu = \frac{m(\Omega_p - \Omega)}{\kappa}.$$

The radial and tangential components of the velocity of the spiral perturbations in polar coordinates $(\delta V_R, \delta V_\theta)$ depend on the pitch angle μ:

$$\delta V_R = u_\eta \cos \mu - u_\xi \sin \mu, \qquad (3)$$

$$\delta V_\theta = h (u_\eta \sin \mu - u_\xi \cos \mu).$$

The contribution to the observed radial velocity produced by the radial and tangential components of the velocity of the spiral perturbations (i.e., the line-of-sight projection of the noncircular motions due to the spiral perturbations) is equal to:

$$V_{sp} = (\delta V_R \sin \theta + \delta V_\theta \cos \theta) \sin i, \qquad (4)$$

where i is the inclination of the plane of the galaxy to the plane of the sky.

The observed radial velocity at a given point of the disk can be comprised of the systematic velocity of the bulk motion of the galaxy V_{sys}, the line-of-sight projection of the rotational velocity of the gas in the disk $V_\theta \cos \theta \sin i$, the line-of-sight projection of the radially symmetrical velocity of gas in the disk $V_R \sin \theta \sin i$, and the velocity of noncircular motions due to spiral perturbations:

$$V_r^{obs}(R, \theta) = V_{sys} + V_\theta(R) \cos \theta \sin i \qquad (5)$$
$$+ V_R(R) \sin \theta \sin i + V_{sp}.$$

We now designate in (2) that part of the spiral phase that is constant at a given galactocentric distance R as: $\theta_{sp} = mh \cot \mu \ln \left(\frac{R}{R_0} \right)$, then substitute (1)–(3) into (4) to obtain

$$\frac{V_{sp}}{\sin i} = A\nu \cos(m\theta + \theta_{sp}) \cos \mu \sin \theta \qquad (6)$$

$$- A\frac{\kappa}{2\Omega} \sin(m\theta + \theta_{sp}) \sin \mu \sin \theta$$

$$+ hA\nu \cos(m\theta + \theta_{sp}) \sin \mu \cos \theta$$

$$+ hA\frac{\kappa}{2\Omega} \sin(m\theta + \theta_{sp}) \cos \mu \cos \theta.$$

Rearranging the terms in (6), we obtain

$$\frac{V_{sp}}{\sin i} = A\nu \cos(m\theta + \theta_{sp})(\cos \mu \sin \theta \qquad (7)$$

$$+ h \sin \mu \cos \theta) - A\frac{\kappa}{2\Omega} \sin(m\theta + \theta_{sp})$$

$$\times (\sin \mu \sin \theta - h \cos \mu \cos \theta).$$

We then use the trigonometric formula

$$\sin(x \pm y) = \sin x \cos y \pm \cos x \sin y, \qquad (8)$$

to rewrite (7) in the form

$$\frac{V_{sp}}{\sin i} = A\nu \cos(m\theta + \theta_{sp}) \sin(\theta + h\mu) \qquad (9)$$

$$+ A\frac{\kappa}{2\Omega} \sin(m\theta + \theta_{sp}) \cos(\theta - h\mu).$$

Using the trigonometric formula

$$\sin x \cos y = \frac{1}{2}\left[\sin(x-y) + \sin(x+y)\right], \quad (10)$$

we rewrite (9) in the form

$$\frac{V_{sp}}{\sin i} = -A\frac{\nu}{2}\sin[(m-1)\theta + (\theta_{sp} - h\mu)] \quad (11)$$

$$+ A\frac{\kappa}{4\Omega}\sin[(m-1)\theta + (\theta_{sp} + h\mu)]$$

$$+ A\frac{\nu}{2}\sin[(m+1)\theta + (\theta_{sp} + h\mu)]$$

$$+ A\frac{\kappa}{4\Omega}\sin[(m+1)\theta + (\theta_{sp} - h\mu)].$$

Using (8) to rewrite (11) yields

$$\frac{V_{sp}}{\sin i} = -A\frac{\nu}{2}\{\sin[(m-1)\theta]\cos(\theta_{sp} - h\mu) \quad (12)$$

$$+ \cos[(m-1)\theta]\sin(\theta_{sp} - h\mu)$$

$$+ A\frac{\kappa}{4\Omega}\{\sin[(m-1)\theta]\cos(\theta_{sp} + h\mu)$$

$$+ \cos[(m-1)\theta]\sin(\theta_{sp} + h\mu)$$

$$+ A\frac{\nu}{2}\{\sin[(m+1)\theta]\cos(\theta_{sp} + h\mu)$$

$$+ \cos[(m+1)\theta]\sin(\theta_{sp} + h\mu)$$

$$+ A\frac{\kappa}{4\Omega}\{\sin[(m+1)\theta]\cos(\theta_{sp} - h\mu)$$

$$+ \cos[(m+1)\theta]\sin(\theta_{sp} - h\mu)\}.$$

We now group the sine and cosine terms of identical quantities containing θ to rewrite (12) in the form

$$\frac{V_{sp}}{\sin i} = A(\frac{\kappa}{4\Omega} - \frac{\nu}{2})\cos(\theta_{sp} - h\mu) \quad (13)$$

$$\times \cos(\theta_{sp} + h\mu)\sin[(m-1)\theta]$$

$$+ A(\frac{\kappa}{4\Omega} - \frac{\nu}{2})\sin(\theta_{sp} - h\mu)$$

$$\times \sin(\theta_{sp} + h\mu)\cos[(m-1)\theta]$$

$$+ A(\frac{\kappa}{4\Omega} + \frac{\nu}{2})\cos(\theta_{sp} - h\mu)$$

$$\times \cos(\theta_{sp} + h\mu)\sin[(m+1)\theta]$$

$$+ A(\frac{\kappa}{4\Omega} + \frac{\nu}{2})\sin(\theta_{sp} - h\mu)$$

$$\times \sin(\theta_{sp} + h\mu)\cos[(m+1)\theta].$$

The coefficients of the sines and cosines of the polar angles $(m-1)\theta$ and $(m+1)\theta$ determine the contribution of the spiral-density wave to the observed radial velocity. It is obvious from (13) that the second mode of the spiral-density wave $(m = 2)$—a two-armed spiral—contributes to quantities multiplied by the sines and cosines of the polar angles θ and 3θ; i.e., to the first and third Fourier harmonics of the azimuthal distribution of the radial velocities at galactocentric distance R. The first mode of

the spiral wave $(m = 1)$—a one-armed asymmetric structure—contributes to the zeroth and second Fourier harmonics of the azimuthal distribution of the radial velocities. Determining the parameters of the density wave from the observed radial-velocity field in the galactic disk thus reduces to a Fourier analysis of the azimuthal radial-velocity distribution at various galactocentric distances.

In [4–6], we carried out a Fourier analysis of the azimuthal radial-velocity distribution in annular zones at various galactocentric distances for the galaxies NGC 3031, NGC 925, NGC 2903, and NGC 6946. Canzian and Allen [7] and Fridman *et al.* [8, 9] used a similar approach to analyze perturbed velocities in NGC 4321, NGC 157, and NGC 3631. The amplitudes of the various derived Fourier harmonics can be used to estimate the parameters of the density wave in the galactic disk.

3. ALLOWING FOR NONCIRCULAR MOTIONS IN THE GALACTIC DISK

In [5], we approximated the observed radial velocity $V_r^{obs}(R, \theta)$ by the two-dimensional function of the polar coordinates (R, θ)

$$V_r^{obs}(R, \theta) = \sin i \quad (14)$$

$$\times \sum_{n=0}^{3}[a_n(R)\cos(n\theta) + b_n(R)\sin(n\theta)].$$

An explanation of the physical meaning of the coefficients $a_n(R)$ and $b_n(R)$ can be found in Table 1 in [5] and in formula (13). Different modes of the spiral wave $(m = 1, 2, 3 \dots)$ should contribute to the coefficients of different Fourier harmonics $(n = 0, 1, 2, 3, 4 \dots)$.

The coefficient $a_0(R)$ of the zeroth harmonic $(n = 0)$ is comprised of the systematic velocity of the galaxy as a whole, V_{sys}, and a contribution from the first-order mode of the spiral wave:

$$a_0(R) = V_{sys} + A\left(\frac{\kappa}{4\Omega} - \frac{\nu}{2}\right) \quad (15)$$

$$\times \cos(\theta_{sp} - h\mu)\cos(\theta_{sp} + h\mu),$$

where $\theta_{sp} = h\cot\mu\ln\left(\dfrac{R}{R_0}\right)$ is the phase of the one-armed spiral. Therefore, when approximated using (14), the dependence of the systematic velocity on the galactocentric radius R of a given annular zone may appear in the azimuthal distribution of the observed radial velocities in selected zones in the galactic disk. The first-order mode $(m = 1)$ also contributes to the second harmonic $(n = 2)$, as was found earlier for the galaxies NGC 3031 and NGC 2903 [5].

The coefficient $a_1(R)$ of the cosine of the polar angle θ in the first harmonic $(n = 1)$ is comprised of

the circular rotational velocity of the gas in the disk, $V_\theta(R)$, and the tangential component of the contribution of the second-order mode of the spiral wave, δV_θ:

$$a_1(R) = V_\theta(R) + A\left(\frac{\kappa}{4\Omega} - \frac{\nu}{2}\right) \qquad (16)$$
$$\times \sin(\theta_{sp} - h\mu)\sin(\theta_{sp} + h\mu).$$

Here, in (16), and in (17) and (18) below, the phase of the two-armed spiral is $\theta_{sp} = 2h\cot\mu\ln\left(\frac{R}{R_0}\right)$.

The coefficient $b_1(R)$ of the sine of the polar angle θ of the first harmonic ($n = 1$) is comprised of the velocity of the radially symmetrical motion of the gas in the disk, $V_R(R)$, and the radial component of the contribution of the second-order mode of the spiral wave, δV_R:

$$b_1(R) = V_R(R) + A\left(\frac{\kappa}{4\Omega} - \frac{\nu}{2}\right) \qquad (17)$$
$$\times \cos(\theta_{sp} - h\mu)\cos(\theta_{sp} + h\mu).$$

It is obvious from (13) that the second-order mode also shows up in the coefficients $a_3(R)$ and $b_3(R)$ of the third Fourier harmonic:

$$a_3(R) = A\left(\frac{\kappa}{4\Omega} + \frac{\nu}{2}\right)\sin(\theta_{sp} - h\mu)\sin(\theta_{sp} + h\mu),$$
$$(18)$$
$$b_3(R) = A\left(\frac{\kappa}{4\Omega} + \frac{\nu}{2}\right)\cos(\theta_{sp} - h\mu)\cos(\theta_{sp} + h\mu).$$

Neglecting in a first approximation the velocity of the radially symmetrical motion in (17), we can derive from (16)–(18) a formula for the circular rotational velocity of the disk

$$V_\theta(R) = a_1 - b_1\frac{a_3}{b_3}, \qquad (19)$$

which coincides with (27) in [10]. We can also derive from these same equations formulas for the frequency ν and ratio $\frac{\kappa}{2\Omega}$:

$$\nu = \frac{b_3 - b_1}{A\cos(\theta_{sp} - h\mu)\cos(\theta_{sp} + h\mu)}, \qquad (20)$$

$$\frac{\kappa}{4\Omega} = \frac{b_3 + b_1}{A\cos(\theta_{sp} - h\mu)\cos(\theta_{sp} + h\mu)}. \qquad (21)$$

Recalling that $\nu = m(\Omega_p - \Omega)/\kappa$, and multiplying (20) and (21), we obtain

$$\nu = \frac{m(\Omega_p - \Omega)}{\kappa} \qquad (22)$$
$$= \frac{b_3^2 + b_1^2}{A^2\cos^2(\theta_{sp} - h\mu)\cos^2(\theta_{sp} + h\mu)}.$$

Relation (22) implies the condition

$$\Omega_p < \Omega \quad \text{when} \quad b_3^2 < b_1^2, \qquad (23)$$

$$\Omega_p > \Omega \quad \text{when} \quad b_3^2 > b_1^2.$$

The condition (23) agrees with the condition (34) from [8], as well as with the condition for determining the corotation radius R_c introduced by Canzian [10]:

$$\nu < 0 \quad \text{when} \quad R < R_c, \qquad (24)$$
$$\nu > 0 \quad \text{when} \quad R > R_c.$$

Both conditions are fulfilled in [8] and [10] under the assumption that the velocity of radially symmetrical motion is zero: $V_R(R) = 0$.

In addition to the first-order mode ($m = 1$), the second Fourier harmonic may also include a substantial contribution from the third-order mode ($m = 3$), which is manifested most clearly in the outer part of the disk. In their analysis of the central regions of the galaxies NGC 157 and NGC 3631, Fridman *et al.* [8, 9] interpret the radial behavior of the coefficients at the cosine and sine of 2θ as the line-of-sight projections of vertical motions (i.e., motions perpendicular to the plane of the disk) in the spiral wave.

4. RADIAL-VELOCITY FIELD OF THE GAS IN NGC 628 AND THE PARAMETERS OF THE SPIRAL-DENSITY WAVE

The ScI spiral galaxy NGC 628 is one of only a few galaxies whose kinematics have been studied in detail. Shostak and van der Kruit [11] constructed the two-dimensional field of the HI radial velocities for the inner, optically visible, part of the galaxy using the aperture-synthesis method, and Kamphuis and Briggs [12] extended this field to the outer part of the galaxy that is detectable in the radio. These observations showed that the kinematics of the gas in the main, optical part of the galaxy correspond to a flat, differentially rotating disk. The velocity field in the outer, optically dark parts of the disk deviates from the behavior for a flat, differentially rotating disk and exhibits a complex, irregular structure. A discussion of possible origins of the peculiar motions in the outer parts of the galaxy is given by Kamphuis and Briggs [12]. To identify noncircular motions associated with the spiral pattern in the inner, optical part of the disk, we performed a Fourier analysis of the two-dimensional HI-velocity field presented in [11], which has spatial and velocity resolutions of $13.8'' \times 48.5''$ ($\alpha \times \delta$) and 5 km/s, respectively. A detailed discussion of the corresponding Westerbork Synthesis Radio Telescope (WSRT) observations can be found in [11]. Table 1 lists the main optical parameters of NGC 628.

We obtained a least-squares fit of the two-dimensional radial-velocity field using (14) for annular zones with width $\Delta R = 1$ kpc in steps of 1 kpc for galactocentric distances from 2 to 10 kpc. We

Table 1. Optical parameters of NGC 628

Type	SAS5	de Vaucoulers *et al.* (1976) [13]
	Sc(s)I	Sandage and Tammann (1974) [14]
α (1950)	$1^h34^m00.5^s$	Gallouet and Heidmann (1971) [15]
δ (1950)	$15°31'38''$	
	$1^h34^m00.7^s$	Dressel and Condon (1976) [16]
	$15°31'55''$	
	$1^h34^m01^s$	de Vaucouleurs *et al.* (1976) [13]
	$15°31'36''$	
Distance	19.6 Mpc	Sandage and Tammann (1974) [14]
	10.4 Mpc	$H = 75 \ \mathrm{km \ s^{-1} \ Mpc^{-1}}$
	7.2 Mpc	McCall (1982) [18]
	7.2 Mpc	Adopted in this paper
D_{25}	$10.4'$	Vaucoulers *et al.* (1976) [13]
	(21.84 kpc)	
Holmberg radius	$6'$	Holmberg (1958) [19]

determined the geometrical parameters (the center of rotation (x_c, y_c) and position angle of the line of nodes PA) by minimizing the dispersions of the desired Fourier coefficients $a_n(R), b_n(R)$ in (14) by varying (x_c, y_c) and PA. The dispersions of the desired coefficients in (14) increase as (x_c, y_c) and PA move away from the adopted values. The center of rotation derived in this way deviates by $-3.1''$ in declination and $-2.5''$ in right ascension from the optical center reported by de Vaucouleurs [13], which, in turn, is shifted by $-19''$ in δ and $+4.5''$ in α relative to the optical center reported by Dressel and Condon [16]. The distance between our optical center and that of de Vaucouleurs [13] is $3.92''$, which corresponds to a linear distance of about 140 pc. Table 1 shows that the center coordinates derived by Gallouet and Heidmann [15] are closer to those of de Vaucouleurs [13], with a shift of about $7.5''$, which corresponds to a linear distance of 260 pc. The offset between the center positions of de Vaucouleurs *et al.* [13] and Dressel and Condon [16] does not exceed 600 pc. Forcing the dynamical center to coincide with the center coordinates of Dressel and Condon [16] results in a nonsystematic pattern for the noncircular velocity field that has no relation to the spiral pattern, as was found by Shostak and van der Kruit [11].

Since the inner disk in NGC 628 has a very small inclination to the plane of the sky, the procedure we have used here is not very sensitive to this inclination, i. We chose the value $i \approx 6°$ based on the fact that the rotation curve flattens into a plateau with a velocity of about 200 km/s for this inclination, which corresponds to the observed luminosity of $M_B = -20.23^m$ [20] for the galaxy. Higher inclinations imply unrealistically low rotational velocities, with the rotation-curve plateau having the velocity 70−90 km/s. The adopted inclination and position angle of the major axis are listed in Table 2.

NGC 628 is a bright Sc spiral. In his classic atlas, Danver [21] points out two arms with a mean pitch angle of $\mu = 17° \pm 2°$. In their analysis of computer-enhanced images of galaxies, Elmegreen *et al.* [22] showed that NGC 628 contains two main symmetrical arms extending to a distance of $0.9R_{25}$ (10 kpc) from the galactic center. We showed above that a two-armed spiral-density wave contributes to the first and third Fourier harmonics. The first-order mode contributes to the zeroth and second Fourier harmonics while the third-order mode contributes to the second and fourth harmonics. The second-order mode contributes to the first and third harmonics, which are independent of the zeroth and second harmonics in Fourier space, so that the first- and third-order modes should not distort the coefficients of the first and third harmonics in the Fourier expansion. We therefore restricted our analysis of the azimuthal distribution of the velocities in annular zones to the first three Fourier harmonics ($n = 1, 2, 3$).

Figure 1c shows the radial behavior of the coefficient $a_1(R)$ of the first Fourier harmonic (squares) in (14), which consists of the circular rotational velocity
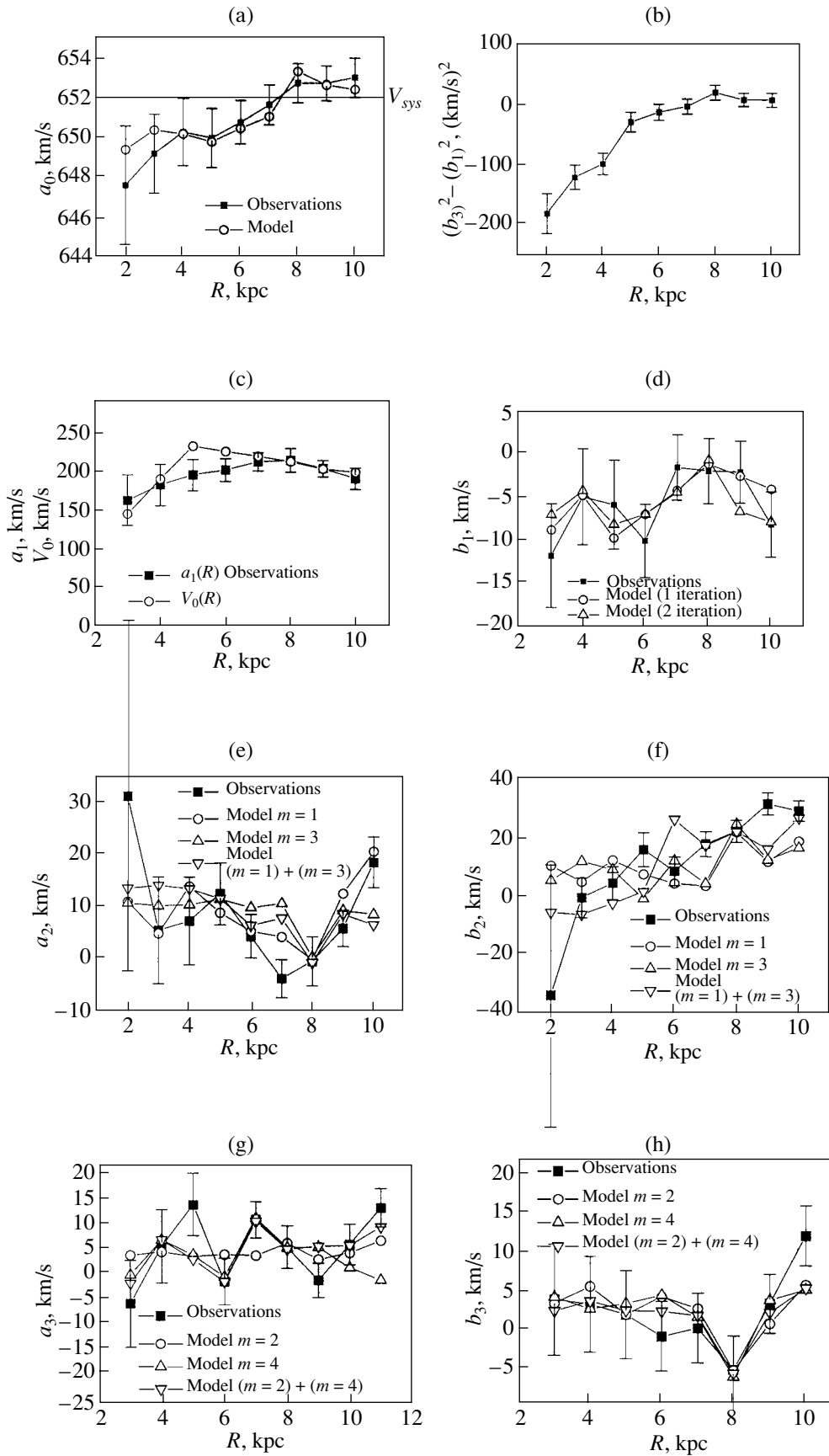
Fig. 1. Fourier spectrum of the velocity field of NGC 628 ($n = 0, 1, 2, 3$; filled squares). See text for details.
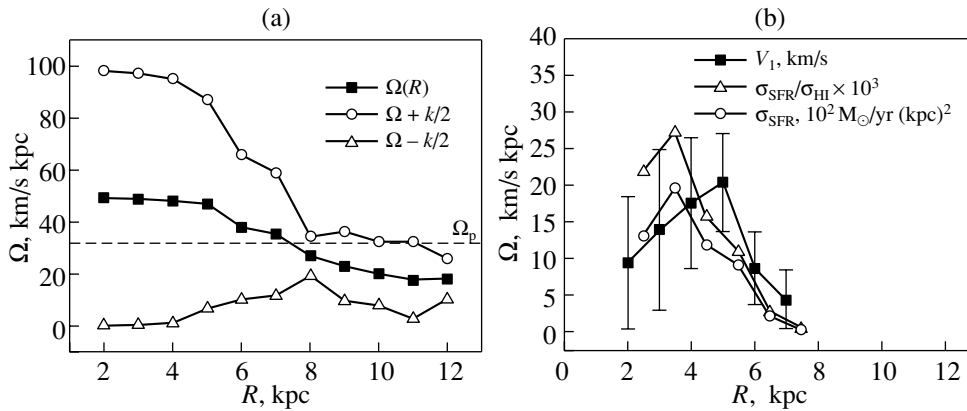
Fig. 2. (a) Corotation resonance ($\Omega_p = \Omega(R)$) in NGC 628, located at about $R = 7$ kpc, and the outer Lindblad resonance ($\Omega_p = \Omega(R) + \frac{\kappa}{2}$), located at $R \approx 10-11$ kpc, near $R_{25} = 11$ kpc. (b) Velocity of gas inflow into the spiral arm, $V_\perp(R)$, as a function of galactocentric distance in NGC 628 (filled squares) and the radial distribution of the surface density of the SFR, $\sigma_{SFR}(R)$ (circles).

and $b_3(R)$ are best described by a superposition of the second- and fourth-order modes of the density wave (the $(m = 2) + (m = 4)$ model is shown by the inverted triangles).

Figure 2a elucidates the position of the corotation resonance ($\Omega_p = \Omega(R)$) in NGC 628. The outer Lindblad resonance ($\Omega_p = \Omega(R) + \frac{\kappa}{2}$) is located at a distance of $R \approx 10-11$ kpc, near $R_{25} = 11$ kpc. Whether the galaxy has an inner Lindblad resonance ($\Omega_p = \Omega(R) - \frac{\kappa}{2}$) depends on the form of $\Omega(R)$ near the center of the galaxy. Rigid-rotation models with a low mass concentration toward the center possess no inner Linblad resonance, since $\Omega_p = \Omega(R) - \frac{\kappa}{2} \equiv 0$. NGC 628 appears to have a low mass concentration toward the center.

Having cleaned the galactic rotation curve of perturbations due to the spiral-density wave and determined the pattern speed, $\Omega_p = 32$ km s^{-1} kpc^{-1}, we can determine the velocity of gas inflow into the spiral wave, $V_\perp(R)$ (Fig. 2b, filled squares):

$$V_\perp = R[\Omega(R) - \Omega_p] \sin \mu. \qquad (25)$$

Figure 2b shows that $V_\perp(R)$ first increases with galactocentric distance, reaches a maximum, and then monotonically decreases to zero near the corotation radius. The velocity of gas inflow into the arm determines the degree of compression of gas and the formation of shock fronts in the arm, which, in turn, affects star formation in the arms. We will analyze the relationship between the velocity of gas inflow into the arm and the position of the corotation and Lindblad resonances, on the one hand, and star formation in the disk, on the other hand, in Section 5 below.

5. STAR-FORMATION RATE IN THE DISK OF NGC 628

The radial distribution of the surface density of the star-formation rate in the disk is indirectly characterized by the distribution of the surface number density of HII regions, and can be calculated from the total Hα flux from HII regions. It is important to account for losses due to extinction and the fraction of Lyman-continuum photons that are absorbed by interstellar dust and so do not participate in ionization processes. Descriptions of the method used to estimate the total SFR and its average surface density from Hα emission-line flux measurements in galactic disks are given in [26, 27] and references therein.

In [28] we obtained a dependence (with a correlation coefficient of $r = 0.8$) between the SFR and the linear size of star-forming complexes (giant HII regions) in spiral and irregular galaxies:

$$\log(\text{SFR}[M_\odot/\text{yr}]) \qquad (26)$$
$$= -(10.15 \pm 0.80) + (3.82 \pm 0.44) \log(S\,[\text{pc}]).$$

Figure 3a compares the calibration of the SFR based on the SFR–size dependence (26) with the calibration of Kennicutt *et al.* [26], based on Hα fluxes. Figure 2b also shows the radial distribution of the surface density of the SFR, $\sigma_{SFR}(M_\odot/\text{yr kpc}^2)$ and the quantity σ_{SFR} normalized to the mass of gas in NGC 628 (circles and triangles, respectively). The surface density of the SFR was calculated by subdividing the disk of the galaxy into annular zones with width $\Delta R = 1$ kpc in radial steps of 1 kpc. We calculated the surface density of the SFR in each annulus by dividing the sum of the SFRs for all star-forming complexes located within an annulus by the area of the annulus. We used (26) to compute the
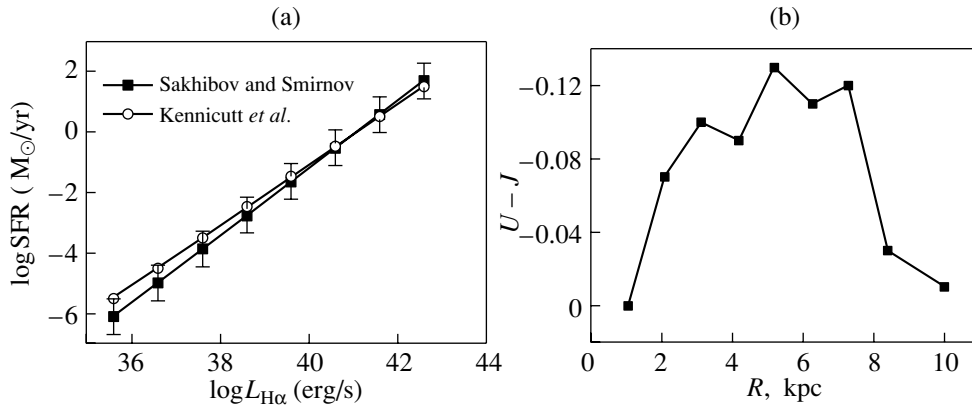
Fig. 3. (a) Comparison of the calibration of the SFR based on the SFR−size S [pc] dependence with the calibration of Kennicutt *et al.* [26], based on Hα flux measurements. (b) Radial distribution of the $U - J$ color index (according to [11]), which characterizes the ratio of relatively young stars to older-generation stars.

SFR of each individual star-forming complex. The sizes and coordinates of a complete sample of star-forming complexes (giant HII regions) in NGC 628 have been measured by Belley and Roy [29]. We adopted the radial distribution of neutral hydrogen, which we used to normalize the SFR to the total gas mass, from Shostak and van der Kruit [11].

The annular shape of the radial distribution of the surface density of the SFR shown in Fig. 2b is typical of the pattern seen in the case of ongoing star formation in other galaxies, including the Milky Way. Starting from a distance of $R = 1$ kpc, σ_{SFR} increases, reaching its maximum at $R_m = 3-4$ kpc, and then decreases until it becomes zero near the corotation resonance at $7-8$ kpc. Star formation in NGC 628 is unimportant beyond the corotation radius.

The fact that the radial dependence of the SFR and this dependence normalized by the gas mass (circles and triangles, respectively, in Fig. 2b) match the velocity of gas inflow into the arms (squares in Fig. 2b) shows that the late Sc galaxy NGC 628 contains large quantities of gas that have not been depleted by star formation, and that the radial distribution of the gas still matches that of the SFR. In early-type (Sa-S0) galaxies, which have already exhausted their gas, the radial distribution of the velocity of gas inflow into the arms can be expected not to match that of the SFR in star-forming complexes.

6. DISCUSSION

The relationship between the SFR and the spiral-density wave in the disk is illustrated by the curve representing the velocity of gas inflow into the arms (Fig. 2b, squares), whose form is similar to that of the radial distribution of σ_{SFR} (Fig. 2b, circles). It follows that the higher the velocity $V_\perp(R)$ of gas inflow into the spiral arm, the higher the intensity of star formation at a given galactocentric radius in the galaxy. Of course, the radial distribution of the gas in the disk also plays some role. The velocity component $V_\perp(R)$ undergoes a jump when it crosses the boundary of the spiral arm, so that the gas is decelerated and compressed, making a transition from an intercloud to a cloud phase [30]. If the gas contains clouds in a state close to gravitational instability, abrupt compression may trigger the gravitational condensation of clouds, resulting in the formation of stars, HII regions, and star-forming complexes.

Near the corotation resonance ($7-7.5$ kpc), where the velocity of gas inflow is $V_\perp(R_c) = 0$, the gas is not compressed when it crosses the arm, so this crossing should not result in the condensation of clouds or trigger star formation. This is illustrated by the radial dependence of the surface density of the SFR $\sigma_{SFR}(R)$ in Fig. 2b (circles).

The radial distribution of the $U - J$ color index [11], which characterizes the ratio of young stars to older-generation stars, is similar to the radial dependence of the velocity of gas inflow into the spiral arm (Fig. 3b). The radial $UBVRI$ photometric profiles also extend not far beyond the corotation resonance, out to the vicinity of the outer Lindblad resonance, $R = 10-11$ kpc [31].

The velocity field beyond the outer Lindblad resonance is not consistent with a flat, differentially rotating disk. A warped-disk model is likewise unable to fully explain the structure of the velocity field in the outer, optically dark parts of NGC 628 [12].

Above, we obtained a qualitative description of the relationship between the kinematics of the gas and star formation in the disk of NGC 628. The parameters of the spiral-density wave that we inferred by

analyzing the observed radial-velocity field for neutral hydrogen can be used to compute the shock wave in a model of the spiral front propagating through a multiphase gaseous medium, and to develop a model for cloud formation, and ultimately for star formation. However, this lies beyond the scope of this paper.

7. CONCLUSIONS

In conclusion, we list the results we have obtained in this paper.

Fourier analysis of the observed polar-angle distribution for the projections of radial velocities in the plane of NGC 628 reveal the coexistence of several modes of a spiral-density wave that rotate at the same angular velocity. The radial behavior of the velocity of gas inflow into the spiral arm is similar to that of the surface density of the SFR in the galactic disk.

The region of star formation in the disk has the form of an annulus located at galactocentric distances from 2 to 7.5 kpc, with a maximum at 3.5−4 kpc.

The absence of an inner Lindblad resonance is indicative of a low concentration of mass toward the center of the galaxy, and of the absence of a bulge.

REFERENCES

1. W. W. Roberts, M. S. Roberts, and F. H. Shu, Astrophys. J. **196**, 381 (1975).
2. H. Visser, Astron. Astrophys. **88**, 149 (1980).
3. C. C. Lin, C. Yuan, F. H. Shu, and H. Frank, Astrophys. J. **155**, 721 (1969).
4. F. Kh. Sakhibov and M. A. Smirnov, Astron. Zh. **64**, 255 (1987) [Sov. Astron. **31**, 132 (1987)].
5. F. Kh. Sakhibov and M. A. Smirnov, Astron. Zh. **66**, 921 (1989) [Sov. Astron. **33**, 476 (1989)].
6. F. Kh. Sakhibov and M. A. Smirnov, Astron. Zh. **67**, 690 (1990) [Sov. Astron. **34**, 236 (1990)].
7. B. Canzian and R. Allen, Astrophys. J. **479**, 723 (1997).
8. A. M. Fridman, O. V. Khoruzhii, V. V. Lyakhovich, *et al.*, Astron. Astrophys. **371**, 538 (2001).
9. A. M. Fridman, O. V. Khoruzhii, E. V. Polyachenko, *et al.*, Mon. Not. R. Astron. Soc. **323**, 651 (2001).
10. B. Canzian, Astrophys. J. **414**, 487 (1993).
11. G. S. Shostak and P. C. van der Kruit, Astron. Astrophys. **132**, 20 (1984).
12. J. Kamphuis and F. Briggs, Astron. Astrophys. **253**, 335 (1992).
13. G. Vaucoulers, A. de Vaucouleurs, and H. G. Corwin, *Second Reference Catalog of Bright Galaxies* (Univ. of Texas, Austin, 1976).
14. A. Sandage and G. A. Tammann, Astrophys. J. **190**, 525 (1974).
15. L. Gallouet and N. Heidmann, Astron. Astrophys., Suppl. Ser. **3**, 325 (1971).
16. L. L. Dressel and J. J. Condon, Astrophys. J., Suppl. Ser. **31**, 187 (1976).
17. A. Sandage and G. A. Tammann, Astrophys. J. **194**, 559 (1974).
18. M. L. McCall, Ph. D. Thesis (Univ. of Texas, Austin, 1982).
19. E. Holmberg, Medd. Lund Astron. Obs., Ser. II, No. 136 (1958).
20. G. S. Shostak, Astron. Astrophys. **68**, 321 (1978).
21. G. G. Danver, Ann. Observ. Lund, No. 10 (1942).
22. B. Elmegreen, D. Elmegreen, and L. Montenegro, Astrophys. J., Suppl. Ser. **79**, 37 (1992).
23. T. Ohnishi, Astrophys. Space Sci. **25**, 217 (1973).
24. S. H. Lubow, S. A. Balbus, and L. L. Cowie, Astrophys. J. **309**, 496 (1986).
25. D. Moss, A. Shukurov, and D. Sokoloff, Astron. Astrophys. **358**, 1142 (2000).
26. R. C. Kennicutt, P. Tamblyn, and C. W. Congdon, Astrophys. J. **435**, 22 (1994).
27. R. Kennicutt, Astrophys. J. **498**, 541 (1998).
28. F. Kh. Sakhibov and M. A. Smirnov, Astron. Zh. **81** (2004, in press).
29. J. Belley and J.-R. Roy, Astrophys. J., Suppl. Ser. **78**, 61 (1992).
30. F. H. Shu, V. Milione, W. Gebel, *et al.*, Astrophys. J. **173**, 557 (1972).
31. G. Natali, F. Pedichini, and M. Righini, Astron. Astrophys. **256**, 79 (1992).
32. C. Carignan, P. Charbonneau, F. Boulanger, and F. Viallefond, Astron. Astrophys. **234**, 43 (1990).

Translated by A. Dambis